

Time-of-flight spectrometry of the
spontaneous fission neutron
emission from ^{244}Cm and ^{252}Cf using
EJ-309 liquid scintillators

Submitted in accordance with the requirements of Lancaster University
for the degree of Doctor of Philosophy

Alexander James Grievson

January 2020

ACKNOWLEDGEMENTS:

No thesis is a solo effort, and this one is certainly no exception, there are many people that I need to thank, not only for direct contributions made to the thesis itself, but also those who have accompanied me on the journey, and this has certainly been a long and varied one

To the many friends I have made along the way also on the PhD journey, Chris Tighe, Dom Lavantine, Liz Howett, Craig Smith, Helen O'Donnell, Ashley Jones, Jonny Beaumont, Vyas, both the laonnises and many more, sharing the road with you all was a privilege and a joy.

Joe Fennell, who's distractions and adventures have made Lancaster home as well as a place of study.

The many people who have provided invaluable help with the experimental work, and also with developing me as a PhD student, Lee Packer, Neil Roberts, Mike Bunce, Stephanie McElhaney, Michael Aspinall, your efforts are truly appreciated. I wish also to thank AWE plc for their financial support for this research.

To Malcolm Joyce, your supervision, insight and knowledge has been truly and deeply appreciated. Few PhD students have ran as far away from a thesis as I have, and special thanks must go to you for keeping me going. It has been a privilege to be your student.

Finally and by no means least I wish to thank my family. I am very blessed in life to have so many loved ones, but without the support and distraction of my Brother, Cousins, Aunties Uncles and Grandparents I would not be who I am today or have achieved what I have, but most of all I must thank my Parents, Brian and Catharine Grievson to whom I wish to dedicate this thesis in thanks for their support, encouragement and love.

Ministry of Defence ©British Crown Copyright 2020/AWE

ABSTRACT

The identification and characterisation of nuclear material is important for a number of security, safeguards and verification purposes. Nuclides susceptible to nuclear fission produce a characteristic energy distribution of fission neutrons, known as the Prompt Fission Neutron Spectrum (PFNS). The energy distribution of the PFNS can be indicative of the material under observation; the measurement of the energy spectrum of neutrons however is notoriously difficult, due to the stochastic manner in which they interact with radiation instrumentation. Time of flight (TOF) spectrometry however is one way of deterministically measuring the neutron energy.

This research has used a variety of the associated particle TOF technique, to perform real time TOF spectrometry of fission nuclides with a small-scale portable set up, triggering on the prompt fission gamma emission. In order to conduct this, the low energy threshold of EJ-309 has been determined experimentally via monoenergetic neutron irradiations to be 0.75 MeV, and efficiency curves have been fitted to these data to ensure self-consistency.

The TOF spectrometry system has been developed and used to measure the prompt neutron energy spectrum of ^{252}Cf and ^{244}Cm , the latter of which has never been explored in this way. The Maxwellian fission spectrum has been fitted to the PFNS of ^{244}Cm with a parameter $T= 1.33 \text{ MeV } (\pm 0.7)$ and the Watt spectrum has been fitted with parameters of $a=0.918$ and $b=1.151$. On the basis of these measurements it is thought that this small scale, real time TOF spectrometer is able to discriminate between certain nuclides.

Declaration

I, Alexander Grievson, hereby certify that this thesis and the research described within, is all my own work, unless otherwise indicated and has not been submitted in any previous application for a higher degree.

Date:..... Signature of candidate:.....

I Professor Malcolm John Joyce, hereby certify that the candidate has fulfilled the conditions of the resolution and regulations appropriate for the degree of Doctor of Philosophy at Lancaster University and that the candidate is qualified to submit this thesis in application for that degree.

Date:..... Signature of supervisor:.....

Professor Malcolm John Joyce

CONTENTS

Acknowledgements:.....	1
Abstract	0
List of Abbreviations	5
1 Introduction.....	2
1.1 Research aims.....	4
2 Background	6
2.1 Neutrons and their origins.....	6
2.1.1 Nuclear Fission	7
2.1.2 (α,n) Reactions as a source of neutrons	12
2.2 Interaction of neutrons with matter	13
2.3 Neutron detection and measurement	17
2.3.1 Proton recoil detectors	18
2.3.2 Scintillator response.....	21
2.3.3 Neutron spectroscopy with proton recoil scintillators	28
2.3.4 Nuclear reaction detectors	34
2.3.5 Fast neutron spectroscopy using reaction detectors.....	37
2.3.6 Time-of-flight neutron spectroscopy.....	46
3 Experimental methods and apparatus	53
3.1 Apparatus and experimental techniques	53
3.1.1 The detector.....	54
3.1.2 The mixed field analyser	56
3.1.3 Pulse triggering and digitisation	58
3.1.4 Pulse-shape discrimination	58

3.1.5	Pulse height spectra	60
3.1.6	Coincidence mode	61
3.2	Neutron sources	72
3.2.1	The Lancaster ²⁵² Cf source.....	72
3.2.2	Bare sealed sources	74
3.2.3	The NPL Van de Graaf accelerator.....	75
3.2.4	Scatter cone measurements	78
3.3	Experimental set-ups and procedure.....	81
3.3.1	First round of Lancaster measurements.....	81
3.3.2	Second round of Lancaster measurements	83
3.3.3	Detector efficiency characterisation at low incident neutron energy 84	
3.3.4	Bare fission source measurements.....	94
3.3.5	Study of sensitivity of TOF set-up to variables.....	98
4	Results	101
4.1	Lancaster University ²⁵² Cf time-of-flight measurements	101
4.2	NPL low-energy response measurement	105
4.3	Lancaster measurements: round two	111
4.4	Measurement of ²⁵² Cf and ²⁴⁴ Cm bare fission sources.....	113
4.4.1	NPL ²⁵² Cf measurement.....	113
4.4.2	²⁴⁴ Cm source measurements	117
4.4.3	Comparison of ²⁵² Cf and ²⁴⁴ Cm in a small-scale TOF setup	119
4.5	Parameter study on TOF system.....	124
5	Discussion	127
5.1	Initial findings and verification of the TOF spectrometer	127
5.2	NPL Bare ²⁵² Cf source measurements	129
5.3	Curium measurements	130

5.4	Simultaneous ^{244}Cm and ^{252}Cf measurements	136
5.5	NPL Efficiency measurements.....	137
5.5.1	Absolute system efficiency.....	139
5.6	Parameter study	140
5.6.2	The effect of photomultiplier voltage on efficiency	141
5.6.3	The effect of PSD settings on the measurement.....	141
5.7	Implications for isotopic discrimination in a security context.....	142
6	Conclusions of this research	145
6.1	Future Work.....	146
6.2	Final words.....	147
7	References.....	149
	Appendix A: Gamma interactions in the detector.....	167
	Appendix B: Properties of EJ301 and EJ309.....	169

LIST OF ABBREVIATIONS

ADC	Analogue to digital converter
ANN	Artificial neural network
BNC	Bayonet Neill Concelman
CBRN	Chemical biological radiological nuclear
COM	Centre of mass
FPGA	Field programmable gate array
GUI	Graphical user interface
MCNP	Monte Carlo neutron photon (simulation package)
MFA	Mixed field analyser
NPL	National Physical Laboratory
PE	Polyethylene
PFNS	Prompt fission neutron spectrum
PHD	Pulse height distribution
PHS	Pulse height spectrum
PSC	Parajito Scientific Corporation
PSD	Pulse shape discrimination
SHV	Shielded high voltage
SiPM	Silicon photomultiplier
TIC	Twin (back to back) ionisation chamber
TID	Time interval distribution
TOF	Time of flight
TTL	Transistor-transistor logic

1 INTRODUCTION

The discovery of the neutron in 1932 by James Chadwick [1] precipitated a number of important discoveries in the early 20th century. Not least of these was nuclear fission, some six years later, a discovery which in turn would bring about the beginning of the atomic age. Few people in history have seen their discoveries have as great an impact on humanity as James Chadwick, who within a career saw his observations proving the existence of a hitherto unknown subatomic particle, culminate in the detonation of the first atomic weapon in the New Mexico desert.

Civil and military uses of nuclear science have proliferated around the world, carrying with them the many benefits and risks which have rendered it a controversial technology. The general public is all too aware of the hazards posed by radiation, making the control of radioactive materials a high priority for governments and those they task with protecting the public from the more harmful aspects of human progress.

The end of the Cold War saw the dissolution of the Soviet Union and increased international concern about the security of the sprawling civil and nuclear infrastructure left behind. These worries were further compounded by the 9/11 terrorist attacks in New York which inspired significant worldwide policy implementation on counter terrorism and CBRN security themes. [2]

Other than via energetic reactions induced via particle accelerators, free neutrons are produced by unstable heavy isotopes, either as a product of fission, or via the interaction of alpha particles and low Z materials. [3] Accordingly, the presence of significant quantities of free neutrons can be a strong indicator of the presence of nuclear material. [4] It is this relationship between free neutrons and nuclear material that makes their detection and measurement valuable in the fields of nuclear security, safeguards and nuclear materials verification. Additionally, the shielding requirements of neutrons are very different to those of other penetrating radiations such as x-rays or gamma rays, a fact which can be exploited when it is believed that a hazardous substance may be being hidden deliberately. [5]

Radioactive materials which produce neutrons include those which are capable of decay via spontaneous fission, including ^{252}Cf , ^{240}Pu and ^{244}Cm . Plutonium in particular bears a strong association with fissile materials, whilst curium is indicative of spent nuclear fuel and high-level radioactive waste, A further grouping of materials are those susceptible to induced fission, either via neutron-induced fission or gamma-induced photofission. Isotopes of interest in this regard include ^{235}U and ^{239}Pu , which, being fissile materials can constitute a security and safeguards concern but can be detected via the neutron and gamma rays emitted following interrogative stimulation from an external source.

^{244}Cm is of further interest from a materials identification standpoint as its spontaneous fission rate is higher than that of other materials of interest, for example ^{240}Pu . This can lead to its neutron flux obscuring Pu signatures in spent nuclear fuel, which are used to determine ^{240}Pu levels in such materials. [6] Uncertainties associated with the production cross sections of ^{244}Cm lead to high uncertainties in the amounts in fuel after irradiation and thus can complicate burn up assessment.

In addition to special nuclear materials and those associated with the nuclear fuel cycle, neutron sources are used in universities and research institutes around the world and are also used in a number of industrial applications [7]. Research and industrial neutron sources most commonly consist of (α, n) sources and ^{252}Cf fission sources, and are used in universities and research facilities for the characterisation and development of nuclear instrumentation. Industrial uses of neutrons include oil well logging, moisture gauging, industrial tomography, and especially recently, the detection of explosive materials. From a security standpoint, the ability to differentiate between neutron sources and identify their origins is of great value.

1.1 RESEARCH AIMS

The advent of digital electronics has revolutionised many areas of radiation measurement and instrumentation. This research will investigate the potential to further harness these advances in the area of fast neutron detection, with a particular focus on source characterisation and spectrum measurement. The research group at Lancaster has considerable experience in the use of liquid organic scintillators for mixed gamma- neutron detection, work which has been commercially developed by the spin off company, Hybrid Instruments. [8] [9] [10] This research is carried out using a specially modified mixed field analyser, capable of performing coincidence analysis between separate EJ309 liquid scintillator detectors and processing this data to perform time of flight (TOF) spectroscopy.

Neutron TOF spectroscopy has been used in a number of applications previously, most notably for the production of nuclear reference data and the response characterisation of neutron detectors. [11] [12] [13] Interest around the technique is primarily due to it being the only way of deterministically measuring the energy of neutrons. TOF spectroscopy has traditionally required substantial and/ or specialised laboratory infrastructure, a fact which has until recently restricted its use in a more general sense. The ability to store and post-process data provided by digital systems has led to recent developments in associated particle TOF methods, where coincidences between particle detections are used to infer the time of flight of neutrons. This research advances this approach, using correlated gamma – neutron detections to measure the fast neutron energy spectrum.

Obtaining access to ^{239}Pu and ^{235}U for the purposes of simulated fission research measurements comes with difficulty due to the safeguards constraints of these materials. In any case, they are both already well studied and characterised. [14] The spontaneous fission rate of ^{240}Pu is low compared to those of ^{244}Cm and ^{252}Cf , meaning even if it were readily available, acquiring TOF spectra would still be relatively difficult.

Therefore, in this research, ^{252}Cf and ^{244}Cm were selected as isotopes that could be used to assess the ability of the TOF system to discriminate

between nuclides via the measurement of their fast neutron spectra. Each of these isotopes has a reasonably high rate of spontaneous fission and they are far more accessible for research purposes than ^{235}U or ^{239}Pu samples, which would also require stimulation to induce fission. Furthermore, measuring these two isotopes would provide an interesting complementarity in that the spectrum of ^{252}Cf has been studied extensively by virtue of its use as a reference spectrum, [15] [16] whereas the fast neutron spectrum of ^{244}Cm is less well understood, and has not been examined in any detail for quite some time. The prompt fission spectrum of both nuclides is believed to be very similar, and so performing these measurements will give a challenging basis on which to test the TOF approach to nuclide identification, and provide insight into the extrapolation of these findings to the ability to identify other nuclides, such as ^{235}U and ^{239}Pu .

This work undertakes to:

- Miniaturise the hardware associated with performing associated particle TOF spectroscopy and enable the conduction of TOF measurements using a single, FPGA-based data processing unit.
- Perform TOF spectroscopy in real time, i.e. discriminate relevant events and provide the timing information to the user in real time, without the requirement for the storage and postprocessing of superfluous pulse and timing data.
- Use the developed instrument to measure prompt fission neutron energy spectra, particularly those of ^{252}Cf and ^{244}Cm .
- Evaluate the ability of the system to discriminate or identify the nuclide under observation from its fast neutron energy spectrum.

2 BACKGROUND

The work of characterising radiation sources, probing the structure and mechanics of the atomic nucleus, and monitoring and controlling nuclear reactions, has long required a means of observing the behaviour of the neutron. From a block of paraffin wax in front of a Geiger counter, to modern ultra-high-speed electronics and data processing techniques, neutron detection and measurement have developed alongside the fields of nuclear physics and engineering, and indeed have been an essential tool to these ends.

It is an unfortunate fact that, alongside the great potential benefits and uses of the nuclear discoveries of the 20th century, arose the need to prevent their abuse. Treaties intended to reduce the potential for mistakes of eschatological proportions are only as effective as the willingness of state actors to abide by them and, accordingly, new fields of safeguards and materials verification developed to ensure compliance and to foster trust. The potential for the abuse of nuclear materials has necessitated the deployment of technologies to provide nuclear security, and to control the movement and availability of potentially hazardous substances.

It is against this background of security and safeguards that this research is primarily motivated, although the physics and techniques are largely shared across various applications of neutron metrology. The following sections will briefly explore the physics and detection equipment which provide the background for this research.

2.1 NEUTRONS AND THEIR ORIGINS

Although stable whilst bound within the nucleus, free neutrons are unstable, decaying to protons with a half-life of just under 15 minutes (depending on how it is measured [17] [18]). As a result, neutrons exist transiently outside the nucleus and, where they are observed, it is as a product of reactions involving atomic nuclei. The predominant sources of terrestrial neutrons are fission reactions, spallation reactions involving cosmic rays, and interactions

between atomic nuclei and alpha particles (the latter known as (α, n) reactions [19]). Naturally occurring neutron background is primarily made up of neutrons produced by cosmic-ray interactions and is of a low intensity when compared with that of other background radiations. [20] A significant neutron flux is also produced by nuclear fusion, [21] and so neutron measurement is also an important requirement in fusion research.

2.1.1 Nuclear Fission

Nuclear fission was discovered by Meitner, Fritsch and Hahn in 1939 to explain the behaviour of uranium bombarded with neutrons. [22] Soon afterwards, Bohr and Wheeler described the process conceptually in terms of an analogy to surface tension maintaining the shape of a drop of liquid. Opposing forces of the attractive strong nuclear force between all nucleons, and the repulsive coulomb forces produced between protons constantly distort and misshape the nucleus into a dumbbell shape as depicted schematically in Figure 1.

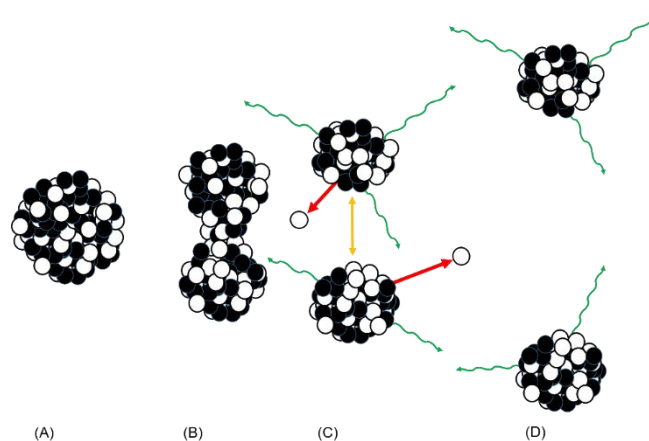


Figure 1: An illustration of the fission process. In (A) the nucleus sits in equilibrium. The interplay of coulomb and strong nuclear forces cause deformation in (B). The nucleus scissions in (C), and emits prompt neutrons after the fragments have fully accelerated. Prompt gamma emission begins alongside neutron emission and lasts slightly longer into (D).

In some cases, the distortion becomes so strong that the attractive force is no longer powerful enough to maintain the single volume, and the nucleus splits, or fissions, into two overly massive and unstable bodies. The two fragments promptly emit neutrons and gamma photons to shed energy

and achieve greater stability. Even after the emission of prompt radiation at the time of fission, fission products are still not stable, and will decay via delayed radiations until they are stable. [23]

Some isotopes with mass numbers greater than 230 can fission spontaneously although this often competes with α -decay. At mass numbers of 230 and just above α -decay dominates, spontaneous fission half-life decreases however with isotopic mass until it begins to approach the rate of α -decay above mass number 252.

The striking of the nucleus by a free neutron can also cause induced fission; the incident nucleus is absorbed, forming an unstable compound nucleus which then fissions in a manner similar to the spontaneous fission described above. Whether a nucleus can be caused to fission via the capture of a neutron depends on the incident neutron energy, and the size and A/Z composition of the nucleus.

The number of neutrons emitted in a particular fission event depends on the size and A/Z composition of the fission fragments. From the point of view of the observer and averaged over many events, they can be assumed to be random, sampled from an approximately Gaussian distribution, with a mean and standard deviation that depends on the parent nuclide. Figure 2 shows the multiplicity distributions for ^{244}Cm and ^{252}Cf . [24]

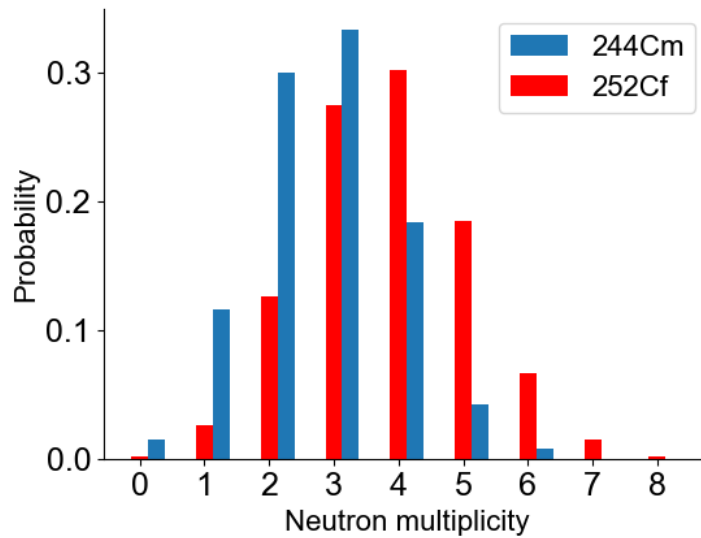


Figure 2: The neutron multiplicity distributions of ^{252}Cf and ^{244}Cm . [24]

The energy spectrum of prompt fission neutrons (the prompt fission neutron spectrum, or PFNS) is related to the energy left with the fission fragments after scission. Early in the study of fission, an analogy to thermodynamic evaporation in liquids has been successful in describing the mechanics behind neutron emission [25]. The fission fragments are left with a certain nuclear temperature, which causes neutrons to “evaporate” off, providing a mechanism for de-excitation (along with prompt gamma emission). The neutrons are evaporated isotropically in the centre of mass frame of the fragment from which they are emitted, with an energy spectrum approximated by a Maxwellian distribution.

This approach describes the energy of the evaporation neutrons in the centre of mass frame with respect to the neutron/ fission fragment system. Perhaps the most frequently used function used to describe the PNFS in the laboratory frame of reference is the Watt spectrum [26]. This treats the neutrons as evaporating off the fission fragments, but transforms to the laboratory frame, reflecting the fact that the majority of neutrons are emitted after the fission fragment is fully accelerated. The Watt spectrum describes

the spectrum using two empirically-derived parameters a and b to describe it. The inclusion of c gives a normalisation parameter. [24]

Equation 1

$$\Phi(E_n) = C e^{-aE_n} \sinh \sqrt{bE_n}$$

The Watt spectrum has been applied to experimental data for a range of nuclides and historically has been the basis for the description and modelling of the PFNS [24]. Both average prompt neutron energy and neutron multiplicity vary with the fission fragment mass and energy, and therefore between different fissioning nuclides. References [27] and [28] give descriptions of comprehensive modelling of the various parameters of fission of different nuclides. Figure 3 shows the Watt spectrum of ^{252}Cf , using parameters of $a=0.84$ and $b=1.03$. The curve is normalised to unity. [24].

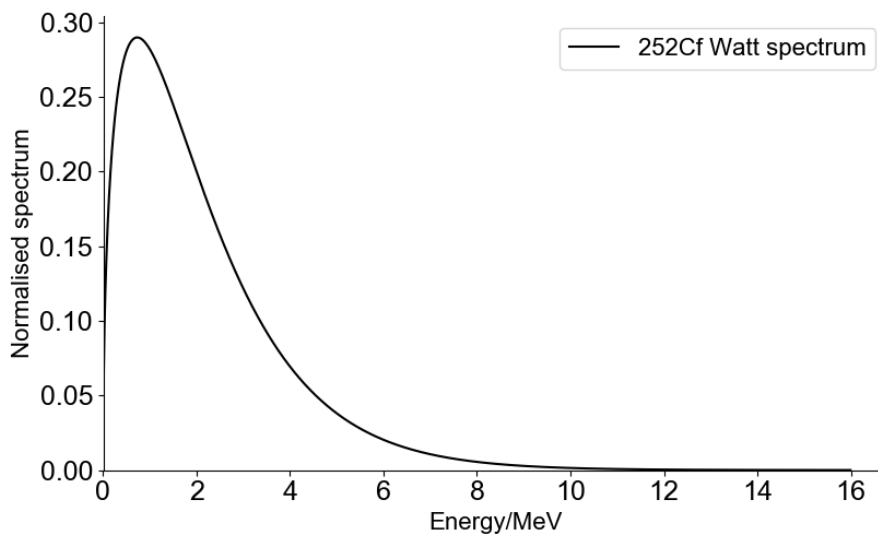


Figure 3: The Watt prompt fission neutron spectrum normalised to unity, shape parameters taken from [24].

The Maxwellian spectrum is also frequently fitted to fission spectra, often with good agreement and uses a single parameter T.

Equation 2

$$\Phi E_n = \frac{2\sqrt{E_n}}{\sqrt{\pi T^3}} \exp\left(-\frac{E_n}{T}\right)$$

The Watt and Maxwellian spectra differ primarily in the low- and high-energy regions, as shown in Figure 4.

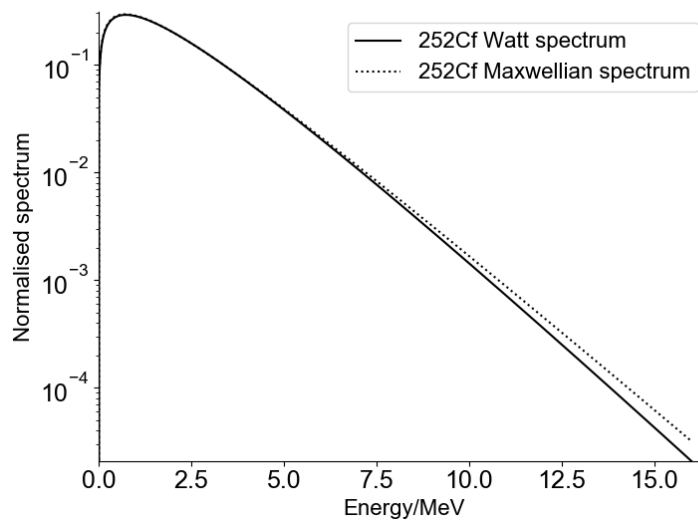


Figure 4: Plot showing the deviation between Watt and Maxwellian spectra of the PFNS of 252Cf.

With regards to the Watt and Maxwellian distributions, it is important to note that, whilst they show good and verified agreement with measured data, they are essentially empirical fits. This means that nuclear data based on Watt or Maxwellian parameters are only as good as the measurements to which they are fitted. There is no predictive ability in the Watt and Maxwellian distributions when it comes to fission spectra that have not been characterised. This can limit the usefulness of the approach, particularly when it comes to modelling induced fission. [29]

There have been efforts to model the PFNS in more detail, particularly with respect to the dependence on fission fragment distributions. The Los Alamos (Madland-Nix) model, for example [30], taking additional aspects of

the fission process into account. These more complex models are usually reserved for modelling use due to their added complexity; where a spectrum is required for comparison with experimental results, either the Watt or Maxwellian spectrum are used in the majority of cases.

2.1.2 (α,n) Reactions as a source of neutrons

The (α,n) reaction was the first type of reaction to be discovered which produced neutrons; this was an important discovery as it was neutrons produced by the bombardment of a beryllium target with alpha particles from a polonium source which led to the discovery of the neutron in 1932 [1]. The (α,n) reaction takes place when an alpha particle is captured by the nucleus of certain low-Z materials, and a neutron is subsequently ejected. [23]

Electrostatic repulsion between the alpha particle and the target nucleus constitutes the coulomb barrier that must be overcome in order for an interaction to occur. As the Z-value of the nucleus increases, the coulomb barrier also increases and so accordingly nuclei above ^{37}Cl are not susceptible to these reactions. The Q-value of the reaction is another important consideration; if the binding energy of the products of the reaction is greater than that of the initial nucleus and alpha particle, then an energy threshold will exist that the alpha particle must overcome in order for the reaction to proceed. The Q-value of a specific $Z(\alpha,n)$ reaction also has implications on the energy spectrum of neutrons produced in this manner.

The (α,n) reaction is a major contributor to the neutron flux produced by spent nuclear fuels due to the abundance of alpha-emitting heavy nuclides alongside oxygen in the form of oxides and other low-Z impurities that build up in the fuel. [23] The (α,n) reaction is also a useful mechanism for the production of neutrons and is utilised in sealed sources which combine a close mixture of an actinide alpha source and a low-Z target material such as beryllium. This constitutes a convenient, passive and portable source of neutrons. [23]

2.2 INTERACTION OF NEUTRONS WITH MATTER

Free neutrons react relatively infrequently with the matter around them. Being uncharged, they do not interact via the Coulomb force with the electronic structure of matter and need to come in direct contact via a collision with an atomic nucleus in order to have an effect on their surroundings. [31] Upon collision, two scenarios can arise: either the neutron will be captured by the nucleus or be scattered by it. After neutron capture, the mass number of the target nucleus will increase by one and the energy of the neutron will be absorbed by the nucleus. This can result in an unstable isotope or a nucleus being left in an excited state, both cases being capable of producing a range of secondary radiations in the form of charged particles (via beta decay, (n,p), (n, α) and other similar reactions), or gamma rays. [32]

The cross section for neutron absorption is generally higher at thermal neutron energies. Fast neutrons are generally more likely to scatter off a target nucleus, either exciting it during the collision (inelastic scattering) or leaving it in its ground state (elastic scattering). These mechanisms of reaction mean that if a neutron does interact then it is in one or more discrete events, such as several scatterings or a capture event. These properties contrast with the behaviour of alpha and beta particles which will continuously lose energy whilst they pass through matter, forming ionisation trails around their path, whereas it is possible for neutrons to pass through metres of matter before interacting by colliding with a [33] [34]

The relative infrequency of neutron interactions complicates the study of their behaviour, as the neutron itself has no means of inducing an electronic signal in a detector. Instead, the effects of secondary reaction products within a detector must be used to infer the presence and properties of neutrons. Neutron detectors operate by facilitating a reaction that will produce a charged secondary particle that can be easily detected such as a proton, beta particle, alpha particle or light ion. Neutron capture is the predominant mechanism for thermal neutron detection as the cross section for this reaction compared with that of scattering is high at lower energies. Neutron scattering off atomic nuclei dominates for fast neutrons and it is this reaction that is utilised in liquid scintillators. [32] [35]

2.2.1.1 Neutron scattering kinematics

Neutrons colliding with a nucleus will be scattered across a certain angle, the neutron will transfer a proportion of its energy to the nucleus which will recoil. The energy transferred to the recoil nucleus is a function of the scattering angle and the mass of the recoil nucleus. Figure 7 shows a neutron scatter diagram showing the same event in the laboratory (LAB) frame of reference and the centre of mass (COM) frame of reference¹. [34]

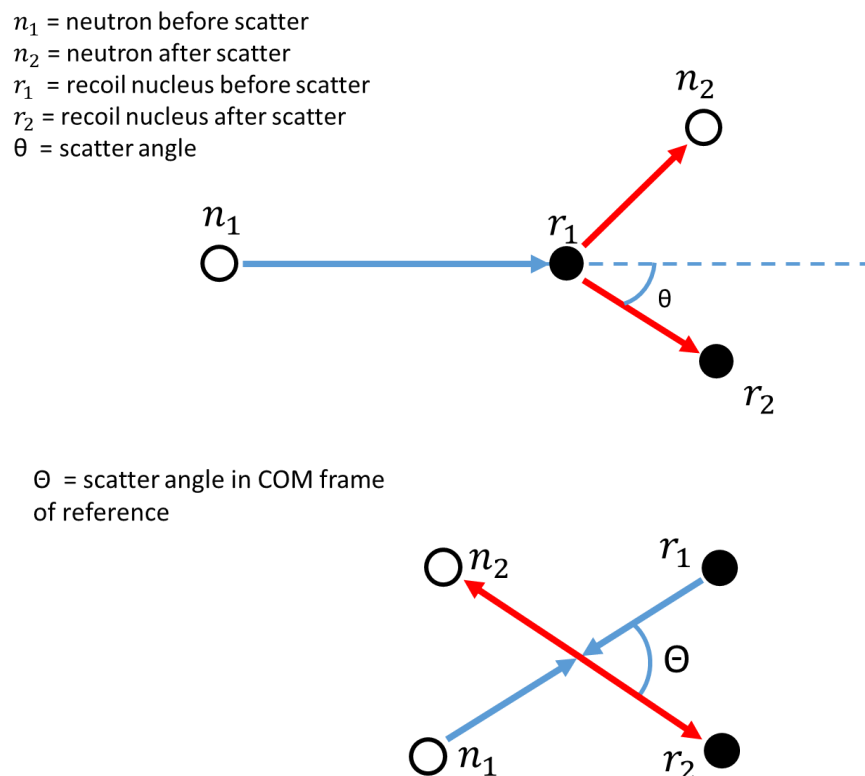


Figure 5: Kinematic diagram of (n,p) elastic scattering, in the LAB frame of reference (top) and COM frame of reference (bottom)

¹ In the LAB frame of reference particle velocities are taken from the point of view of the observer in the laboratory. As the neutron is moving at far higher velocities than the recoil nucleus (which will be travelling at thermal velocities) the nucleus can be considered static until after the collision. Conversely in the centre of mass (COM) frame of reference the centre of mass of the two particles is used as the stationary point. Both the neutron and nucleus will be moving toward this point with velocities with the same proportion as the proportion of masses of the two bodies. Using this frame of reference can make the kinematics of the reaction easier to treat mathematically.

By considering the conservation of energy and momentum, the energy transferred to the recoil nucleus during the scatter is:

$$\text{Equation 3} \quad E_r = \frac{2A}{1+A^2} (1 - \cos\theta) E_n$$

where E_r is the energy transferred to the recoil nucleus, A is the ratio of the nucleus to neutron mass, θ is the COM scatter angle and E_n is the energy of the incident neutron.

The following transformation can be used to calculate the energy transfer in terms of the angle through which the neutron is scattered in the LAB frame of reference:

$$\text{Equation 4:} \quad \cos \theta = \sqrt{\frac{1 - \cos\theta}{2}}$$

which gives:

$$\text{Equation 5:} \quad E_{n2} = \frac{4A}{(1+A)^2} (\cos^2\theta) E_{n1}$$

In the LAB frame of reference θ is used to denote the scatter angle of the recoil nucleus. From this result it can be seen that the neutron will impart a portion of its energy according to the scatter angle. To transfer a maximum amount of energy the neutron hits the recoil nucleus head on, and the nucleus recoils in the direction of neutron travel and a scatter angle of 0° . A “glancing” collision of the neutron will only impart a vanishingly small amount of the neutron’s kinetic energy, scattering the recoil nucleus at an angle close to 90° off the neutron’s direction of travel.

The actual proportion of energy transferred in a scatter event with a specific angle θ is dependent on the mass ratio of nucleus to neutron. The

larger the mass of the recoil nucleus the less energy is transferred to it, as dictated by Equation 5

The ^1H nucleus consists of one proton and is approximately the same mass as a neutron, therefore the neutron is able to transfer almost the entirety of its energy to a proton in a single event, whereas a neutron will scatter off a heavy nucleus without transferring much energy at all. Table 1 shows the maximum amount of energy transferable to different light nuclei in a single scattering event according to Equation 5.

Table 1: Potential energy transfer to different nuclei in elastic scattering events. From [36]

<i>Target Nucleus</i>	<i>A</i>	<i>Proportional energy transfer</i>
^1H	1	1
^2H	2	$8/9=0.889$
^3He	3	$2/4=0.750$
^4He	4	$16/25=0.640$
^{12}C	12	$48/169=0.284$
^{16}O	16	$64/289=0.221$

As stated above, neutrons will react in matter over several discrete events as opposed to charged radiation, which transfer energy more continuously via the ionisation tracks formed as they pass through matter. This has consequences when attempting to shield neutrons. Instead of being slowed in electron-rich, high-mass material, neutrons must be slowed via several recoil events in a moderating material. This means that the steps taken to shield a neutron field are starkly different to other forms of ionising radiation. Low-Z materials rich in light nuclei such as hydrogen, nitrogen, oxygen and carbon make the best neutron moderators, as high proportions of the neutron energy can be transferred in each recoil event.

Conversely, recoils in shielding designed for electromagnetic radiation (gamma rays, X-rays etc.), such as lead, will not remove much energy from a neutron and therefore it will not act as an efficient neutron attenuator. Indeed,

neutrons can travel through large amounts of concrete and lead shielding. [34] Polythene and water are commonly used to shield against neutrons. The addition of materials comprising elements with isotopes having a high thermal neutron capture cross section, such as boron or cadmium, improves neutron shielding by absorbing neutrons via neutron capture reactions once the neutron has been slowed to thermal energies via scattering interactions.

The relationship between recoil nucleus mass and energy transfer also has important implications for detectors which utilize neutron scattering reactions as a detection mechanism for neutrons.

2.3 NEUTRON DETECTION AND MEASUREMENT

As mentioned in the previous section, the only clue to the observer of the presence of neutrons is the effects produced by secondary radiations produced by the neutron as it passes through matter. In the following section, some methods of detecting neutrons and then measuring their energy will be explored. The first instance examined will be the proton recoil scintillator, being the device used in this research. There are a range of other methods which will be described afterwards.

Scintillation mechanisms have been used in radiation detection since the dawn of the field. [37] Scintillators exploit the fluorescent effect of secondary particles produced in a detector volume to indicate the presence of neutrons (and gamma rays) and infer some of the properties of these radiations. The secondary particle observed most often in liquid organic scintillators, such as EJ-309, is the recoil proton.

2.3.1 Proton recoil detectors

A neutron which scatters off a proton - a hydrogen nucleus - imparts some energy to the proton. If the incident neutron is fast, then the energy imparted will often be very much greater than the energy necessary to break the chemical bond holding the hydrogen atom in its molecular structure, thus freeing the molecular hydrogen nucleus and producing an energetic free proton. This energetic proton will now move through the scintillant, depositing energy via ionisation in the form of tracks of charge carriers. It is possible for the neutron to scatter off a subsequent nucleus, producing another recoil product as shown in Figure 6. Such multiple scatterings happen very rapidly, each contributing light to the total scintillation magnitude. Scatter events will happen until the neutron is thermalised, captured or leaves the detector volume.

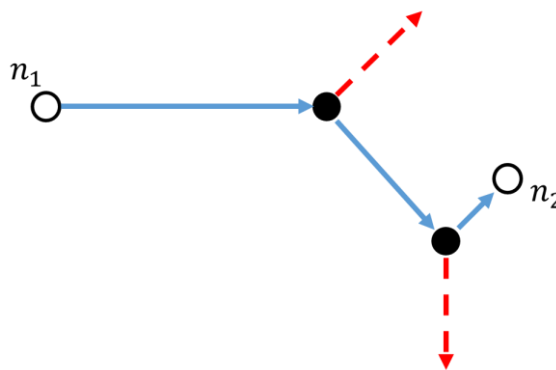
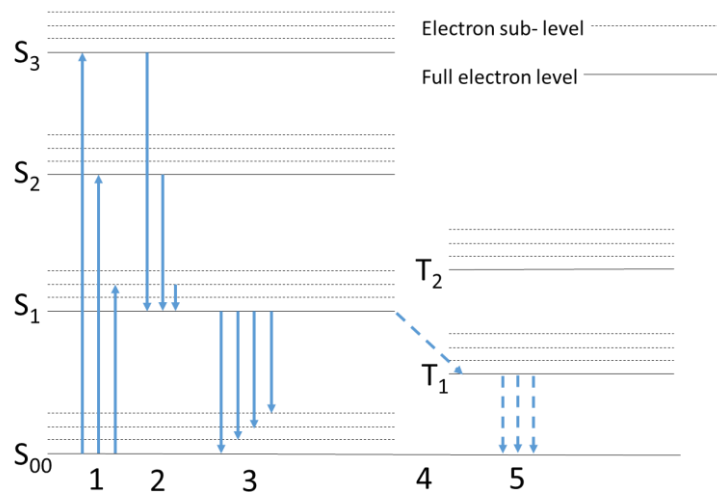


Figure 6: Illustration of Neutron scattering off protons in the detector volume from N_1 to N_2 . Blue arrows show track of the neutron and red dashed lines show the path of the recoil proton.

Of course, the neutron can scatter off any nucleus in the scintillant (or none at all and pass through undetected.) From Equation 5 it is clear that the energy transferred in a scatter is inversely proportional to the recoil nucleus mass. In order to improve signal strength and preserve spectroscopic information, it is desirable that energy transfer is maximised in each scatter. Effective detection media are therefore rich in low mass nuclides, such as hydrogen, oxygen and carbon: hence the effectiveness of organic liquid and plastic scintillators in this regard.

Scintillators are also sensitive to gamma rays. Whilst neutrons interact with the atomic nucleus, gamma rays are electromagnetic phenomena and can interact with the electron structure of the scintillant. Gamma rays primarily react via Compton scattering in organic scintillators, a discrete scatter event similar to the proton recoil experienced by neutrons. The primary difference is the resultant secondary particle, where neutrons produce energetic free protons, an incident gamma ray will produce a fast electron. Protons and electrons are both charged particles which may deposit energy in the scintillant via electromagnetic reaction as they pass through. For further information on gamma ray interaction in the scintillant, see Appendix A: Gamma interactions in the scintillator.



*Figure 7: Excitation and de-excitation diagram of electrons in the scintillant figure reproduced from [38]. Passing energetic charged particles excite the electron structure to one of the singlet states as shown at **1**. The singlet state excitations higher than level 1 will quickly de-excite via radiation less processes in **2**, to the 1st singlet state. De-excitation to ground happens in **3** and produces scintillation light. Intersystem crossing (**4**) causes excitation in the triplet states, which de-excite, producing light with a longer delay. (**5**)*

Scintillation light is produced via a process of excitement in the electronic structure of the scintillator substance. [38] As the secondary charged radiation loses energy to an ionisation track in the scintillator material, it produces a volume of high ionisation and excitation density. Delta rays produced by the initial secondary particle can exit the track producing extra “blobs” of ionisation and excitation off the ionisation track. Scintillation mechanisms rely on the excitation of the π -electron bond structure, found in

certain molecular arrangements. The benzene ring is an example of a molecule possessing such a feature, in that only a small number of the valence electrons are tightly associated with stronger σ -bonds and the rest are not bound to a particular atom and are available for excitation between π -electronic states. The π -electronic states are shown in Figure 7. Electrons can be excited in the singlet states (electron paired with spin=0) or triplet states (spin of one paired electron charges). These levels also have a finer set of excitation levels associated with vibrational states of the molecule. An electron can be raised into one of several singlet states via a passing charged particle, as shown by upward arrows marked 1 in Figure 7. Excitations higher than the first singlet state quickly ($\approx 10^{-11}$ s) de-excite via radiation less processes (2 in Figure 7) within the molecule to the first singlet state. They can also use a mechanism (intersystem crossing) to convert to the triplet states (4 in Figure 7). De-excitation between the first singlet state and the ground S-states results in the emission of a photon, at a wavelength dependent on the energy gap between S_1 and the vibrational level it de-excites too. Most de-excitations occur between smaller energy gaps than that of the S_0 - S_1 transition, meaning the photon cannot be absorbed via the excitation of another electron system in the scintillator. For this reason, the scintillator is highly transparent to its own scintillation light. S_1 - S_0 transitions happen very promptly, within nanoseconds, whereas triplet states decay much more slowly, over up to hundreds of nanoseconds. This two-component scintillation process produces asymmetric light pulses, as illustrated in Figure 7.

EJ-301 and EJ-309 are liquid scintillators which use p-xylene as a solvent, providing a ready source of hydrogen and carbon nuclei. The molecule contains a π -electron structure in its central benzene ring, giving the scintillator mechanism, as shown in Figure 8. Some of the properties of EJ-301 and EJ-309 are provided in Appendix B: Properties of EJ301 and EJ309.

EJ-301 and EJ-309 are popular due to their fast response, good sensitivity and their ability to discriminate between gamma rays and neutrons.

Being liquids, they are also more resistant to the crystal structure damage that solid crystal scintillators can experience when subjected to high radiation fields. [39] [40]

The response of EJ-301 and EJ-309 has been studied extensively and much work has been performed characterising the light output properties and efficiencies of these scintillators. The physics behind the response function is elucidated upon in the following section.

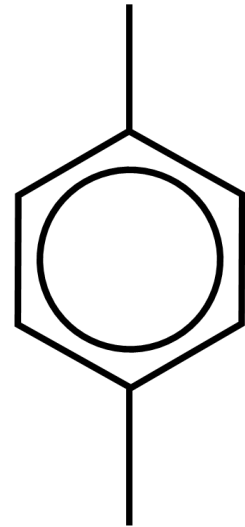


Figure 8: The chemical structure of xylene. The central benzene ring provides a scintillation mechanism.

2.3.2 Scintillator response

Every radiation detector will have a certain response to incident radiation that must be understood in order to interpret the measurements made with the device. The response of liquid scintillators is largely dependent on the kinematics of the neutron scatter process and the relationship between secondary particle energy and light production. [41]

As described previously, neutrons and gamma-ray photons traversing the scintillator chamber will not produce light due to their lack of charge but instead rely on recoil particles to produce their scintillation. The relationship between the energy deposited in the scintillator by the recoil particle and the number of light photons produced varies with the recoil particle.

The amplitudes of photon pulses generated by hydrogen nuclei are not linearly proportional to their recoil energy. Their light output has been characterised using a variety of empirical functions. A well-studied and commonly-used example is the Kornilov function [42]:

Equation 6:
$$L(E_p) = L_0 \left(\frac{E_p^2}{E_p + L_1} \right)$$

Where L is the light output in MeVee, E_p is the proton recoil energy and L_0 and L_1 are empirically-obtained constants that vary with the detector scintillant and geometry. The curve of this light production function is shown in Figure 9.

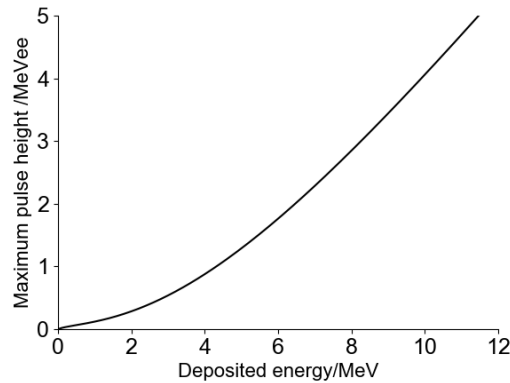


Figure 9: Light output curve for EJ309 scintillator based on the Kornilov function [42]. The curve was produced by fitting the curve to experimental data collected by the author via detector calibration measurements performed using a Van de Graaf accelerator at the National Physical Laboratory, Teddington. Monoenergetic neutrons produced via the ${}^7\text{Li}(p,n)$ and $T(p,n)$ reactions provided known energy responses with which to determine the relative light output per MeV deposited in the detector. Plot for informative purposes only and is not referred to henceforth.

Gamma radiation primarily generates scintillations as a result of a recoil electron, produced as a result of a Compton scatter event. The light output from an electron is proportional over the range of energies relevant in this work (>0.4 MeV). This relationship is useful as a basis for using the units of eVee (electron volt electron equivalent, equivalent to the pulse height produced by an electron with an energy of 1 eV) as a value for relating pulse height to particle.

2.3.2.1 Detector response to mono-energetic neutrons

As the light output from the scintillator is proportional to the energy of the recoil particle and not the neutron itself, the detector does not simply respond with a peak representing the incident neutron energy. Instead, the pulse height spectrum (PHS) produced in the detector by a mono-energetic source of neutrons will reflect a range of possible scatter scenarios in the scintillant. At the simplest level, the PHS will be a flat continuum of values, up to an edge at a maximum value. This continuum represents the range of scatter angles that can occur in a neutron–proton scatter event and is shown

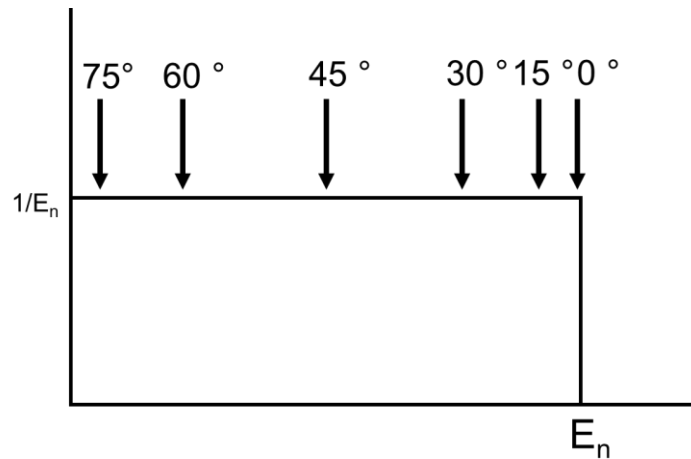


Figure 10: Illustration of the idealised rectangular pulse height distribution indicative of that which would be produced by varying scatter angles of the $n(\text{scatter},p)$ reaction. Angle of scatter indicated by the arrows across the top. Figure reproduced from [36]

in Figure 10. As a neutron can impart the entirety of its energy in one scatter event with a proton, the upper edge of the continuum represents the full energy of the neutron. The rest of the continuum represents the ability of the neutron to deposit any amount of its energy to a recoil proton, depending on the scatter angle. In practice, a number of other factors affect the PHS [35] [43]:

- Non-linear light output: As the scintillator light produced by the recoil proton follows the relationship shown in Figure 9, the PHS shows a skew toward low pulse heights as shown in Figure 11 (a).
- Wall effect: A recoil proton produced adjacent to the wall of the scintillator volume may escape the scintillator before depositing the entirety of the energy it has picked up from the neutron. Again, this will skew the PHD toward low pulse heights as shown in Figure 11 (a).
- Finite resolution: The inherent uncertainty of the light production and gathering process smears out some of the detail of the PHS, in a mono-energetic source this would manifest in rounding of the edges of the high energy cut-off as seen in Figure 11 (b).

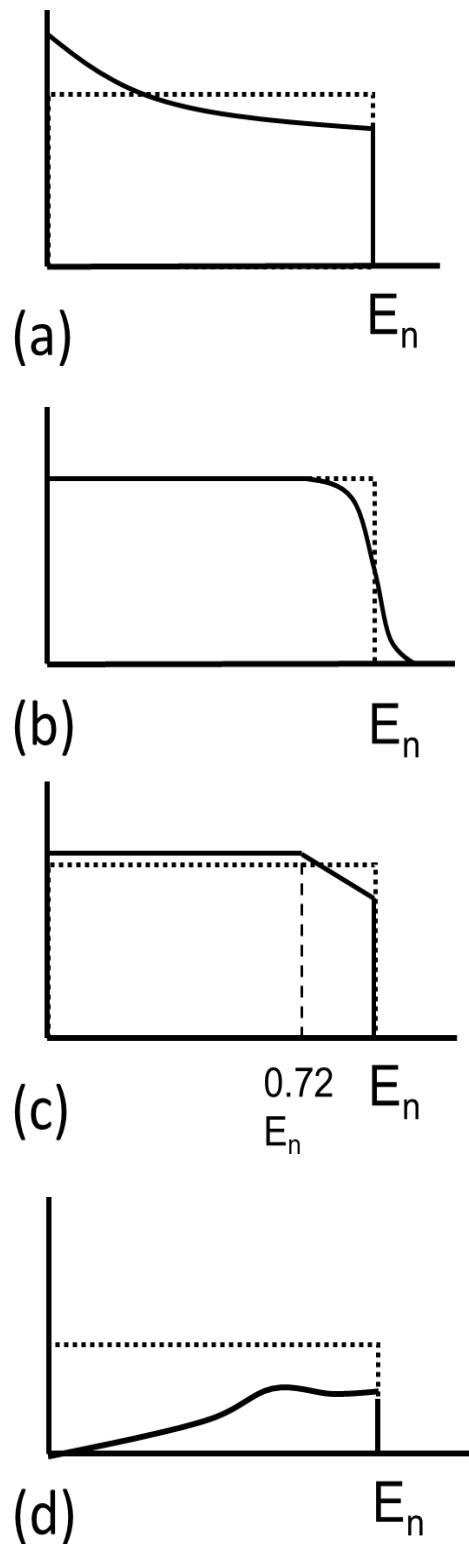


Figure 11: Diagram showing the effect of different contributions to the shape of the PHS. (a) shows the effect of non-linear light production in the scintillator, (b) illustrates the effect of detector resolution, (c) shows the effect of carbon scatters and (d) shows the contribution of multiple scattering events.

- Carbon scatters: As neutrons impart a far lower proportion of their energy to the heavier carbon nuclei, the scintillation light produced directly by carbon has a relatively limited effect on the PHS. Subsequent proton scatters however will still contribute, but with a lowered available energy after the carbon scatter. This results in a “missing” section of the PHS representing those neutrons which have lost energy in carbon scatters previously to the proton scatter. The maximum energy a neutron can lose to a carbon nucleus in a scatter is $0.28 E_n$ (from Equation 5) and so carbon scatters are apparent above $0.72 E_n$. Figure 11 (c) shows this effect on the PHS.
- Multiple scatters: In the flat rectangular “perfect” response, all of the pulses are produced in single neutron scatters off protons. After the first scatter has happened, it is still possible for the neutron to scatter again, producing another recoil proton. As the scatter and excitation process happens much faster than de-excitation and scintillation, the light produced by the second proton adds to the pulse height of the first event, rather than appearing as a separate event. The effect on the PHS is additional larger pulses, forming a hump behind the high energy edge of the distribution as shown in Figure 11 (d).

The combination of the above components produces a PHS for a mono-energetic neutron source like the one shown in Figure 12.

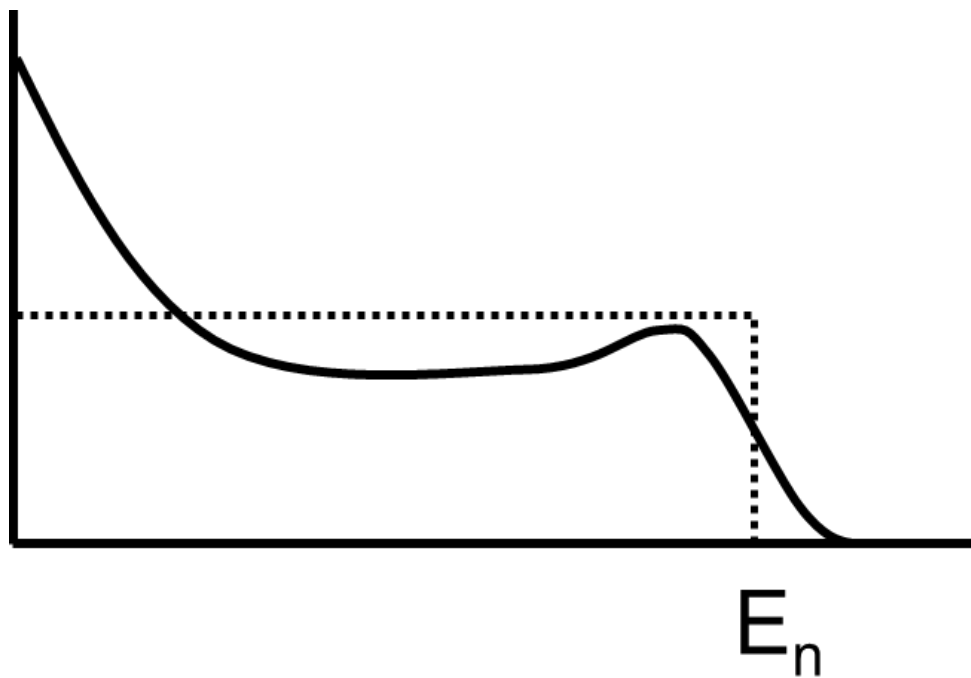


Figure 12: Illustration of the PHS produced in an organic liquid scintillator by a mono-energetic neutron source of energy E_n . The dotted line shows the distribution of energies deposited in the original simple treatment of single scatters off protons, the solid line shows the effect on the PHS of the other factors described above.

2.3.2.2 Pulse shape n/γ discrimination

Neutrons and gamma-ray photons elicit a similar response in the detector². As all sources of neutrons also produce gamma rays, a method of distinguishing between photon and neutron detections must be used to give meaning to any readings of either radiation. The pulses produced by neutrons and gamma rays are very similar, stemming from the de-excitation of singlet and triplet states in the scintillant. Energetic protons produced by neutrons typically deposit their energy in a shorter physical space in the scintillant than the electrons produced by gamma rays and will produce a higher proportion of longer-lived triplet state excitations. [44] This means that the pulses produced by neutrons take longer to decay for a given pulse height, as shown in Figure 13.

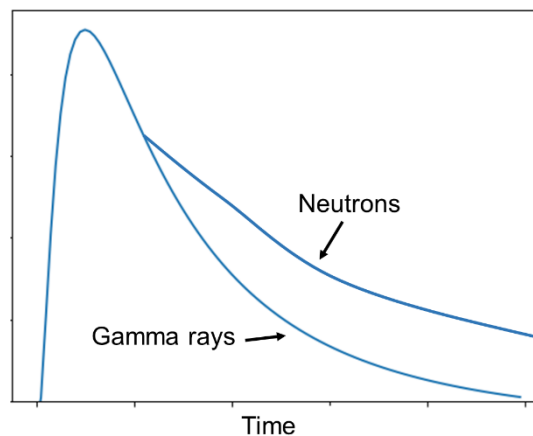


Figure 13: Illustration of pulse shapes for neutron and gamma induced detection events. The proton-mediated scintillations of the neutron give a longer decay tail than the electron produced pulses of gamma rays.

This subtle difference in pulse shape gives rise to a number of methods of discriminating between neutron and gamma-ray events, most commonly by integrating sections of the pulse providing comparison between the overall pulse magnitude to the tail magnitude. [8] [45]

² For a discussion of the mechanics of gamma ray interaction in the scintillator volume, see Appendix A: Gamma interactions in the scintillator.

2.3.3 Neutron spectroscopy with proton recoil scintillators

The relatively flat nature of the scintillator response to neutrons complicates the process of obtaining a source neutron spectrum. As there is no well-defined peak in the pulse height distribution produced by even mono-energetic neutrons, a simple relationship between the neutron energy spectrum and the pulse height spectrum in the detector cannot be assumed. This facet of detector behaviour necessitates the using of some process to separate the desired energy information from the detector response.

A comprehensive review of the mathematics behind spectrum unfolding is given by Matzke [46] . For our purposes, a brief overview of the concepts and approaches behind spectrum unfolding is sufficient to understand the process and some of its nuances.

The pulse height spectrum produced in the scintillator is a convolution of the source energy spectrum $\Phi_E(E)$ and the detector response function $R(E)$, a relationship that is described by the following equation:

Equation 7
$$N_k + e_k = \int R_k(E)\Phi_E(E)$$

where N_k is the number of counts in channel k , $R_k(E)$ is the detector response in channel k to incident neutrons of energy E , e_k is a term accounting for the various uncertainties, i.e., counting statistics, poorly defined responses etc. As can be seen from the expression, the response in any particular channel is an integration of contributions from across the whole energy spectrum $\Phi_E(E)$, and the process of obtaining $\Phi_E(E)$ from a set of measurements involves unfolding the measurements and the response. From this observation alone the difficulty in performing fast neutron spectroscopy can be appreciated: we know from the kinematics of the scattering process that the energy deposited by a given neutron is stochastic across a range of values, and so a particular initial energy cannot be assigned to a specific neutron from the signal it produces in the detector. The neutron spectrum must therefore be determined stochastically from the observed response and with a certain amount of *a priori* information.

The task of unfolding neutron measurements is usually begun by describing the relationship between N_i and Φ_E in terms of a discrete matrix equation [46]:

Equation 8
$$N_k = \mathbf{R}_{kj}\Phi_j$$

As before, \mathbf{N}_k is the counts in channel k of the pulse height spectrum although now expressed in a column vector with each entry representing a channel. The terms \mathbf{R} and Φ now represent a matrix and a vector, respectively, Φ being a vector containing each channel of the solution spectrum and \mathbf{R} being a $k \times j$ matrix containing a characterisation of the detector response in different channels across the full energy spectrum. At first glance what is given is a matrix inversion problem, yet herein lies the primary difficulty of neutron spectrum unfolding, as the solution for \mathbf{N}_k is highly ill-conditioned, since the true spectrum is just one of a great many possible solutions.

2.3.3.1 Detector characterisation and response measurement

In order to unfold the neutron spectrum using Equation 8, the detector response matrix must be obtained. This is a relatively involved process which must be performed to a high level of accuracy to obtain reliable results. Detector calibration typically involves a combination of modelling work and characterisation with neutrons of known energy; the kinematics of neutron scattering within the detector can be accurately modelled using cross section data within Monte-Carlo calculations, the finer points of light production and detection on the other hand cannot. Modelling can be performed using either general purpose Monte-Carlo modelling software such as MCNP, or via purpose made detector modelling packages [47] [48] [49] [50] [51]. Detector characterisation involves quantifying the effect that the various aspects of the detection mechanism have on the response of the detector.

Traditionally, the light output per unit energy deposited in the detector and the detector resolution are measured by irradiating it with neutrons of known energy and observing its response. [47] [48] [49] This information is then fed back into a model to calculate the response function of the detector across the desired energy range. Although there are no radionuclide sources of mono-energetic neutrons, in the sense of the dependence describing a Dirac delta function, the closest to this ideal is achieved by producing neutrons with reactions in an accelerator. The method of using measurements to produce and verify a model of the detector response is powerful in that it allows the response at any energy across a range, and even the response to a particular poly-energetic source. Modelling the response over a particular energy structure can also make the unfolding process simpler, as the size of the response matrix can be tailored to match the energy bin structure of measured or solution spectra.

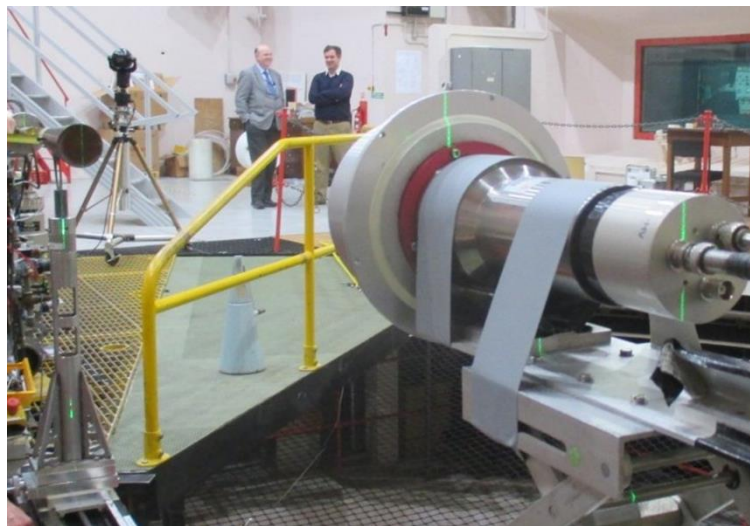


Figure 14: A liquid scintillator set up in front of the reaction target of a Van de Graaf generator for mono-energetic neutron irradiation. Photograph author's own.

Knowledge of neutron energy on an event-by-event basis can only be obtained via time-of-flight methods, typically via the use of a pulsed or chopped accelerator source. Either is usually a time consuming and expensive process and unsuited to portable measurements of workplace fields.

An alternative to the use of an accelerator is time-of-flight detector characterisation using fission sources. Using this approach, a separate detector is used to obtain a timing (trigger) signal for a fission event, and the energy of the neutron can be calculated from the time of flight [52] that elapses prior to it being detected, relative to that of the trigger signal. Accumulating pulses produced by neutrons with the same time of flight gives the pulse height distribution for a given energy.

TOF detector characterisation set-ups vary according to the choice of radiation mechanism exploited for the start signal and also the type of detector used in the start and stop positions. Ionisation chambers used to detect fission fragments have been used successfully, as have scintillators triggered by correlated fission particles, and scatter of a single neutron between detectors [53] [54] [11]. As well as not requiring accelerator facilities, an advantage to this approach is that, as neutron sources produce neutrons across the detector response, the whole response function can be determined in a single measurement. The resolution of the response function obtained only limited by the precision with which the particle flight can be timed and the time available to make the measurement.

2.3.3.2 Spectrum unfolding

Without a very well characterised and detailed understanding of the detector response, a probabilistic approach must be used to estimate the most likely solutions. To get the best results, the estimation process must not only take into account a mathematical treatment of the measured data, but also as much *a priori* information as the measurer can account for. A wide variety of unfolding codes and procedures exist, but in general an effective unfolding process should [55]:

1. Produce a stable solution
2. Provide only one valid solution
3. Reject unphysical solutions
4. Provide estimation of errors propagated through from the various inputs.

The matter of incorporating *a priori* information into the unfolding process is one that requires an amount of judgement on the part of the researcher. At the simplest level, *a priori* information can be the steps taken within the unfolding process to satisfy condition 3, ensuring that the solution spectrum remains physical. Often this entails preventing the inclusion of negative values or suppressing the tendency of many unfolding codes to produce strong oscillations in the solution spectra. Many codes require *a priori* information in the form of a starting spectrum. This can simply be a flat distribution, or if the approximate shape of the source spectrum is known then this can be included as an initial guess spectrum. The ISO standard spectra for ^{252}Cf or AmBe are other possible seed spectra to begin unfolding if the identity of the source is known. The scientist performing the measurements is not restricted to a single choice of *a priori* information, and comparison between results unfolded from different initial guess spectra can aid in evaluating the convergence process. [56]

In addition to *a priori* information being used to generate the solution, it can also be used to determine the nature of the solution itself. In Bayesian analysis, a parameterisation of the solution spectrum is used, for example a particular dose produced by a workplace field or the FWHM of the energy peak of neutrons produced in a fusion plasma. [57]. Applying Bayes' theorem allows a probability to be calculated that the neutron spectrum measured would produce a given set of parameters using a likelihood function incorporating known behaviour of the detector. [58]

A large body of work has been built up by authors over many years on the subject of spectrum unfolding, devising a multiplicity of different unfolding codes and procedures. [59] [60] [61] Despite the large number of codes and programs, they utilise the same core mathematical mechanisms attempting the same mathematical aim: finding the spectrum that when multiplied by the response matrix gives best agreement with the measured data. [62]

Amongst the approaches to solving the ill-posed problem of spectrum unfolding are iterative least squares fitting and maximum entropy methods as some of the oldest and most commonly used approaches. Least squares and

maximum entropy unfolding algorithms are variations of regularisation unfolding methods. [61] This approach takes a starting spectrum and attempts to adjust it to best match the observations made with the spectrometer, according to the relationship with the response function. [63] This is often an iterative process using a metric such as a form of a chi squared statistic based on *a priori* information, and the relationship between the response and the source spectrum, to evaluate the best solution.

Maximum entropy algorithms are a regularisation approach which use the principle of maximum entropy to evaluate the solution spectrum, again using *a priori* information in the form of an initial guess spectrum. [59] [58] Informational Entropy is a measure of uncertainty, by choosing a solution spectrum that maximises the entropy between the solution and the *a priori* spectrum, the algorithm is introducing the least amount of information which does not come directly from the measurements and input spectrum. The maximum entropy method was developed as a way of including *a priori* information in a consistent and general fashion.

Various machine learning algorithms have been used to unfold neutron energy spectrum measurements including, in particular, artificial neural networks (ANNs) and genetic algorithms. ANNs have been used successfully to discriminate between different sources but are still outperformed by least squares methods. [64] [65] Additionally, it is difficult to account for the uncertainties in the solution spectrum, consistently. Genetic algorithms have also been used to unfold a variety of spectra successfully. An advantage of this technique is that it does not need an initial guess spectrum to begin unfolding, but when good knowledge of the measured spectrum is known, better results can be obtained with maximum entropy methods. [66]

One of the major limitations of many unfolding algorithms is the inability to consistently evaluate the uncertainty associated with the unfolded solution spectrum. [46] Whilst this does not preclude their use in many applications, it does attach the requirement of experience and interpretation when it comes to using their results. [67]

The unfolding of neutron spectra from pulse height distributions in proton recoil detectors is a useful and varied field of research. There are several limitations associated with the technique however:

- A not inconsiderable amount of skill and effort is required when it comes to preparing the response function of the detector, input data, and any initial guess spectrum used in the calculation.
- The solution spectrum can be highly dependent on the amount of *a priori* information available and the judgement of the user when incorporating this into calculations.
- The propagation of uncertainties can be inconsistent.

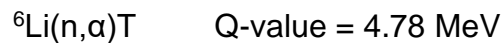
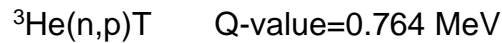
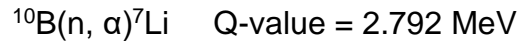
Liquid scintillators are not the only instrument whose measurement results require unfolding. Observations made with many other instruments with non-trivial responses to neutron fields can and have been unfolded to perform neutron spectroscopy. Other instruments which can be used to measure neutron energy spectra will be explored in the next section.

2.3.4 Nuclear reaction detectors

There are several alternative detection mechanisms available for converting the energy of a neutron into a form that which can be detected and measured. Several nuclear reactions are used in neutron spectrometry utilising a variety of detector constructions. These reactions produce energetic charged particles as secondary radiations which can be detected much like the recoil proton in an organic scintillant. In addition to nuclear reactions, neutron activation of elements has also been used to perform spectroscopy in a process which will be described in the following sections.

2.3.4.1 Nuclear reactions in neutron detection

There are three reactions which are particularly relevant to the field of neutron detection [68] [69]:



The $^{10}\text{B}(n,\alpha)$ reaction is often exploited for measurements at thermal and can be used to detect fast neutrons after they have been moderated by an appropriate material. [70] The $^3\text{He}(n,p)$ and $^6\text{Li}(n,\alpha)$ are also used to detect both fast and thermal neutrons and are used in various spectroscopy applications.

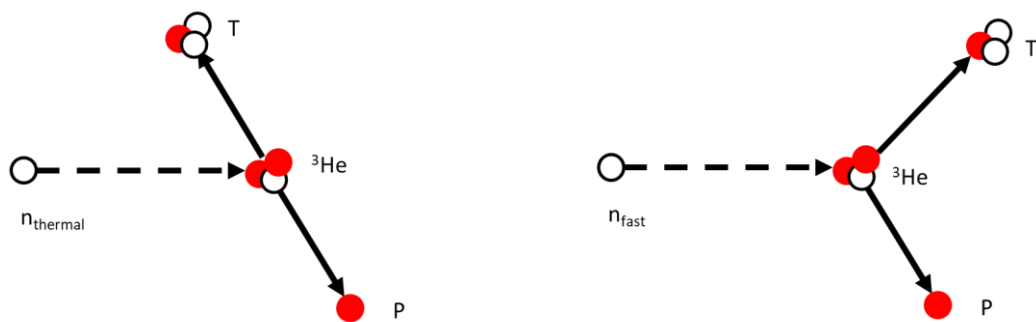


Figure 15: Illustration of the $^3\text{He}(n,p)\text{T}$ reaction at thermal (left) and fast (right) incident neutron energies. In the case of the thermal neutron the energy of the reaction products is Q, and they are emitted in opposite directions. When a fast neutron is involved, its momentum is retained with the reaction products along with the energy associated with the Q-value, resulting in the scenario on the right. Reproduced from [68].

The two fundamental differences between neutron *capture* reactions and *scatter* reactions are the positive Q-value and the fact that the reaction will produce two reaction products, with the entirety of the energy of the incident neutron. The positive Q-value indicates that the reaction is exothermic, and the secondary products receive energy from the reaction as well as the energy of the neutron. Most basically, this indicates that even thermal neutrons with negligibly low energies will produce reaction products of at least the Q-value. This has advantages as it raises the energy of the products of low-energy neutron events well above noise and the signal level of

gamma-ray interactions, offering some reaction detectors an element of in-built n/γ discrimination, via their immunity to gamma-rays.

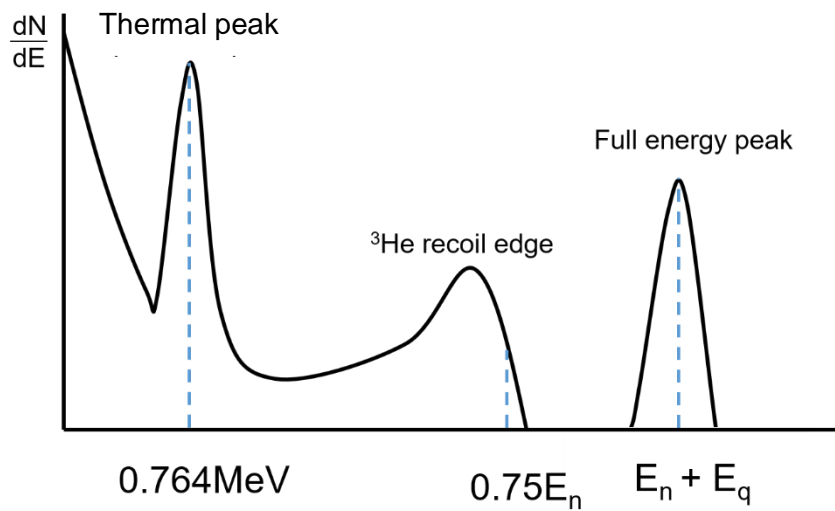


Figure 16: Illustration of the energy distribution of charged particles produced in a ^3He detector irradiated with mono-energetic fast neutrons of energy E_n , reproduced from [68]

The response of reaction detectors to fast neutrons contrasts with that of the proton recoil detector in several ways. Figure 16 shows an idealised energy distribution in dN/dE , or counts per unit energy, of charged particles produced in a ^3He detector. Like proton recoil detectors, the recoil edge associated with neutron scatter is present, although in this case it is scatter off a ^3He nucleus rather than a proton, and therefore is only $0.75E_n$. The major difference from the spectrum produced in a purely recoil detector is the presence of the full energy peak, representing the energy possessed by the reaction products of the capture reaction, plus the energy E_n of the incident neutron. Finally, the thermal peak contains events corresponding to reactions involving neutrons that have been captured after thermalisation, producing reaction products with energy equivalent to the Q-value of the reaction.

Not shown in Figure 16 is the wall effect. In the same manner as a recoil proton hitting the wall of a scintillator before it has had the chance to deposit its energy, the reaction products in a reaction detector can be lost at the wall of the detector. Like the case of the scintillator, this produces a continuum of events where decreasing amounts of energy are deposited in the detector. When thermal neutrons are captured, there are two reaction products and thus two possibilities to lose one to the detector wall. This

produces a two-step wall effect around the reaction peaks, as shown for the $^{10}\text{B}(n,\alpha)$ reaction in Figure 17.

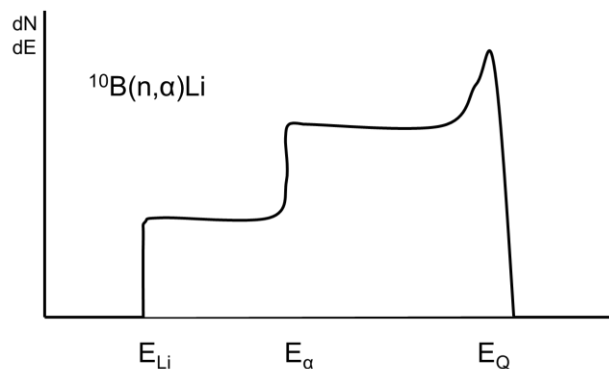


Figure 17: Illustration of the wall effect seen in the detector response of $^{10}\text{B}(n,\alpha)$ detectors. (not showing the effects of different energy states of the ^{10}B nucleus) Reproduced from [68]

The wall effect can act as a limit on the energy ranges of detectors, particularly those which absorb reaction energy within a gas. The wall effect can be minimised with bigger detector volumes, minimising the probability a reaction product will reach the wall, or by adding a heavy gas such as argon to shorten the path of the charged reaction products.

2.3.5 Fast neutron spectroscopy using reaction detectors

The design of a nuclear reaction detector involves two main considerations: a vessel containing the reaction nuclide of interest in a convenient form and a means of absorbing the energy of the reaction products and converting this into a measurable signal. There are many ways of achieving these ends and many subtle design features that can improve the efficiency or utility of a neutron spectrometer. The following sections discuss some of the devices that have been used, both in the past and more recently, to detect and measure fast neutrons.

2.3.5.1 Ionisation chambers

Ionisation chambers have long been used for neutron spectroscopy, along with many other radiation measurements. Whilst their use in many fields has

declined in preference of solid-state detector technology, they remain useful for high-resolution neutron energy measurements. ^3He gas is utilised to exploit the $^3\text{He}(n,p)\text{T}$ reaction to produce ion trails which yield a signal across a cathode and anode held at a potential difference. Ionisation chambers can also include a grid assembly to increase the energy resolution; another advantageous property when performing neutron spectroscopy.

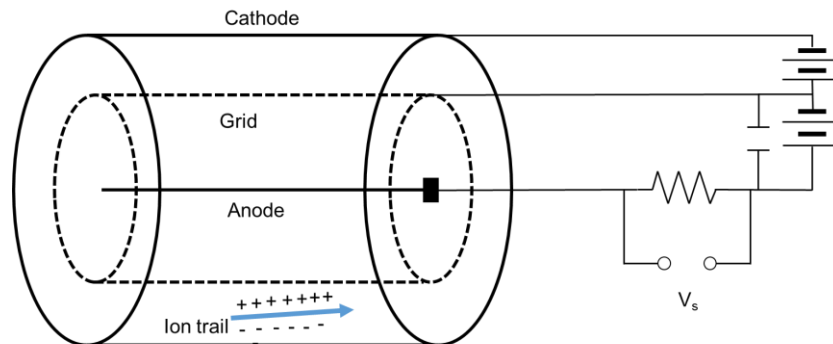


Figure 18: Schematic representation of the operation of a gridded ionisation chamber. In its simplest form an ionisation chamber simply requires the anode and cathode with an appropriate potential difference between the two. Ion pairs produced between them will drift to the electrodes producing a signal in the detector. The inclusion of the grid removes the component of the signal produced by positive ions and the first part of the electron's drift. Subsequently the signal only varies with ion track length, removing variance of the signal with the point of ionisation and improving resolution.

The use of ^3He gas gives a neutron response as shown in Figure 16, with the possibility of the full energy of the neutron to be transferred to the reaction products. The inclusion of the full energy peak is advantageous when unfolding neutron spectra, although scattering events must still be accounted for, either by inclusion in an unfolding calculation or, more recently, by event-by-event filtering using pulse rise time analysis [71] [72]. Pulse shape analysis can be used to discriminate neutron events from background counts from other radiations.

As well as use as a direct neutron spectrometer, ionisation chambers can be constructed with thin layers of fissile material deposited onto foil cathodes in the instrument itself. The twin, back-to-back ionisation chamber (TIC) is an example of an instrument which, when used in laboratory settings, has enabled observations of fission fragment distributions. The measurements can be extended to cover the prompt fission neutron energy spectrum by using the ionisation chamber signal in coincidence with a separate neutron detector, thus allowing neutron energy measurement via time-of-flight measurements [73]. More recently, a specialised multiple independent anode construction in conjunction with analysis of fission fragment position and energy distribution has provided neutron energy and multiplicity measurements in a single detector. [74]

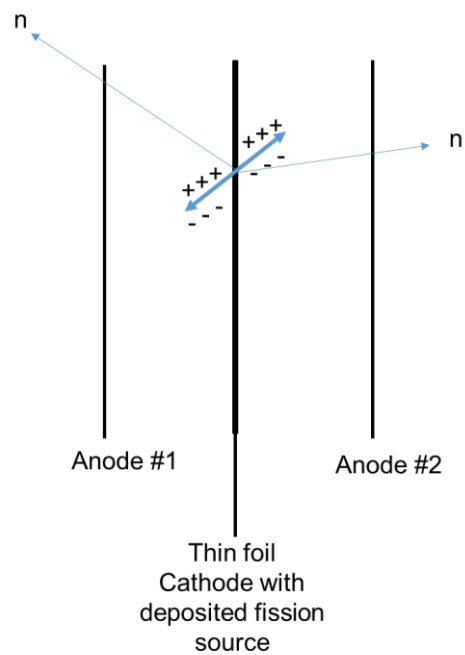


Figure 19: Schematic representation of a Twin back to back ionisation chamber (TIC). Two separate anodes share a common cathode deposited with a thin layer of fissile material. Fission fragments are emitted into the ionisation chamber where their respective energies can be measured. Unless a suitable fill gas is used then neutrons will escape the detector.

2.3.5.2 Proportional counters

Proportional counters of various fill gasses and geometric arrangements are another commonly-used instrument for performing neutron counting and spectroscopy [75] [76]. The ${}^3\text{He}(n,p)\text{T}$ and ${}^{10}\text{B}(n,\alpha){}^7\text{Li}$ reactions are both utilised in neutron detectors and are particularly well suited to the detection of thermal neutrons due to their high absorption cross section in that energy and positive Q-values. [77] $\text{B}(n,\alpha)$ detectors use boron trifluoride (BF_3) gas and ${}^3\text{He}$ gas is usually used with a buffer gas such as CO_2 , CH_4 or Kr to decrease charged particle range in the gas and reduce the wall effect. [78] [79] A boron-lined proportional tube, with a different fill gas, is another way of

using the $^{10}\text{B}(n,\alpha)^7\text{Li}$ reaction without BF_3 due to its toxicity. Although ^3He -filled proportional tubes have been used as fast neutron spectrometers, the use is uncommon outside the laboratory as the thermal peak can dominate the response, since the detection efficiency at thermal energies is considerably higher than for fast neutrons. [80] Figure 20 shows the cross sections for ^3He scatter and capture. To measure fast neutron fields, ^3He or ^{10}B proportional counters are more commonly used as the thermal detector at the centre of moderated detectors described below. Utilising the lower cross section at thermal energies, nitrogen gas has been used in a proportional counter to perform fast neutron spectroscopy of radionuclide sources, using the $^{14}\text{N}(n,p)^{14}\text{C}$ and $^{14}\text{N}(n,\alpha)^{11}\text{B}$ reactions, albeit with a strong contribution from the wall effect. [81]

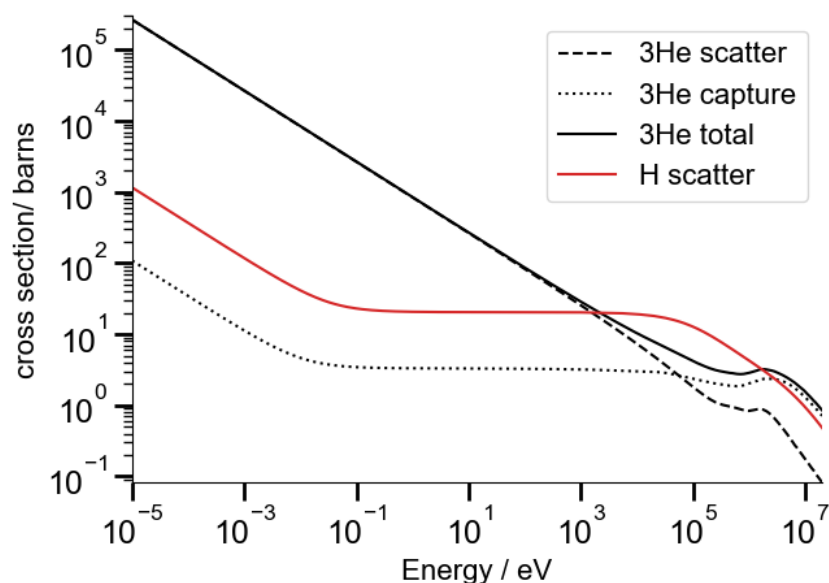


Figure 20: Cross sections for neutron capture in ^3He , along with scatter on ^3He and ^1H . Data taken from ENDF/B-VIII.0

Used as fast neutron spectrometers, proportional counters have also been used to measure the energy deposited by neutrons via scatter reactions in ^1H , ^4He gas in elastic scatter reactions, requiring a similar characterisation process and unfolding of the recoil edges as a recoil scintillator. [77]. Recoil-based, He-gas proportional counters are limited to use below around 5 MeV

incident neutron energy as the poor stopping power of He gas means that the wall effect becomes a hindrance at higher recoil particle energy. [82]

2.3.5.3 Bonner spheres

Bonner spheres are a common component of a specific design of neutron spectrometer. [83]

Together with a detector, they provide an instrument with a wide useful energy range and isotropic response, a particularly useful attribute when measuring workplace neutron fields. [84] [69]

They are also used in studies of the cosmic neutron background.

[20] Bonner spheres consist of a set of spheres made from hydrogen-rich materials (high-density polyethylene), with a small thermal neutron counter in the centre. Neutrons hitting the sphere

will scatter in the moderator until they are thermalised or escape the sphere.

Thermalised neutrons at the centre have a reasonable chance of being detected and producing a count. A set of spheres of different thicknesses provides the user with a number of different detectors with a set of response curves that vary with moderator thickness. Measurements with Bonner spheres consist of a single count number from each sphere, and an unfolding process not unlike that performed for proton recoil detectors is used to construct the source energy spectrum from the set of counts, the response functions of the spheres, and *a priori* knowledge of the neutron field. [85]

The instrument was originally developed by Bramblett et al., (the team including Bonner himself, for whom the spheres are named) using small $\text{LiI}(\text{Eu})$ scintillators. [86] Since then a variety of central detectors have been used: ^3He proportional counters are common and BF_3 proportional counters

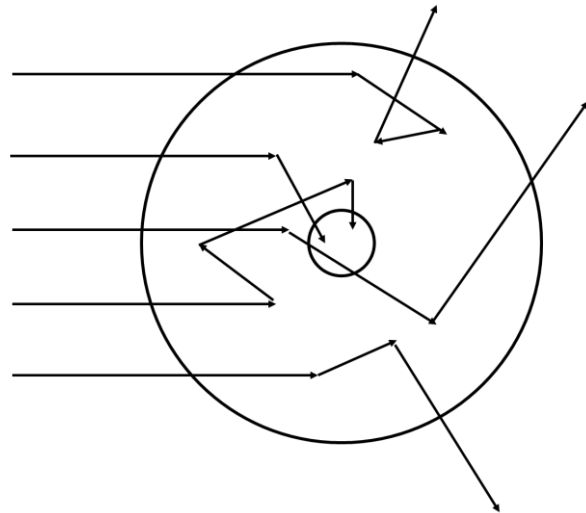


Figure 21: Schematic representation of a Bonner sphere. The hydrogen rich neutron moderator thermalises fast neutrons via scattering events. Thermalised neutrons then have a higher chance of detection in the central detector volume. Different thicknesses of moderator provide different efficiency distributions with respect to energy.

have been used as well. Recent research has also used solid state thermal neutron rate detectors successfully within Bonner spheres. [87] Measurements have also successfully been performed using different activation foils as the neutron counter. Foils, whilst somewhat inconvenient for general use, offer several advantages in certain situations, including immunity to pulse pile-up and oversaturation limitations when measuring intense neutron irradiations, and lack of sensitivity to high photon fields. [88] [89]

Novel, single-instrument, Bonner-style instruments have been developed, placing a number of detectors at different points within a single moderating sphere, enabling single instrument measurements to be made. [90] [91]

2.3.5.4 Inorganic and gaseous scintillators

Organic liquids are not the only substances that can be used as scintillators for the detection of neutrons. Various other scintillator materials and mixtures of materials have been used successfully as neutron spectrometers. All scintillators use a similar general construction, featuring a material that scintillates upon irradiation within a light-tight chamber. This is coupled to a sensitive light detector, traditionally a photomultiplier tube but some modern scintillators have used solid state alternatives, such as silicon photomultipliers (SiPMs). [92] [93]

Both recoil and capture reactions can be used to produce energetic, charged, secondary radiations which will induce scintillations. In the same realm as proton recoil scintillators, the use of ^4He as a recoil detector has been reported, developed in response to the shortage of ^3He , as a neutron spectrometer sensitive to and preserving the energy information of fast neutrons. [94] As in all gas-based detectors, raising the pressure of the fill gas increases the number of reaction targets available to neutrons and therefore increases detection efficiency. The ^4He scintillator uses ^4He gas as both a source of recoil nuclei and scintillator material, producing a similar response to proton recoil scintillators but with recoil edges on the PHS reflecting the lower maximum energy that can be transferred in an ^4He (n, elastic) scatter event. An unfolding process identical to that performed with

proton recoil scintillators is required to obtain the source neutron distribution [95]. One advantage of using the gas is the relatively low electron density, giving a relatively low gamma-ray sensitivity.

^3He has also been used in scintillators although its relative expense and recent shortage of supply have precluded its extensive use in recent years. [96]

^6Li does not have a gaseous form and is instead used as a component in solid scintillator crystals. Lithium iodide crystals doped with thallium or europium are commonly used scintillators, containing a significant quantity of lithium and a structure in which the reaction products (an alpha particle and a triton) deposit their energy, producing scintillations. [97] These scintillators are particularly sensitive to thermal neutrons, and are often used with moderation in integral spectroscopy arrangements to perform fast neutron spectroscopy, as described in the previous section on Bonner spheres.

Scintillators are also often doped with various combinations of additives to increase light yield or tailor the response to different energies of neutron or photons [98] [99] [100]. Scintillators are also built into different shapes and arrangements for different applications, for example, large sheets or into fibres. [101]

2.3.5.5 Sandwich spectrometers

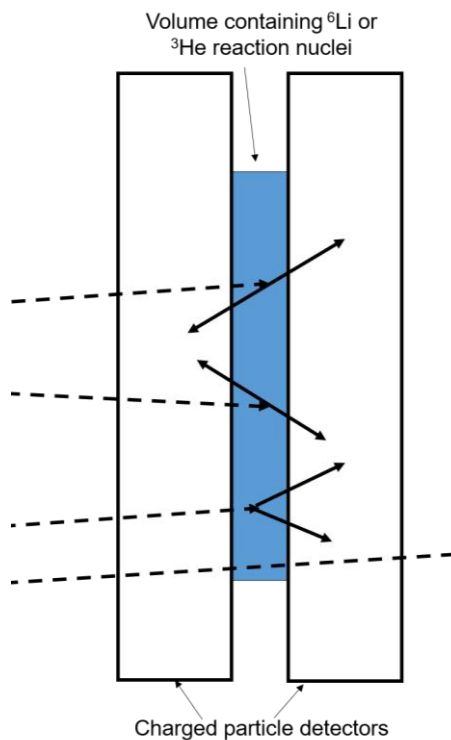


Figure 22: Schematic illustration (not to scale) of a sandwich spectrometer. The central area contains reaction nuclei such as ^3He or ^6Li . The secondary charged particles produced during capture reactions are detected in the detection regions on either side. Using coincidence counting, background counts can be greatly reduced and the full energy ascertained.

Sandwich spectrometers are another means of measuring the neutron field using nuclear reactions. As the name suggests, the sandwich spectrometer consists of a reaction product filling sandwiched between two charged-particle detectors, as illustrated schematically in Figure 22. In a similar mode of operation as the twin back-to-back ionisation chamber, the two reaction products are emitted in opposite directions into the two detector areas. Running the two charged-particle detectors in coincidence mode affords a degree of immunity to noise, as uncorrelated, background counts will typically only register in one side.

Additionally, summation of the two coincident pulses allows the full energy of the incident neutron to be measured.

Choosing the thickness of the central reaction material is largely a trade-off between providing sufficient thickness to provide reasonable efficiency, without too much of the energy of the reaction product being absorbed before they reach the detector areas. At high neutron energy, enough momentum from the incident neutron is transferred to the products to cause them both to end up in one detector, leading to lowered efficiency as energy increases.

Both ^6Li and ^3He have been used as reaction targets in the centre of sandwich spectrometers. Lithium, being a solid at room temperature, is deposited on thin substrates between detectors, as shown in Figure 22. There are a range of charged particle detectors which can be used in sandwich detector construction. Recent research has made progress using diamond detectors

around a deposited ^6Li neutron converter layer, to constitute a neutron spectrometer that is both environmentally robust and radiation-hard. The thinness of the sensitive layer however means their effectiveness is optimised in high-flux applications, such as reactor dosimetry and fusion diagnostics. [102] [103]

Being gaseous, ^3He must be contained in a volume and is particularly effective when this volume is run as a proportional counter alongside the charged particle detectors on each side. This setup, first reported by Kluge and Wiese, [104] is particularly effective as a spectrometer as it gives the best chance converting the full energy deposited by a neutron into a signal as energy deposited in the reaction gas still adds to the signal. Observing coincident pulses in the proportional counter and the two semiconductor layers allows differentiation between true events and background detections. The ^3He sandwich spectrometer has been used for characterising reference neutron sources. [105] Like many detectors utilising the $^3\text{He}(n,p)\text{T}$ reaction, the high cross section at thermal energies can pose a problem when making measurements, as the thermal neutron contribution can swamp the detector response.

2.3.5.6 Activation foils

Activation foils can be used in integral spectroscopy methods to construct the neutron energy spectrum in a similar methodology as is used with Bonner spheres. As mentioned in section 2.3.5.3, activation foils with a high cross section for activation by thermal neutrons can also be used as the detector in the centre of Bonner sphere sets. [88] [89] Foils made from materials which have an energy threshold to neutron activation can also be used directly as an integration spectroscopy system; the relative activations of a set of foils with different thresholds can be unfolded to calculate the neutron energy spectrum. Many of the unfolding codes used for Bonner spheres or scintillators are also used when unfolding foil activation measurements. [106] [107] As mentioned previously, foils provide spectroscopic capabilities where neutron fluence rates would overpower other detectors. Similarly, they are useful when neutrons are produced alongside very high gamma-ray fluxes resulting in them being a popular choice when measuring reactor or medical accelerator fluxes. [108]

[109] [110] Another advantage is that they are unpowered, minimising time spent setting up and arranging power supplies. This can be a desirable quality when taking measurements in high dose areas.

Activation foils share disadvantages with most integral spectroscopy systems, in that they have poor resolution and there is an amount of uncertainty in the unfolding process. In addition, there is the counting process involved in measuring the activation which, depending on the decay constant of the induced activity, must be performed within a certain time after irradiation, adding complexity to the measurement process.

2.3.6 Time-of-flight neutron spectroscopy

In the previous section 2.3.3.1, the use of time-of-flight measurement to establish neutron energy for purposes of detector calibration was described. When characterising a detector, the time of flight of a detected neutron can be used to measure the full energy of the neutron independently of the amount of energy it deposits in the detector. The logical extension of this technique is to take the neutron energy as the value being measured and construct the neutron energy spectrum from this information. Figure 23 illustrates the principle of TOF spectroscopy.

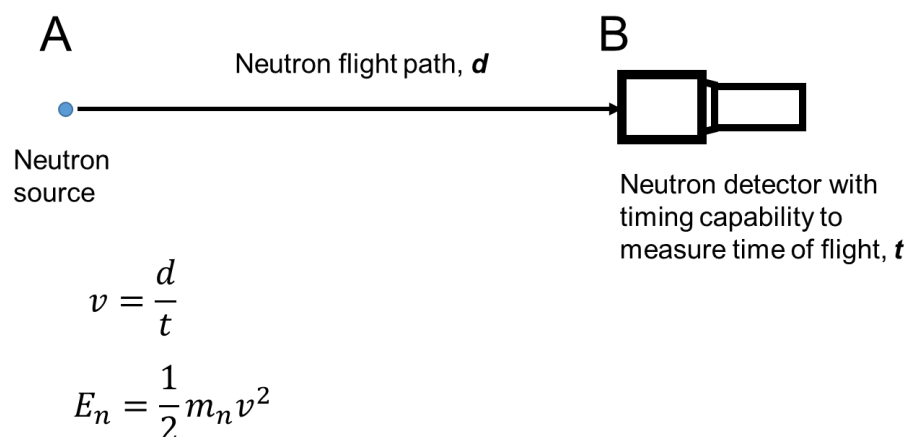


Figure 23: The principle of TOF spectroscopy. A detector placed some distance, d , from a neutron source measures the time taken for a neutron to fly from point A to point B. Application of simple kinematic formula reveal the energy of the neutron. At the neutron energies encountered from fission reactions and as a result of (α, n) reactions, the effect of relativity can be acceptably ignored.

One of the chief difficulties of using the neutron time of flight as a basis for spectroscopy is the acquisition of a start signal; until recently this aspect of making these measurements has limited its use. The detection of the neutron at the end of its journey is relatively simple and has been measured with a variety of detectors (primarily scintillators due to their fast response and relatively high efficiency across a range of neutron energies). Gauging the moment of the beginning of the neutrons journey however is more difficult but this has been achieved by a number of methods:

- Fission fragment detection
- Pulse mode accelerator use
- Associated particle methods

Fission fragment methods use the detection of fission fragments to determine the time of fission allowing TOF measurement of the PFNS. Being heavy charged ions, fission fragments can produce a strong signal within a detector but are also stopped very quickly by matter and will not escape from a physically-thick source. To combat this, the source nuclide is deposited thinly onto a foil and located within the detector itself, usually an ionisation chamber (as mentioned previously in section 2.3.5.1). This provides a prominent signal associated with the fission event, with a high degree of

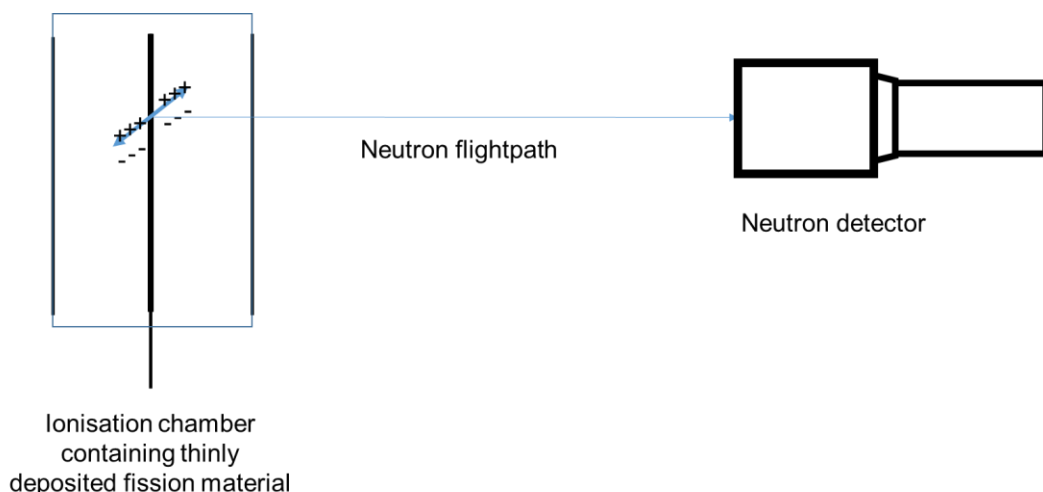


Figure 24: Illustration of ionisation chamber triggered TOF spectroscopy. Fission fragments detected in the ionisation chamber (left) trigger the start of the timing process. The detection of a prompt fission neutron in the second detector (illustrated here as a scintillator) stops the timing process.

efficiency (up to 99%). [15] By only triggering on the detection of both fission fragments, background counts can be greatly reduced.

A similar approach places the source within a ^4He gaseous scintillator rather than an ionisation chamber, although this has been reported in the context of detector characterisation as opposed to direct spectroscopy. [12]

Accelerator-triggered measurements can be used to measure the neutron energy spectrum of any prompt neutron radiation produced in induced reactions, such as induced fission or neutrons produced through bombardment reactions on targets. An accelerator-based neutron source which can operate in pulsed mode irradiates a sample of the reaction material, producing both the reaction and the start signal of the TOF measurement.

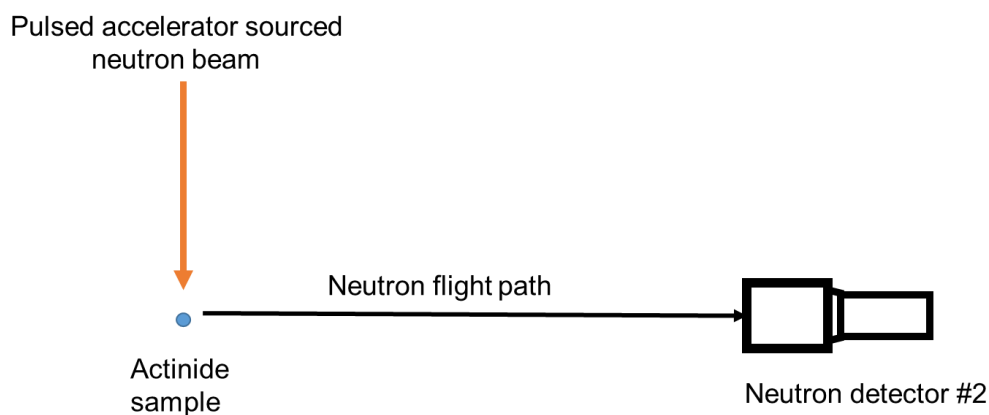


Figure 25: Accelerator triggered time of flight spectroscopy, in this case measuring the induced fission neutron spectrum of an actinide sample. The start time of the time of flight measurement is provided by the accelerator which also produces the stream of neutrons inducing the reaction.

Associated particle TOF measurements use paired detections of various particles produced either at the same time or very closely to a neutron. For fission reactions, this can mean either co-produced neutrons, or prompt gamma rays. (α, n) sources can also be measured using this technique via the detection of gamma rays produced during the reaction. For this method to work, there must be some means of correlating the two events. This can be done using a coincidence gate; neutrons detected within a certain time window after a gamma ray, for example, can be assumed to be correlated.

The time of the detection of the gamma ray is taken as the moment of fission, whilst the delay between the two events is taken to be the time of flight of the neutron. Additionally a single neutron can be used as both the trigger pulse and the particle being measured. A neutron scattered in the first detector can produce a pulse, triggering the ToF measurement. When the neutron is detected in the second detector the timing is completed, it will however have lost energy in the scatter event which must be accounted for.

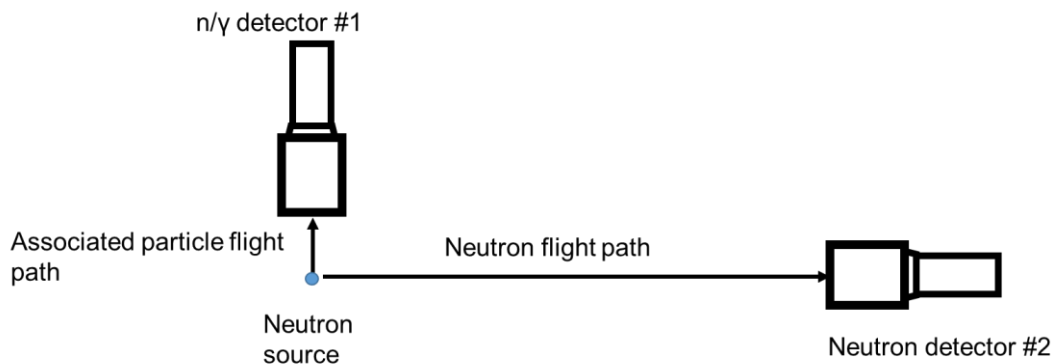


Figure 26: Associated particle TOF spectroscopy. Co-produced particles can be detected in the two detectors, and the time interval between the two detections can be used to infer the TOF. For example, a fission event can produce prompt gamma rays and neutrons. The travel time of a gamma ray to detector #1 is negligible, and so the time taken to detect a correlated neutron in #2 can be treated as its time of flight. Some method must be used to determine correlation, such as looking for events within a certain coincidence time window.

The time-of-flight method of neutron spectroscopy has a relatively long history. Due to the tendency of the alternative methods of neutron spectroscopy described above to provide a stochastic measure of the neutron spectrum, time of flight has been used as an alternative providing a deterministic measure of the neutron energy. The deterministic nature of the results has meant that it has been frequently used to evaluate neutron spectra for reference values and nuclear data purposes.

The Mannhart evaluation [15] is still a benchmark treatment of the important ^{252}Cf fission spectrum used as a standard in nuclear measurements. It is based on an evaluation of different experimental measurements of the ^{252}Cf spontaneous fission neutron spectrum available at the time. All of the experimental data in that evaluation were produced by ionisation chamber

triggered TOF setups, using a variety of neutron detectors including lithium glass scintillators, plastic scintillators and organic liquid scintillators. All of the measurements used in the Mannhart evaluation were taken in 1983 (or closely prior to 1983), but the technique predates this. Ionisation chamber TOF methods are still used to generate nuclear data as they are a well understood means of obtaining neutron spectra.

Accelerator-initiated TOF measurements are commonly used to characterise accelerator-based neutron sources. [111] [112] This method is also particularly useful for measuring the PFNS in induced fission reactions such as the $^{235}\text{U}(n,\text{fission})$ reaction and $^{237}\text{Np}(n,\text{fission})$ and is used to produce nuclear data for modelling and reference purposes. [113] [114] An additional advantage of this technique, as opposed to inducing the reaction via a radionuclide neutron source, is that the energy of the inducing neutron can be finely controlled. This allows the dependence of the spectrum on the energy of the incoming neutron to also be investigated.

A common theme across the previous two techniques is that they have primarily been used in laboratory-based settings. They are excellent techniques for producing nuclear data and reference spectra, but less well suited to general use source identification or characterisation. The requirement of accelerators or the preparation of the source within an ionisation chamber makes them impractical for more general source characterisation use. Associated particle triggered time-of-flight methods do not have the same requirements and can be performed with two detectors and the necessary electronics.

The data processing aspect of the measurements have been the limiting factor in exploiting this technique. Whilst this type of measurement has been performed in the past, the advent of digital electronics has enabled the use of associated particle triggering more widely. However, the vast majority of recent work on the subject has been focused detector characterisation rather than using it for direct spectroscopy [53]. The primary motivation is cost and convenience, as it allows a detector to be fully

characterised using a single radionuclide source rather than requiring repeated and expensive measurements using accelerators.

Some spectroscopy has been performed using the technique, however. A particular theme appears to be the measurement of the neutron spectrum produced by $^{241}\text{AmBe}$ (α, n) neutron sources [115] [116], potentially because they are less well suited to ionisation chamber measurements as they do not produce fission fragments. A characteristic, 4.44MeV gamma ray is produced by the $^9\text{Be}(\alpha, n)^{12}\text{C}^*$ reaction which can serve as a trigger for TOF measurements and can be detected outside the source volume. Additionally, the neutron spectrum of fusion experiments has been measured using neutron scatter TOF in high flux environments. [117]

The often-measured ^{252}Cf reference spectrum has also been measured using γ -tagging TOF methods, Becchetti et al. [118] and Blain et al. [119] both report the use of associated particle TOF spectroscopy in research contexts, in the first case however this is deployed as a laboratory demonstration tool, and in the second case the technique is pressed into service with the intention of gathering nuclear data. Both cases use specialised electronics and in the second case, dedicated gamma detectors to increase gamma sensitivity and n/ γ discrimination.

The present state-of-the-art in associated particle time-of-flight spectroscopy still leaves unexplored areas. The potential to provide deterministic neutron energy measurements in a wider range of applications and with portable equipment is worth exploring, especially if the ability to discriminate between very similar spectra, such as those of fission nuclides of relevance to security applications, can be achieved. This research has attempted to examine some of these possibilities as the use of digital electronic data processing methods has become widespread. In particular, the aim is to demonstrate TOF spectroscopy capabilities using general-purpose FPGA hardware and EJ-309 liquid scintillators.

A further aim of this research is to investigate the ability of such a set-up to discriminate between sources. Of particular interest are fission nuclides;

knowledge of the nuclide producing a neutron field can offer valuable insight into the origin of that particular radioactive source.

3 EXPERIMENTAL METHODS AND APPARATUS

The following chapter outlines the experimental methods deployed during the course of this work. Firstly, an overview of the EJ-309 detectors and Hybrid digitiser system used in all measurement campaigns is given. Afterwards, a description of the set-up of the system for taking Time of Flight (TOF) measurements and converting these to energy spectra is given. Finally, the calibration of the detectors with mono-energetic neutron irradiations at the sparsely explored low end of the neutron energy range is described.

3.1 APPARATUS AND EXPERIMENTAL TECHNIQUES

As discussed previously, in this research a liquid organic scintillator detector has been used to investigate various neutron spectra based on TOF. The scintillator is not a standalone device and is used in conjunction with ancillary electronics and a data-logging PC. In this research, a single-unit Mixed Field Analyser from Hybrid Instruments has been used to process the signals from the scintillators. A PC is used to log the data. Figure 27 shows a schematic diagram of the detector set-up.

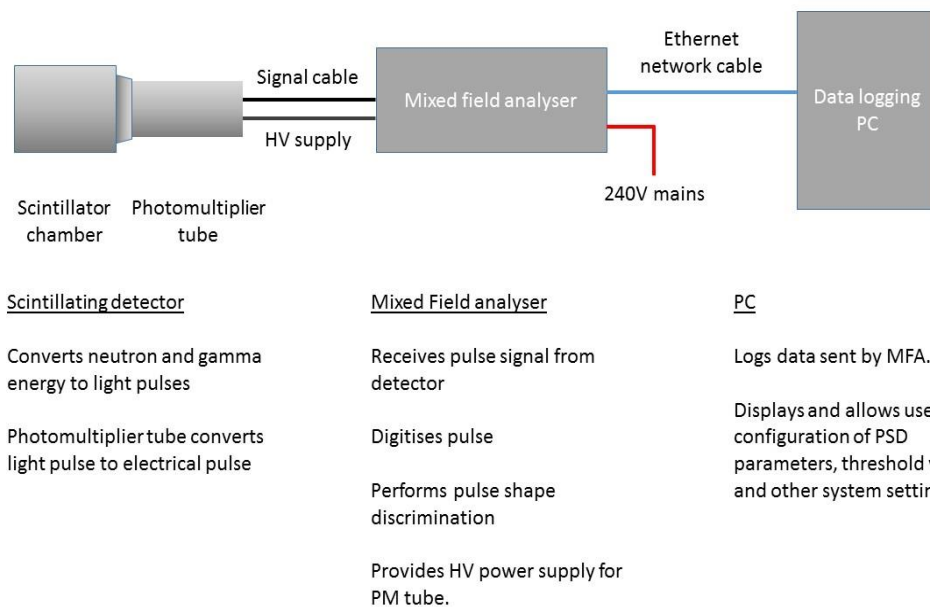


Figure 27: Schematic diagram of a single detector system using the Hybrid Instruments mixed field analyser.

3.1.1 The detector

The scintillators used in this research consist of a container of EJ-309 scintillant coupled to a photomultiplier tube. The mechanics of the scintillation mechanism and the detector response has been discussed in section 2.3.1 and will not be elaborated on further here.

The photomultiplier tube has been an essential component of the scintillator detector for many years. Indeed, until its introduction, scintillation experiments utilised the sensitivity of the human eye in a dark room, and good eyesight and stamina were preconditions to study these branches of science. The use of a device to detect scintillations with a high level of sensitivity allows for electronic data acquisition, and the ability to quantify the magnitude and pulse shape of very fast scintillations opens the possibility of spectroscopic and particle discrimination techniques.

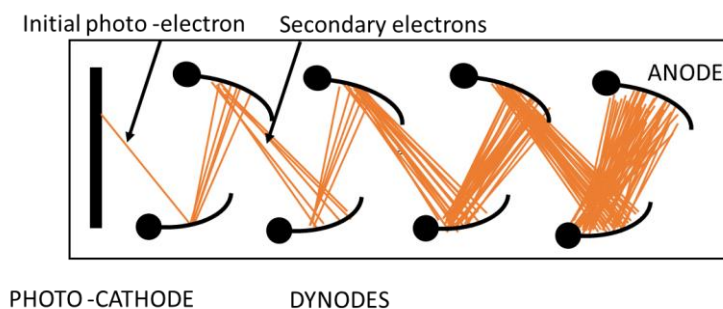


Figure 28: Schematic of a photomultiplier tube. An incident photon liberates a photo-electron from the photocathode on the left. The electron is accelerated through a potential difference to the first dynode, where it liberates further electrons via secondary emission. By using stepped dynodes, large gains can be achieved.

The photomultiplier tube is an evacuated tube containing a cathode, several dynodes and an anode. [120] The device is fed by a negative, high-voltage supply holding the cathode at a very low potential, and the dynodes at gradually increasing in potential toward ground in a stepwise manner. Light photons are guided from the scintillator volume along a light guide, made of optical acrylic or glass. At one end of the tube they encounter the photocathode where the photo-electric effect is exploited to convert them into electrons. The photocathode is designed to have a high quantum efficiency in

the blue to near ultraviolet section of the electromagnetic spectrum which is where most scintillators emit their light. An electron freed at the photocathode is then accelerated across an electric potential to the first dynode where it liberates several additional electrons via the secondary emission process. This process is repeated at each dynode resulting in considerable gain across the whole tube. Typical gains for photomultiplier tubes are between 10^3 and 10^7 depending on the number of dynodes and the operating voltage.

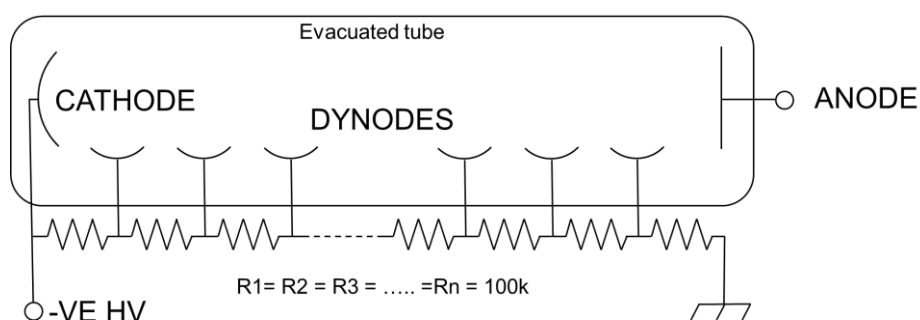


Figure 29: Circuit diagram of a photomultiplier tube showing the arrangement of the resistor network, anode, cathode and dynodes.

Figure 29 shows a circuit diagram for a standard photomultiplier tube. On the left is the photocathode as described above. Several dynode stages are then seen separating the negative high voltage from ground. The resistor network provides a potential divider giving a gradual decrease in voltage in several discrete steps. The resistors are specified to limit the current that will flow with each pulse: too low a current will affect sensitivity, but linearity is lost as current rises above a threshold value. Resistors of around $100\text{ k}\Omega$ are typically used in the potential divider.

The detectors have a signal output on the photomultiplier tube anode connection, using a BNC connector to allow a length of RG-58 co-axial cable to carry the detection pulse to the mixed field analyser. The use of co-axial cable gives good HV signal transmission for fast pulses, particularly important in the case of scintillators with typical pulse rise times of nanoseconds. The detectors are supplied with a high-voltage supply fed via another co-axial cable, connected via a SHV connector to prevent incorrect coupling.

Operating voltages of photomultiplier tubes can vary depending on their design and purpose. [121] Generally speaking, photomultipliers are run at between -500 V and -2000 V. Photomultiplier gain varies logarithmically with the operating voltage and insufficient voltage will affect sensitivity. Overly high magnitude pulses can exceed the range of pulse processing hardware or be outside the range in which the hardware behaves in a linear fashion.

3.1.1.1 The detector used in this research

This research has used two EJ-309 detectors, both produced by Scionix, Holland, of type V94A94. The detector consists of a square scintillator chamber coupled to a photomultiplier tube with an integrated resistor network.



Figure 30: Photograph of the Scionix V94A94, EJ-309 liquid organic scintillator used in this research.

The scintillator chamber is 100 mm × 100 mm × 100 mm in dimension, with an aluminium casing and light guide to ensure optical coupling to the photomultiplier tube. Connection to the negative high voltage supply and data logging electronics are provided by BNC sockets on the top of the detector. The scintillator is pictured in Figure 30.

3.1.2 The mixed field analyser

The mixed field analyser (MFA) is a field programmable gate array (FPGA) based signal acquisition and processing system manufactured by Hybrid Instruments Ltd. It comes in single channel or 4-channel versions, the latter allowing it to operate 4 detectors independently but on a single processing board and clock for timing purposes. Figure 31 shows the MFA and some of its specifications.

Hybrid instruments Mixed Field analyser

- 500 MSa/s sampling rate
- 12-bit resolution
- 3 Mpps discriminated particle throughput
- Integrated HV supply up to 2 kV
- Time correlated TTL neutron and gamma outputs
- Network based PC connectivity



Figure 31: Hybrid Instruments Ltd Mixed Field Analyser

Central to the operation of the MFA is an FPGA signal acquisition board. FPGA hardware provides ultra-quick processing of the detector signals, allowing real time pulse processing and throughput. Pulses from the detector are digitised by the MFA which then offers several processing options. As its name suggests, it is primarily a device for working in mixed neutron/gamma-ray fields: neutron and gamma events are separated using a pulse-shape discrimination algorithm described below. Following discrimination, events are output either in the form of TTL signals on the front of the unit, allowing it to be used with a pulse-counting device, or via TCP/UDP network packets over a network card to a connected PC. In PC-mode, the pulse height or the time of flight between two events can be logged in an event list mode. The PC is also used to set the pulse shape discrimination parameters, trigger settings and thresholds using a graphical user interface on the PC.

In time-of-flight mode, a coincidence window can be set between two detector channels on a 4-channel MFA. When two events are detected within this time window, both are assumed to be scatter events between the detectors. More information on TOF mode is given below.

The MFA also has an integrated high-voltage supply, providing independent supplies to each connected detector. This allows different models of detector to be used or independent calibration of similar detectors to be performed.

3.1.3 Pulse triggering and digitisation

Pulse digitisation is performed via a 12-bit bipolar analogue to digital converter (ADC) feeding into the FPGA. Prior to digitisation, the signal is passed through a variable gain amplifier. The ADC provides a total of 2048 separate values across the positive voltage range and appropriate variable gain amplifier settings are chosen to enable the use of the full range of the ADC without producing signal clipping due to over-amplification of the largest pulses.

The MFA offers a choice of two triggers used to recognise pulses: a differential and a greater-than trigger. When set to greater-than, the MFA will trigger as the signal rises above a user-defined threshold. The differential trigger operates by comparing adjacent samples; a trigger is initiated when a samples value increase is greater than the user-specified value and a pulse is registered. The trigger level is set in arbitrary ADC units as the effect of the variable gain amplifier precludes relating the trigger level setting to a specific voltage range. Figure 32 shows the two trigger schemes.

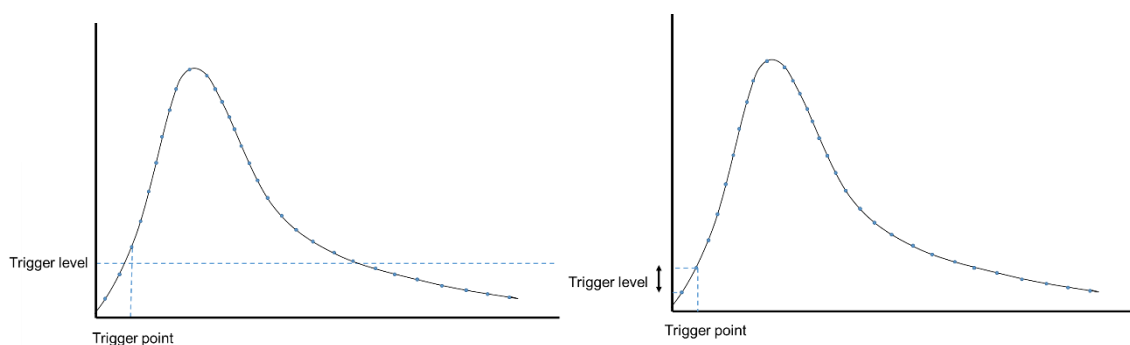


Figure 32: Trigger options available on the Hybrid systems MFA. On the left the greater than threshold, where the first datapoint above a threshold triggers pulse processing. On the right, Differential triggering, where a difference of a certain value between points triggers pulse processing.

3.1.4 Pulse-shape discrimination

Discrimination between neutron and gamma-ray events is performed by the FPGA onboard the MFA in real time as pulses are detected and digitised. Differentiation between particle detections is achieved by measuring the difference in pulse shape produced by each particle. As described in section

2.3.2.2, Pulse shape n/γ discrimination, there is a subtle difference in neutron and gamma-ray pulses, with both rising quickly to their full pulse height, and then dropping off with pulses produced by neutrons decaying more slowly than pulses produced by gamma-ray events.

The beginning of the pulse is detected using one of the two methods described above as chosen by the user. Once the MFA has been triggered at the start of a pulse, a set time window is taken to contain the pulse, and the digitised pulse is passed to the PSD algorithm.

The MFA distinguishes between the events using a two-point discrimination algorithm. Firstly, the pulse is smoothed using a moving average filter to reduce measurement noise. Following this two amplitude samples are taken, one a short amount of time after the pulse peak, and the second a user specified number of nanoseconds afterwards. The comparison of these two points allows neutron events to be distinguished from gamma events in 56ns, faster than the timescale of the pulse. Figure 33 shows the pulse shape and the timings of the various PSD parameters.

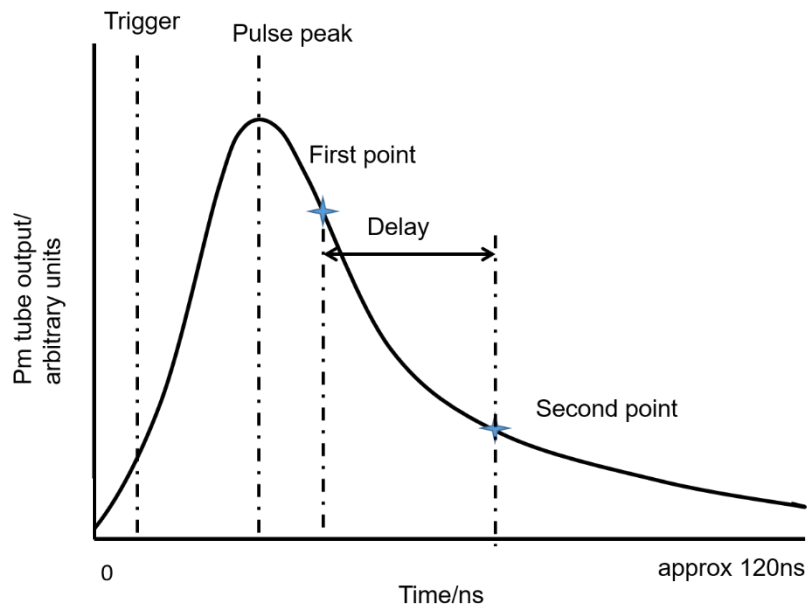


Figure 33: Illustration of the PSD process. The pulse is smoothed using a rolling average filter, once the peak is detected, two parameters are sampled, one near the peak, and one a set amount of time (typically 16ns) later. The difference between these two samples are used to identify the particle that produced the event.

When connected to a PC, the MFA can transfer the two pulse shape parameters over the network interface to the software running on the PC. This will plot the two values on a scatter plot, where the user can then specify PSD parameters as shown in Figure 34. In this research, the PSD capabilities of the MFA have been used to filter coincidence events in terms of the combination of particles they consist of. As this process requires either real-time knowledge of particle identity, or the storage and post processing of list mode pulse data, the real time PSD capability of the digitiser is valuable.

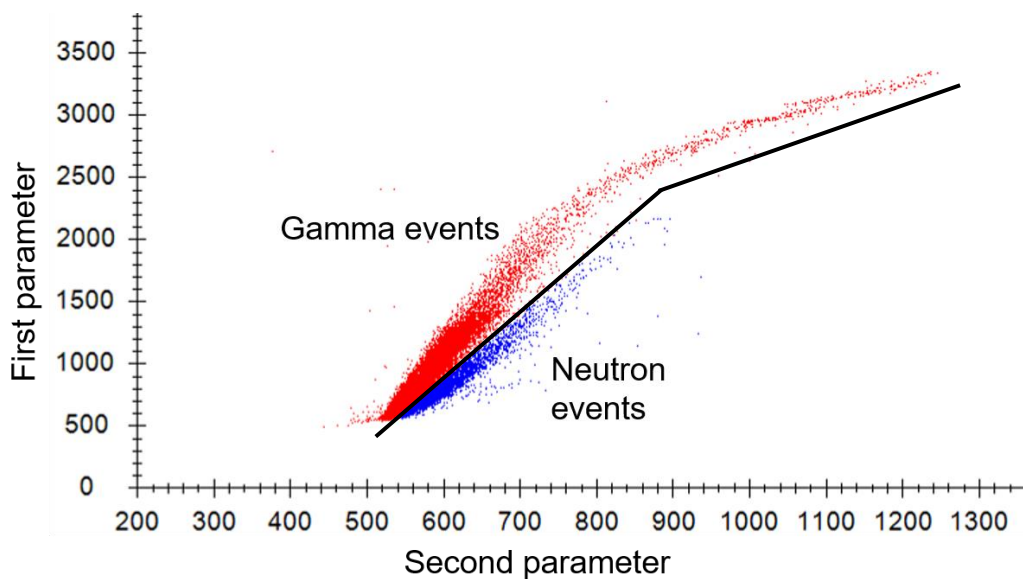


Figure 34: PSD scatter plot showing neutron and gamma "plumes" produced by the PSD parameters taken by the MFA. PSD allows the neutron component to be extracted in the presence of a strong, undesired gamma field. Events are sorted depending on the side of the black line they fall, which is set by the user by placing the three points during the instrument set-up. Data collected from a ^{252}Cf neutron source for illustrative purposes

3.1.5 Pulse height spectra

Producing histograms of pulse heights detected by the MFA is very useful for spectroscopy and troubleshooting purposes. The MFA can display a pulse height spectrum in real time directly on the GUI, or the long integral values can be taken from the log file in post processing. In this research, the python® programming language has been used to produce scripts that post process the log files, extracting the long integrals and binning them by size to produce a pulse height spectrum. Python® post processing of long and short integrals has also been used to judge the operation of the PSD process.

3.1.6 Coincidence mode

In response to a specific requirement for this research, the MFA firmware was modified by Hybrid Instruments Ltd. to operate in a bespoke coincidence mode. This function provides time measurement between pulses in separate detectors for spectroscopy purposes. Processing the signals from both detectors in the same unit and using the same clock cycle for processing allows for timing of pulses between channels. The FPGA gives a timing resolution of 4 ns, limited by the clock cycle of the unit.

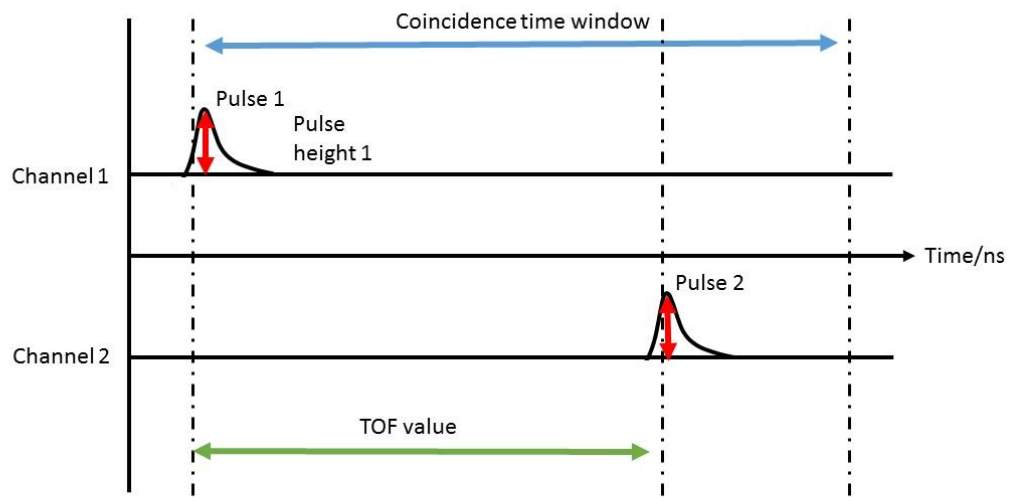


Figure 35: Schematic illustration of coincidence mode. Every pulse detected opens a coincidence window (time set by the user, up to 240 ns). An event second detector within the time window is registered as coincident and the time between the two events, as well as the particle identity is recorded.

The coincidence mode gives the option to set a variable length time window. Whenever a pulse is detected in one channel, the window is initiated and if a pulse is detected in the other channel during this time period, a coincidence event is logged. Figure 35 shows the timing schedule for time of flight mode. Along with fast timing the MFA retains its real time particle discrimination function, allowing particle-based logic to be applied to coincident events, only

processing those for example which involve two neutrons, or a gamma-ray and a neutron. This function firstly acts as a filter to reduce the data-processing requirement both during operation and post-measurement, and also allows the contributions to the time distribution made by different mechanisms to be identified.

Upon flagging a coincident event, the MFA logs an event via the network interface, recording the pulse heights in each detector, the time of flight between the detectors, and a direction indication parameter showing the direction in which the scatter occurred.

The four detection pairings contain manifestations of three coincidence scenarios:

1. Detection of correlated particles: two prompt gamma rays, neutrons or combinations of the two are detected within the coincidence window in the two detectors. Particles detected after correlated production like this will take direct paths to the two detectors as seen in Figure 49.
2. Detection of scattering between detectors: a single neutron or gamma ray is detected in both detectors as it scatters between the two. Events of this type result from a single particle taking the path between the detectors also shown in Figure 49.
3. Accidental counts are recorded as a result of two uncorrelated particles being detected in the two detectors within the coincidence window by virtue of the Poisson statistics governing the temporal distribution of radioactive decays of the source.

Figure 36 shows an example of the time distribution of correlated events (example data taken at the Lancaster University ^{252}Cf source). This plot shows the time interval distribution (TID) recorded between two detections, provided the second event is in the second detector and is detected within the coincidence window of 240 ns. This plot contains all events independent of particle identification. The features produced by the four correlation scenarios can be clearly observed and are demarked in Figure 36.

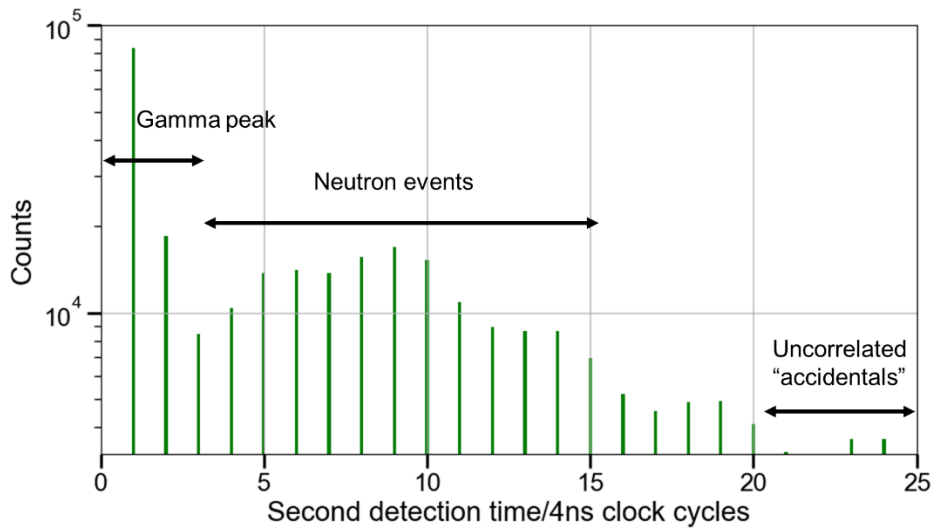


Figure 36: Time interval distribution of correlated events independent of particle type. This distribution contains a histogram of the times logged for correlated events detected within a time window of 100 ns. The Gamma peak seen on the left contains coincident gamma detections. Events involving neutrons form a “hump” produced by the range of arrival times for neutrons of different energies. Data collected for illustrative purposes from a ^{252}Cf fission source.

The first feature in the time distribution is the gamma-ray peak. Gamma rays travelling at the speed of light arrive first after the corresponding fission event from which they originated, irrespective of the detector they arrive at. This initial peak in the time separation spectrum represents double gamma-ray events, either containing a single gamma-ray photon scattered between detectors or two correlated prompt gamma-ray photons. The following “hump” spanning 3 to 20 clock cycles (12 to 80ns) contains events involving neutrons. The contents of the n-hump are listed in Table 2.

Table 2: Coincident detection mechanisms in the two detectors found in the neutron "hump".

Particle in detector 1	Particle in detector 2	Correlation mechanism	Time of Flight corresponding to presumed coincidence mechanism
n	n	Correlated neutrons from the same fission event	(TOF of neutron to D2)- (TOF of second neutron to D1)
n	n	Single neutron scattered between detectors	TOF of neutron between D1 and D2
γ	n	Prompt gamma detected in detector 1, prompt neutron detected in detector 2	(TOF of neutron to D2)- (TOF of gamma to D1)
Either	Either	Accidentally coincident events	Flat interval distribution according to Poisson statistics

Theoretically, the spectrum of Time Of Flight (TOF) values stated for the second two scenarios listed in the table are related directly to the PFNS emitted from the source. In the case of the n-n scatter events, the time of flight corresponds to the time of flight between the detectors, where the neutron will

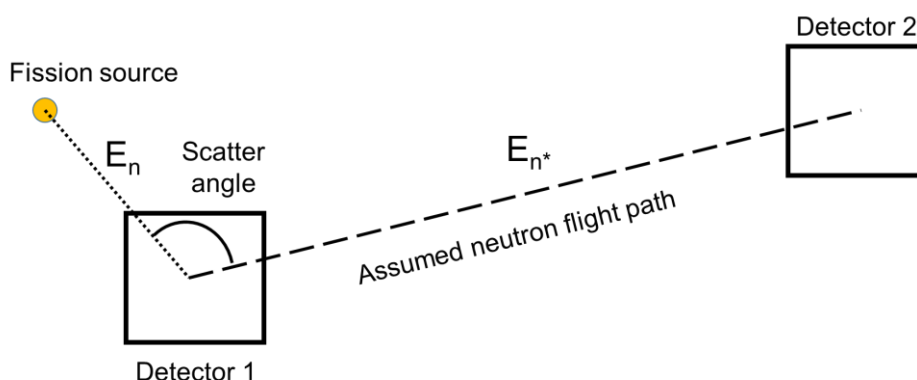


Figure 37: Schematic of a n-n scatter event. The source neutron with energy E_n scatters in the first detector, depositing some energy and producing a start signal. Timing the neutron's flight to the second detector gives a measurement of its energy after the scatter, E_{n^*}

have the energy it received from the fission event, minus the energy lost in the scatter. As all of the neutrons which undergo scatter reactions will be scattered through approximately the same angle between the detectors, and therefore the TOF spectrum is a function of the PFNS, the scatter angle between the detectors and the distance separating the detectors.

The time recorded in the case of gamma-neutron events also corresponds to PFNS. The time of flight of the gamma ray to the first detector is practically negligible compared to that of the neutron to the second detector, and so if the two are correlated then the gamma ray can be treated as an indicator of the time of the fission event itself (or a correction can be made assuming the source location is known). Correspondingly, the time delay to the neutron detection can be considered to be a measurement of the time of flight of the neutron from point of fission to second detector. The TOF from source to detector is a function of the PFNS and the detector-source separation, and so this TOF spectrum can be directly converted to the PFNS.

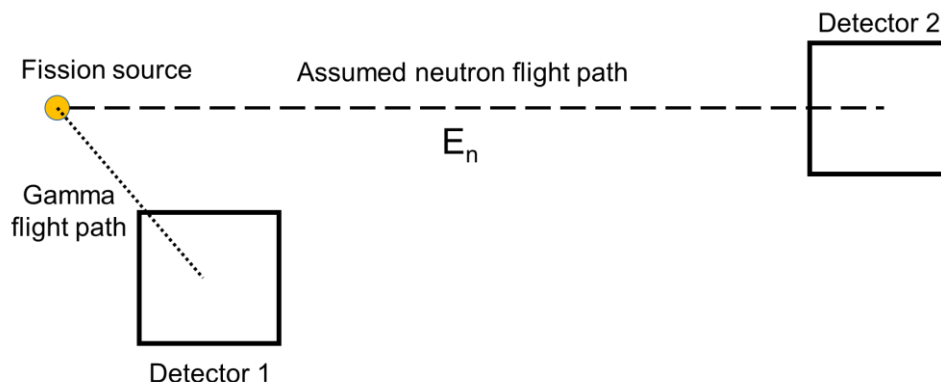


Figure 38: illustration of gamma triggered TOF measurements, the detection of a gamma event in detector 1 starts the timing process, stopped by detector 2.

3.1.6.1 Uncertainties in the TID to TOF conversion

If the source and detectors were set up in a large area of free space, with perfect detection timing, particle discrimination and infinitely small and infinitely efficient detectors were available, then the TOF measurements above could be used to determine the PFNS directly, as described above.

However, there are several factors which affect the response of the system and add a level of uncertainty to the measurements.

Firstly, there is the matter of neutron scattering; in addition to travelling directly to or between the two detectors and producing the scenarios listed in Table 2, the particles involved can travel via one or more scatters off the surroundings. Neutrons detected after a scatter will have traversed a considerably further flight distance than that inferred from the detector arrangement. In addition, the neutron will lose a portion of its energy as it scatters, travelling more slowly and adding extra time to its time of flight. The geometry involved with these scattering events is shown in Figure 39. Scattered neutrons are shown in the figure as coming directly from the fission source but scatter off a mass after scattering in the first detector is also possible.

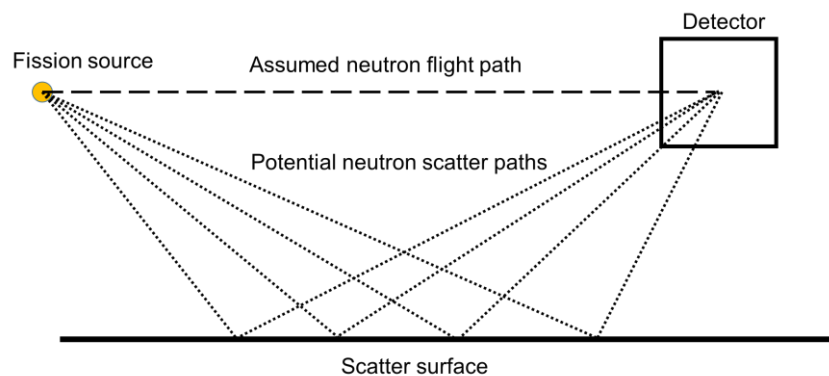


Figure 39: The effect of scatter neutrons on the perceived TOF spectrum. The dotted lines show different possible paths taken to the detector by a neutron. In all cases the detection will have been assumed to have followed the direct path shown by the dashed line.

The physical size of the detectors also adds an amount of uncertainty to the measure of the distance the neutron has travelled. Since the neutron interaction with the detector can either happen at the front of the scintillator volume, at the rear or any other point, uncertainties of up to 9 cm (in the detectors used in this study) are introduced. As a 1 MeV neutron travels approximately 1.4 cm in a nanosecond, this can mean a difference of around

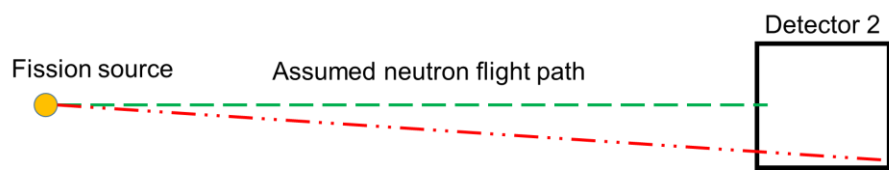
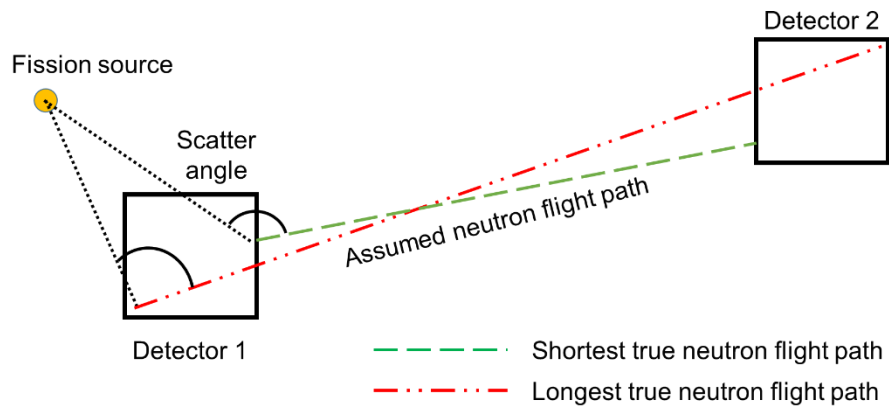


Figure 40: Uncertainty produced by detector setup in n-n scatter events (top) and γ -n events (bottom). The effect of position of scatter in the detector on flight length and scatter angle is illustrated.

6.5 ns in travel time depending on where it interacts in the detector. Figure 40 shows the potential longest and shortest flight path of neutrons in both the n-n and γ -n correlation scenarios. Geometric uncertainties will be more pronounced in the case of single particle n-n scatter detections, as there is uncertainty in the detection/scatter position in both the first and second scintillator volume. In this case, the different scatter paths will also contain a range of potential scatter angles, leading to uncertainties in how much energy the neutron will have deposited in the first detector. If the fission source is physically small, then γ -n detections only have spatial uncertainty in the second detector as the differences in TOF as a result of detection point for the gamma ray being negligibly small³.

For n-n correlated events there is a component of the detection separation spectrum added by correlated prompt neutrons. As fission events

³ A gamma ray takes 0.03 ns to travel an extra centimetre in the detector in contrast to the neutron's 0.7 ns.

produce neutrons with an average multiplicity greater than one, there is a possibility of detecting two of the prompt neutrons in two separate detectors. If the assumption is being made that all n-n designated events are a result of detection of a single neutron scattered in the first detector, then this component will contaminate the TOF spectrum garnered from the measurements. The time separation of two detected prompt neutrons cannot be directly related to the PFNS as it is a function of two neutron energies, and two detector distances from the source, rendering the problem ill-posed.

Finally, there is a certain level of background counts. Radioactive decay obeying Poisson statistics produces randomly-spaced events with a time interval distribution described by the function [122] :

Equation 9
$$I_n(t) = \frac{(\lambda t)^{N-1} e^{-\lambda t}}{(N-1)!} \lambda$$

Where $I_n(t)$ is the distribution of time intervals t between a pulse and its Nth neighbouring pulse, and λ being the average rate . Summed over all possible values of N renders:

Equation 10

$$\sum_{N=1}^{\infty} I_N(t) = \lambda$$

indicating that single, randomly produced counts will produce a flat distribution proportional to λ^2 , highly-active sources giving higher background counts. A background correction can be performed by taking the average count of the bins representing coincidences that arrive after any real correlated particles could arrive. In practice, this is where the time separation distribution flattens to a constant value of counts.

3.1.6.2 Conversion to neutron energy spectrum

The TID spectrum can be converted to the neutron energy spectrum via a number of steps. Firstly, an assumption must be made so that the detection time separation spectrum may be treated as a Time-of-Flight spectrum. To enable this, coincidences must be able to be treated as correlations.

All contributions to the time separation spectrum are correlated in some manner except accidental coincidences which must be removed. As stated above, truly random, uncorrelated events can be expected to produce a flat response in the detection time separation spectrum. This effect is seen in the example dataset shown in Figure 41. The contribution made by this random background can be inferred by observing the count in a time bin a substantial

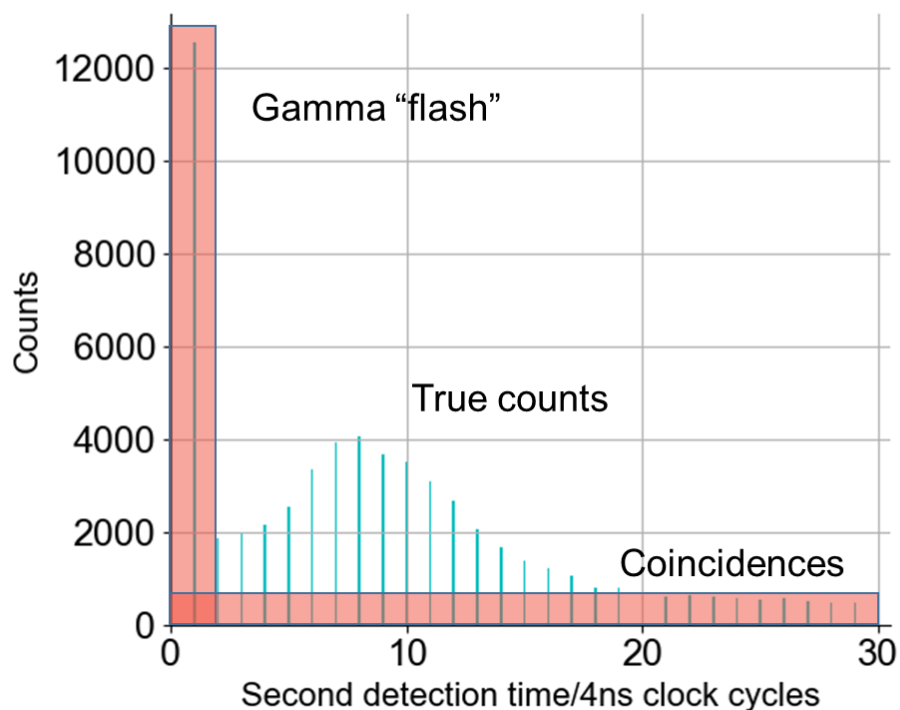


Figure 41: Time interval spectrum example data showing discarded components of the data. A constant section at the bottom of each bin can be removed representing coincident events. The gamma flash at the beginning of the distribution can also be discarded.

distance from the initial detection, after any genuinely-correlated counts can be expected to have arrived in the detector. Taking the average of several bins in a window at great time separation from the initial event accounts for statistical variation in background counts, and this value can be subtracted from all bins. Without randomly coincident events, the remaining counts in the time separation spectrum can be reasonably assumed to be correlated in some manner.

Using the correlation mechanisms described in Table 2, the researcher can begin to make sense of the physical events being measured. Using all

recorded events in one analysis is sub-optimal, as a number of different mechanisms contribute to the spectrum, and therefore a single time bin cannot be reasonably assumed to represent a single time of flight. Using the additional information provided by the particle discrimination abilities of the MFA, however, allows the different mechanisms to be separated out to a certain degree. With a reasonable level of confidence that the correlations are due to a particular coincidence mechanism, the spectrum can be treated as a TOF spectrum and then converted to an energy spectrum.

As the PSD process is not perfect, some events can be miss-identified, allowing some corruption of the TOF spectrum. Some mis-identifications can be filtered out from the TOF spectrum itself. Any gamma rays detected in the second detector will arrive in the first two clock cycles, well before any of even the fastest neutrons can arrive in the detector. This gamma-ray peak can therefore be removed, as shown in Figure 41, and the effect of mis-identifying gamma photons as neutrons in the second detector is null.

Incorrect particle discrimination in the first detector however is more problematic. If the assumption, for example, is that an n-n event is a scattered neutron, when in fact it was a prompt gamma ray that arrived in the first detector and a prompt neutron in the second detector, then the distance that it has travelled is further than anticipated, and additionally it will have been assumed to have lost energy in a scatter event that never happened. This will give an erroneous measure of the neutron's energy, although the exact magnitude of the error will depend on the initial energy of the neutron.

More simple is the case of a neutron masquerading as a gamma ray in the first detector. In this case, the assumption is that the event in the first detector corresponds to the time of the fission event producing the neutron detected in the second scintillator. In actual fact, the TOF value measured will be the genuine TOF of a neutron to the second detector, minus the non-negligible time of flight of the first neutron to the first detector. This will therefore produce a value indicative of a faster neutron than was actually present.

Once the TOF spectrum has been obtained, it can be converted to neutron energy using the standard formula expressing kinetic energy in terms of distance and time:

Equation 11

$$E_n = \frac{1}{2} m_n \left(\frac{d}{t} \right)^2$$

where E_n is the neutron energy, m_n is the mass of the neutron, d is the distance the neutron has travelled and t is the TOF.

If n-n coincidences are being used to generate the PFNS spectrum then an additional correction must be made for the neutron scatter. This correction can be performed using Equation 5, the formula for neutron energy after a scatter event discussed in the section on Neutron scattering on page 14, reproduced here:

$$E_{n2} = \frac{4A}{(1+A)^2} (\cos^2 \theta) E_{n1}$$

(with E_{n1} and E_{n2} being neutron incident and resultant energy, respectively, A is the atomic mass of the recoil nucleus and θ is the neutron scatter angle.) As can be seen, the energy possessed by the neutron after its scatter depends on the initial neutron energy, the angle through which it is scattered by, and the mass of the nucleus off which it scatters. Scatter angle can be measured from the angle between detector 2 and the centroid of the source and detector one. This angle is subject to uncertainty associated with the non-negligible dimensions of the detectors. The mass of the scatter nucleus cannot be known without prior knowledge of the initial conditions. An assumption can be made that the predominant scatter nucleus is hydrogen ($A=1$), although the spectrum will be contaminated with events which have scattered off other nuclei in the scintillator, primarily carbon ($A=12$).

Further to converting the TOF bins in the above plots, a correction for bin width must also be applied. Neutron energy is inversely-proportional to the square of the TOF, and so the bin widths, although a constant width of 4 ns (1 clock cycle) in the time domain, are wider in the energy domain at shorter

times of flight. To make the energy bins comparable with each other, the counts are corrected by dividing through by the bin width to give units of dN/dE .

A final correction must be made for the effects of relativity. The effect on the spectrum at fission neutron energies is small ($\approx 3\%$) but can be accounted for by replacing the rest mass of the neutron with its relativistic mass according to its velocity using the following relationship:

Equation 12

$$m_{relativistic} = \frac{m_{rest}}{\sqrt{1 - \frac{v^2}{c^2}}}$$

Where $m_{relativistic}$ is the relativistic neutron mass, m_{rest} is the neutron rest mass, v is the neutron velocity and c is the speed of light.

3.2 NEUTRON SOURCES

Several different neutron sources at separate facilities were used for measurements in this study. The first was Lancaster university, where a water-stored ^{252}Cf source was used for initial research with the TOF system and an investigation into the effect of several variables on the TOF spectrum. An experimental campaign at the National Physical Laboratory, Teddington, UK, involved the use of accelerator-based mono-energetic neutrons along with the use of a bare ^{252}Cf source.

^{244}Cm measurements were taken at Pajarito Scientific Corporation, in Santa Fe, New Mexico, also available there was a ^{252}Cf source for comparison.

3.2.1 The Lancaster ^{252}Cf source

The Lancaster University californium neutron source is a water-stored ^{252}Cf neutron source. It is housed in a 1 m^3 water tank providing containment of the neutron field when not in use. Gamma shielding is provided by 20 mm of steel cladding on the outside of the tank. The source is a small, doubly-encapsulated ^{252}Cf fission source mounted on a pneumatic handling mechanism. For day-to-day storage, the source is kept in the centre of the

tank, and when the source is required a compressed air mechanism moves the source from the middle to the edge of the tank, allowing neutrons to escape out of the side. When in the exposed position the source still has a thin layer of 2.5 cm of water between it and the side of the tank. The source was used in this research to perform initial validation measurements to test the ability of the MFA running two detectors in coincidence mode for the first time.

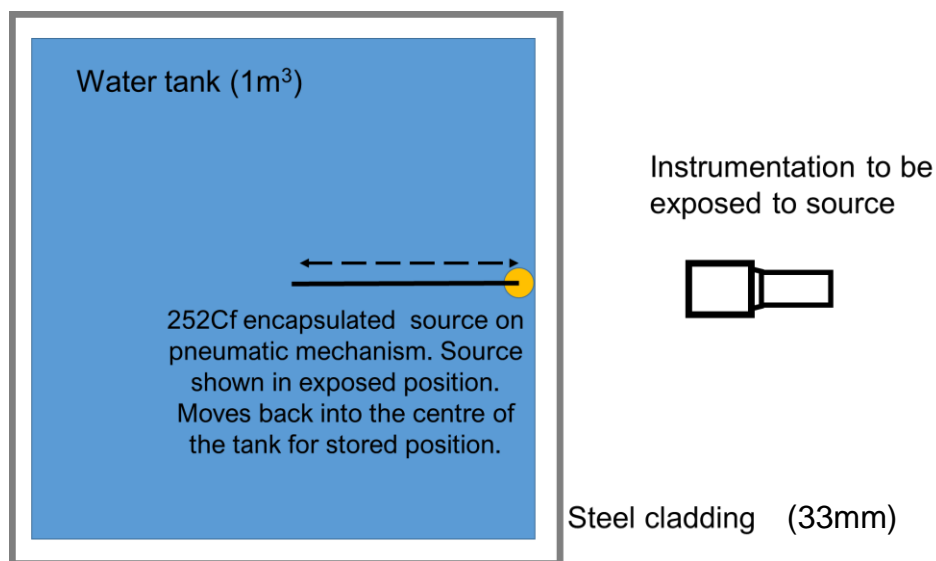


Figure 42: Plan view of the neutron source facility at Lancaster university. In the figure the source is shown in the exposed position in which neutrons can escape from the side. In the stored position the source is moved to the centre of the tank. (not to scale)

3.2.2 Bare sealed sources

In addition to the water-stored ^{252}Cf source, a number of sealed neutron sources have been used in measurements. Sealed sources contain an amount of active material produced in a reactor. The source is typically doubly-sealed inside stainless steel capsules, welded closed to provide



Figure 43: A variety of sealed sources used for various detector calibration and other measurement tasks. Photograph taken by the author at Bradbury Science Museum, Los Alamos, NM.

protection against leaks. Neutrons are produced either via spontaneous fission or secondary reactions produced by the radiation of the primary radioactive nuclide, for example (α, n) reactions. Sealed sources come in a range of sizes, measured in either decay rate (usually in Becquerels but also Curies) or neutron production rate (ns^{-1}). Neutron rate is more common with (α, n) sources as the neutron production rate depends on many factors arising in the manufacture of the source. For spontaneous fission sources the neutron production rate will depend on the source activity, the branching ratio of the decay chain of the active nuclide, and the spontaneous fission neutron multiplicity of the isotope. The half-life of the active isotope must also be considered when calculating source strength. ^{252}Cf for example has a half-life of 2.645 years; sources are frequently deemed usable for several half-lives and so the actual amount of active material will potentially have diminished since the source was commissioned.

protection against leaks. Neutrons are produced either via spontaneous fission or secondary reactions produced by the radiation of the primary radioactive nuclide, for example (α, n) reactions.

Sealed sources come in a range of sizes, measured in either decay rate (usually in Becquerels but also Curies) or neutron production rate (ns^{-1}). Neutron rate is more common with (α, n) sources as the neutron production rate depends on many



Figure 44: ^{244}Cm source used at PSC. The active material is contained on a foil disk at one end of the source assembly. Ruler markings in inches.

Sealed sources are convenient to use as the material is completely sealed away from the outside world. They are particularly useful in the TOF measuring context as they are physically small, giving a precise location from which, the neutrons originate, and have little in the way of moderating material to significantly affect the neutron energy spectrum. Figure 44 shows the source assembly used in the curium measurements at Pajarito Scientific Corporation (PSC), the active material is contained in a circular foil disk 22 mm in diameter at one end of the source (top end in image.) The additional bulk of the source assembly distances the hand from the source foil to minimise the dose received. In practice, the source is carried by the string visible in the bottom of the image in order to minimise the received dose further.

The two other sources used in this research were both sealed ^{252}Cf spontaneous fission sources. A small californium source was used at PSC to compare with the curium measurements. A sealed californium source was also used at NPL to compare a bare source with the Lancaster water-stored source.

3.2.3 The NPL Van de Graaf accelerator

Whilst radionuclide sources are useful in many applications, their continuous neutron spectrum can limit their use in calibration applications. In order to determine the absolute detector efficiency at low energies, a detector characterisation was performed at the low-scatter facility at the National Physical Laboratory in Teddington, London (NPL). The low-scatter facility consists of a Van de Graaf generator housed alongside a large accelerator hall. The accelerator hall contains a large pit with a tower in the centre which gives a mounting point for the detector, providing a large spatial separation between the detector and the hall structure. This allows measurements to be taken with a minimal scattered neutron component. When used in conjunction with a mono-energetic neutron source, the detector response to an accurately known neutron spectrum and fluence rate can be measured.

The mono energetic neutron source is produced by the Van de Graaf generator. By accelerating protons or deuterons toward a suitable target, (p,n)

and (d,n) reactions can be used to obtain neutrons. As the potential difference is finely controllable, the energy transferred to the ions introduced into this cylinder is also finely tuneable. [123] Acceleration is achieved using a high potential difference generated on a steel shell by an electrically charged belt.

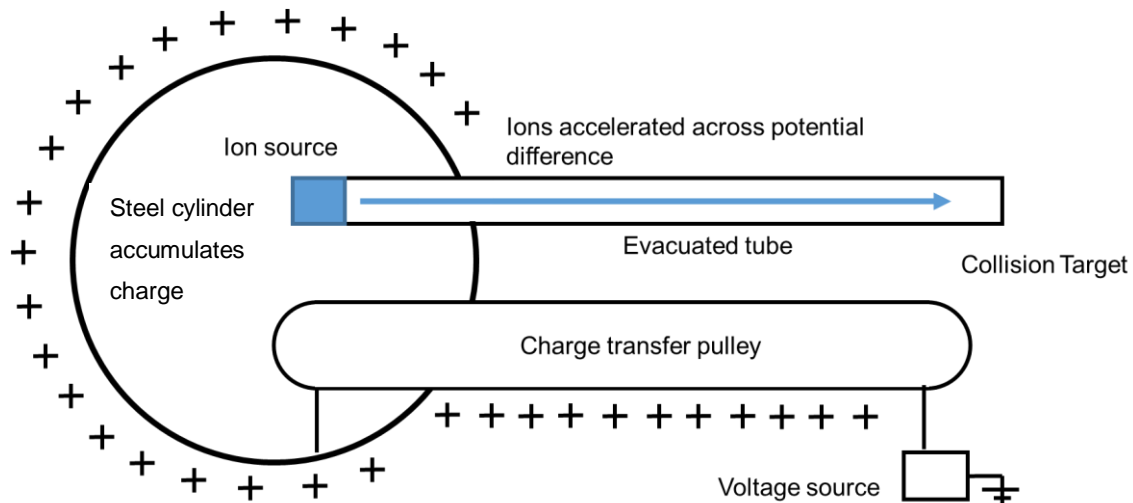


Figure 45: Schematic of a Van de Graaff accelerator. Positive charge is transferred to a steel cylinder from a charged belt via the skin effect. This positive charge produces a potential difference used to accelerate ions to a finely tuneable energy.

The energy provided to the neutron during the reaction depends on that of the incident proton. This gives the Van de Graaf generator its ability to provide an essentially mono-energetic source of neutrons. As the target is physically thin, the protons will only lose a very small amount of energy traversing the target, meaning the reaction kinematics are essentially the same for each produced neutron, leading to a mono-energetic neutron spectrum. There is a small deviation from a purely mono-energetic neutron energy spectrum caused by neutron scatter within the target; this contribution is calculated via Monte Carlo calculations for the specific neutron energy and target material and is folded into the uncertainties.

The energy of neutrons produced in this way is not isotropic and varies with the angle from the reaction target and the magnitude of this variance is dependent on the neutron energy. The low-scatter facility has the equipment to mount the subject of an irradiation at any angle around the pit and provide several irradiations at different energies at once, in these measurements however the 0° position was used exclusively. Figure 46 shows the layout of the low-scatter facility and the position of the mounted detector.

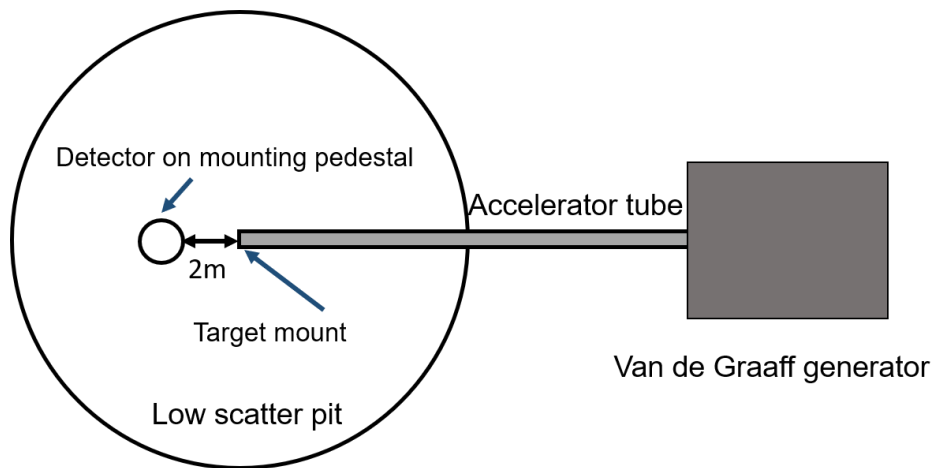


Figure 46: Plan view of the layout of the low scatter facility at NPL. The detector is mounted on a pedestal near the centre of the pit, approximately 2m away from the reaction target of the Van de Graaf generator.(not to scale)

To perform calibrated runs, the neutron fluence rate is determined using the NPL standard long counter prior to the irradiation of the instrument. This process ensures the fluence rate at the particular neutron energy provided to the detector to be calibrated is accurately known. The long counter consists of a BF_3 proportional counter tube surrounded by a cylinder of moderating wax, open at one end. This gives a directional, neutron detector, insensitive to gamma rays and with a reasonably flat response across a wide range of neutron energies [124]. The response of the long counter is well characterised through the use of well-defined radionuclide sources and Monte Carlo calculations.

As the long counter and scintillator cannot be run in the same position and at the same time, an additional measurement during both the calibration run and the detector irradiation must be made. To provide this information a

current integrator measures, the proton current impinging on the reaction target and a slab counter on the laboratory wall measures the neutron field produced during each measurement. Counting software measures these two parameters so that the total integrated fluence provided during the detector irradiation may be determined.

3.2.4 Scatter cone measurements

As discussed in section 2.2.1.1, neutrons scatter off matter in the environment and so neutrons that would not have hit the scintillator can potentially scatter back into the detector from the surroundings and register a signal. This scatter component of the neutron field will be indistinguishable from neutrons direct from the source. This presents several potential issues for the neutron metrologist. Complications arising from scatter neutrons include:

1. Distortion of the measured pulse height spectrum. Neutrons will have lost energy as they scatter, this will affect the PHS measured from a particular source and interfere with spectroscopy measurements using the energy deposited in the scintillator.
2. Scatter neutrons will take longer to reach the detector, corrupting time of flight measurements.
3. Greater numbers of neutrons will be detected than would have been otherwise. If the counts made in a detector are being used to infer the absolute decay rate of a source, or calculate detector efficiency, then the extra counts from scattered neutrons will add erroneous counts.
4. Scatter neutrons can mask the location of a source. If directionally sensitive detector systems are being used, then scatter neutrons may appear as if they are arriving from another location.

The number of scatter counts made by a detector is dependent on the particular surroundings at time of measurement. Any matter in the proximity of the detector can scatter neutrons back to be counted and form a potentially large scatter component of the measurement. Scatter can be off solid, dense objects in the vicinity of the source or detector, or it can be from the air around the detector, producing air in-scatter.

In many cases the best way to combat the incursion of scatter neutrons on the measurement is to minimise their existence in the first place. Siting the detector and source as far away from unnecessary objects can reduce the total number of scatter neutrons. The low-scatter facility at NPL used for some of the measurements in this research uses a large room (7 m separation from the closest wall) and places the detector on a tower in a pit (6 m deep) to reduce the scatter contribution to measurements. A similar strategy is used when making measurements with a radioisotope source whereby large masses of matter are avoided in the source area.

Sometimes the nature of the measurements being performed make scatter neutrons particularly undesirable. For example, in this study measurements have been made to determine the absolute efficiency of the detector and the additional counts contributed by scatter neutrons can artificially increase the measured efficiency. In order to correct for the scatter effect a shadow cone measurement is performed. The shadow cone measurement is run in identical conditions to the main measurement, but a cone to isolate the contribution from scattered neutrons is placed between the source and the detector.

The shadow cone is made up of two sections, an iron forward section and a boron-doped paraffin or polyethylene section behind. [125] This arrangement prevents the detector from “seeing” the source directly, it will however still count neutrons that have scattered in the environment, allowing the scatter component of the initial measurement to be determined. Figure 47 shows the effect of the shadow cone on the ability of the detector to count neutrons directly from the source.

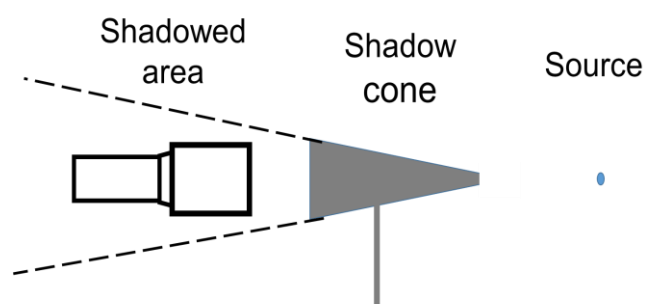


Figure 47: Schematic of the shadow cone measurement technique. The cone blocks neutrons from reaching detector unless they have been scattered in indirectly.

The counts from the shadow cone measurement can then be used to determine the scatter fraction. This in turn can be used to produce a scatter corrected measurement.

If spectroscopy data are being measured, then a pulse height spectrum can be populated from the shadow measurement to determine the scatter contribution as a function of deposited energy. Figure 48 shows the contribution of scatter neutrons to a PHS measured from a 16.5MeV monoenergetic neutron flux.

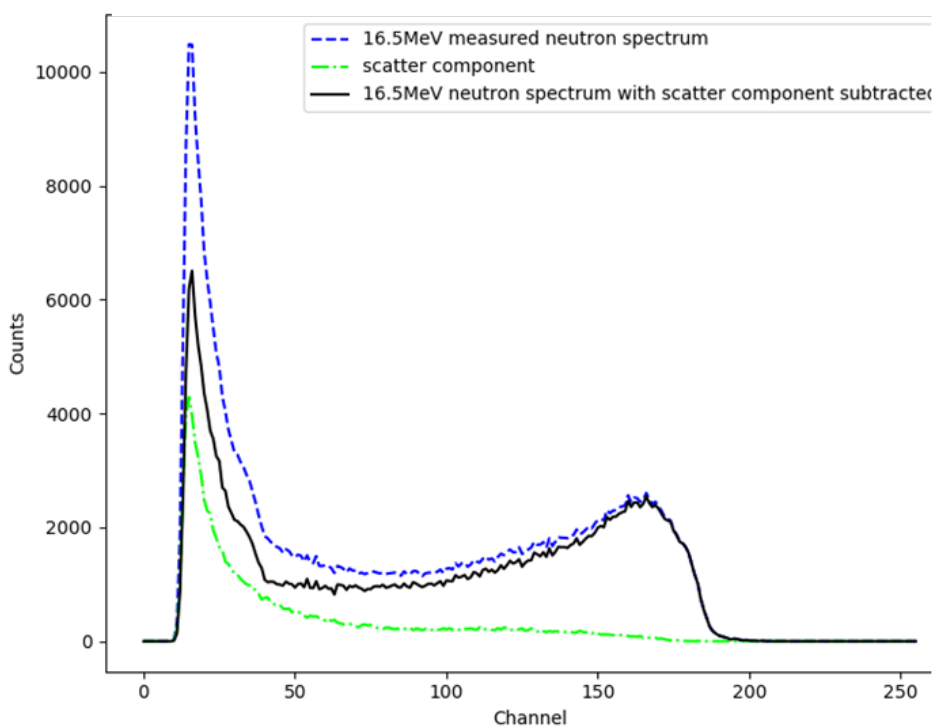


Figure 48: Scatter contribution of a 16.5 MeV irradiation of the detector. Data collected by the author using the NPL Van de Graaf accelerator. Monoenergetic neutrons are produced by the $T(d,n)$ reaction. The green line shows the measurements gathered with the scatter cone in place. The black line shows the corrected pulse height spectrum. Data for illustrative purposes only and not referred to subsequently.

As can be seen in the figure, the bulk of the scatter contribution to the pulse height spectrum is at the low energy end of the spectrum as would be expected from neutrons which have undergone at least one scatter.

3.3 EXPERIMENTAL SET-UPS AND PROCEDURE

Four sets of measurements were performed as part of this study. The following sections explain the experimental procedures carried out in each case. The experimental research began with a series of measurements of the Lancaster source after the MFA modifications had been made. These measurements were performed primarily to verify the operation of the coincidence mode and the ability of the system to measure the PFNS. In the first set of measurements, the detectors were set up in a configuration encouraging n-n coincidences. The second round of Lancaster measurements built on this work testing the system when the detectors were arranged to favour γ -n coincidences. After these measurements were a success a low-energy detector efficiency characterisation was performed at NPL in London to better understand the behaviour of the system at low incident neutron energy. At the same time, a bare source ^{252}Cf measurement was taken, and this was finally compared with the measurement of a bare ^{244}Cm source in an identical set up. Additional data collected using the Lancaster source are presented also, giving a characterisation of the system.

3.3.1 First round of Lancaster measurements

The initial set of time-of-flight (TOF) measurements were taken at Lancaster University using the Engineering Department's ^{252}Cf source. The aim of the first round of measurements was to test the ability of the system to measure the prompt fission neutron spectrum (PFNS) via a number of coincidence mechanisms between two detectors. The MFA was used in coincidence mode to measure the time separation between coincident events. Space was limited by the size of the room to a detector separation of 95 cm. This measurement was geometrically optimised to record neutrons scattering in the first detector into the second. The detectors were offset slightly from the central line of sight to the source as, by definition, any neutrons scattering

between the detectors would be scattered off the line. The detectors were arranged as in Figure 49.

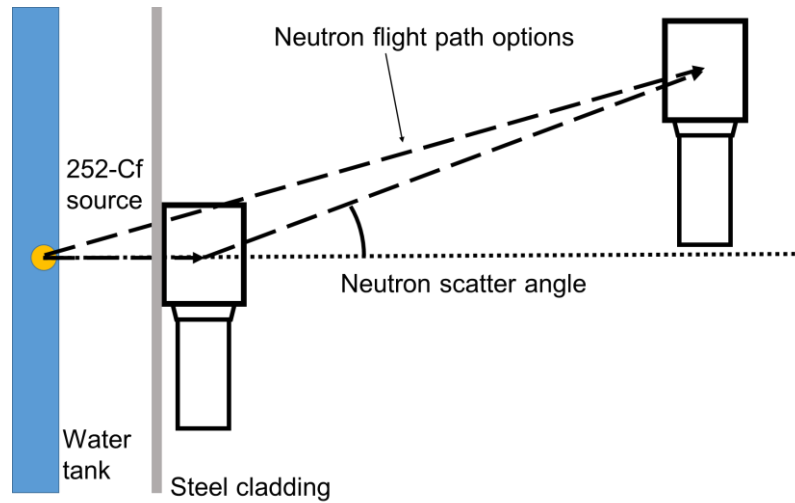


Figure 49: Detector set up for the first round of coincidence measurements made using the Lancaster ^{252}Cf source. View from above.

The two detectors were connected to the MFA with the tank-side detector connected to channel 1 and the further detector into channel 2. Initially, the MFA was run in PSD mode to set up the detectors with appropriate PSD parameters, allowing particle type sorting of the different coincidence events to be performed.

The MFA was switched to coincidence mode to collect the TOF data. A coincidence window of 240 ns was used for these initial measurements. At the time of measurement, the Lancaster source contained an encapsulated 40 MBq ^{252}Cf source. The system was allowed to collect data for 46 hrs.

3.3.2 Second round of Lancaster measurements

A second round of measurements were made using the Lancaster ^{252}Cf source. This set of measurements used a modified detector arrangement to optimise energy resolution calculated from the time separation of coincidentally-detected gamma-ray and neutron events. In this set-up the detectors were arranged in a linear geometry, with one detector given a clear view of the source with a large separation to improve the anticipated time resolution, and the other close to the tank to maximise the probability of gamma-ray detections. The detector arrangement is shown in Figure 50. In this arrangement there was 97 cm separation between the ^{252}Cf source and detector 2. Detector 1 was placed close up against the tank wall.

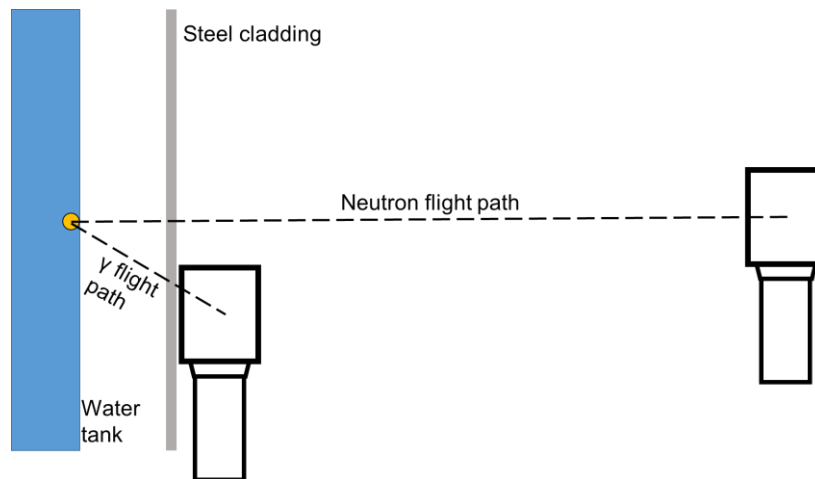


Figure 50: Detector arrangement by the Lancaster water stored ^{252}Cf source for the second round of Lancaster measurements. View from above.

These measurements were taken some time after the initial measurements with a time gap of just under one half-life of the source. The source strength was now therefore 20MBq.

As in the initial measurements, the PSD parameters and negative high voltages were set before the measurements using the PHD scatterplot mode on the MFA GUI.

3.3.3 Detector efficiency characterisation at low incident neutron energy

Although the application of the coincidence measurements using the Lancaster source showed promise, uncertainty around the response of the detector provided the motivation to characterise the efficiency of the detector at low neutron energies. Whilst a great deal of progress has been made characterising scintillators at a range of energies, such as recent studies by Pino [54], in order to verify the applicability of the EJ-301 scintillators used in this research at the particularly important low-energy end of the neutron spectrum, mono-energetic neutrons produced by the Van de Graaf generator at NPL in Teddington, London, were used to probe their efficiency response at low energy.

Neutrons for this research were produced using the $T(p,n)^3\text{He}$ reaction. The target consists of a gold body with the target mate impregnated on the surface. Compressed air cools the target to prevent the heating effect of the proton beam from warping the target and liberating the target material. Figure 51 shows the target mounted on the accelerator tube.



Figure 51: The tritium target mounted at the end of the accelerator tube. Compressed air is supplied to cool the target via the copper tube at the bottom of the image.

This research involved a sweep of different neutron energy values aimed at improving the understanding of the thresholding function of the MFA, along with the scintillant response. Following this calibrated fluence runs were made at three energies, (0.7, 0.85, 1 MeV) along with scatter correction measurements. This provides the means of calculating the detector efficiency at these energies. The detector was set up in the centre position of the NPL low-scatter facility. The front face of the detector was aligned to be coincident with the path of the beam as shown in the photograph in Figure 52.

The detector was mounted a distance of 2 metres from the reaction target of the accelerator apparatus and was aligned so that the neutron flux was aimed co-axially to the centreline of the scintillator. The MFA was set up close to the detector, connected to the anode and negative HV sockets by 3 m lengths of RG58 coaxial cable, the MFA was then connected to the data logging laptop located outside the accelerator hall in the control room, allowing control of the MFA whilst the accelerator was running. The MFA was set to record the two pulse parameters, giving the pulse height, for spectroscopy,

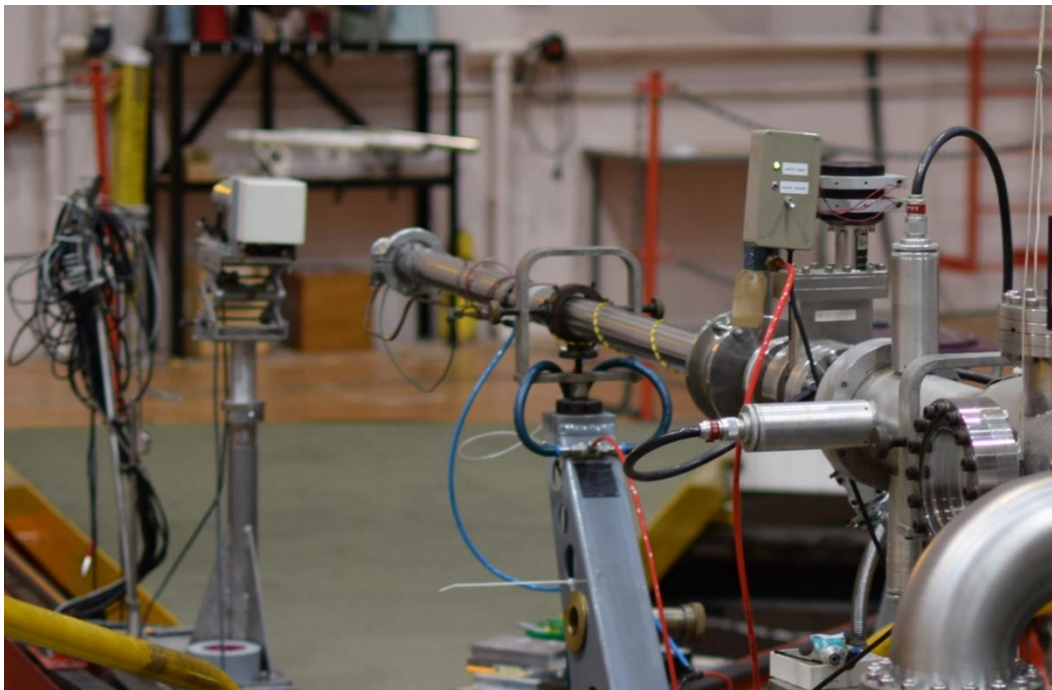


Figure 52: EJ309 detector mounted in the beamline of the Van de Graaf generator in the accelerator hall of the NPL low scatter facility. The detector can be seen in the middle-background, with the evacuated accelerator tube moving back through the centre of the photograph.

and a short integral value to provide n- γ discrimination. The short integral value was set to begin 43 ns after the pulse peak.

The PSD thresholds were set as for the Lancaster californium measurements and checked with a californium source provided by NPL. The threshold settings were also set the same as for the Lancaster measurements (100), as lowering the threshold lead to the presence of an overwhelming artefact on the scatter plot, shown in Figure 53.

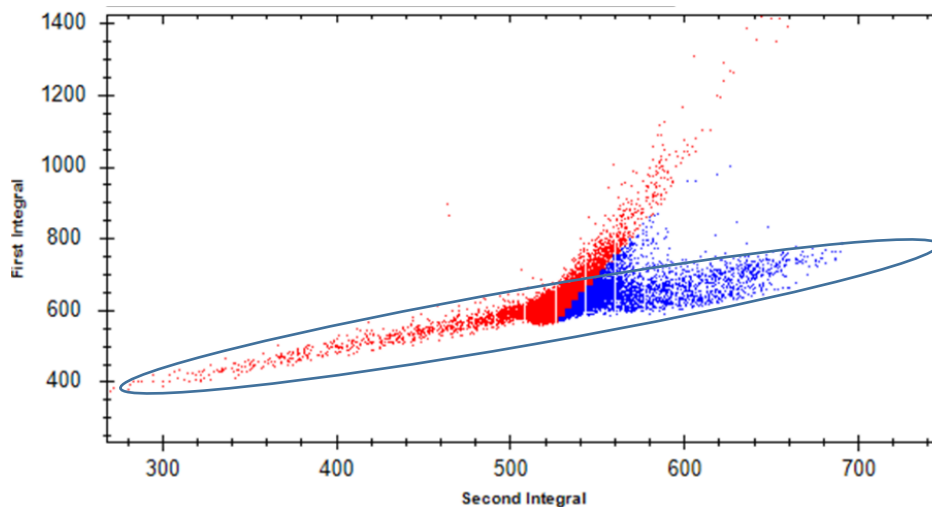


Figure 53: Scatter plot produced by the GUI controlling and receiving data from the MFA during a 1MeV mono-energetic irradiation. The linear artefact displaying unphysical events can be seen from the bottom left to mid right of the plot, identified within the ellipse, obscuring any neutron counts.

In order to locate the approximate level of the low-energy cut-off of the detector and make best use of the available time with the accelerator, a sweep of energies was performed. Initially, the accelerator was set to produce 400 keV neutrons with the intention of sweeping up until a neutron plume became evident on the scatterplot displaying the events being recorded by the MFA. It was expected that the low-energy cut-off would be between 450 keV and 1 MeV. In practice, the neutron plume did not become apparent until approximately 2 MeV; far higher than anticipated, indicating that using this system, neutrons were indistinguishable from gamma rays below 2 MeV. Whilst this would not necessarily affect the TOF system, as gamma rays can be separated from the neutron by virtue of where they land in the TOF

spectrum, it would impede the ability to measure the neutron detection efficiency of the detector.

In subsequent, higher energy irradiations of the detector, an additional difficulty emerged: as the display software from the MFA displays point data with no change for multiple events with the same pair of first and second integrals, it proves difficult to distinguish the amount of overlap between the plumes in the scatter plot containing gamma-ray and neutron events. In order to distinguish between the areas of the scatter plot containing high numbers of counts and the areas which were outliers, a heat map analysis was performed, plotting the same scatter data but with colour to demark areas of high counts. Figure 54 shows the standard scatterplot alongside the heat-map display of the data for a 2MeV monoenergetic irradiation. The heat map colour

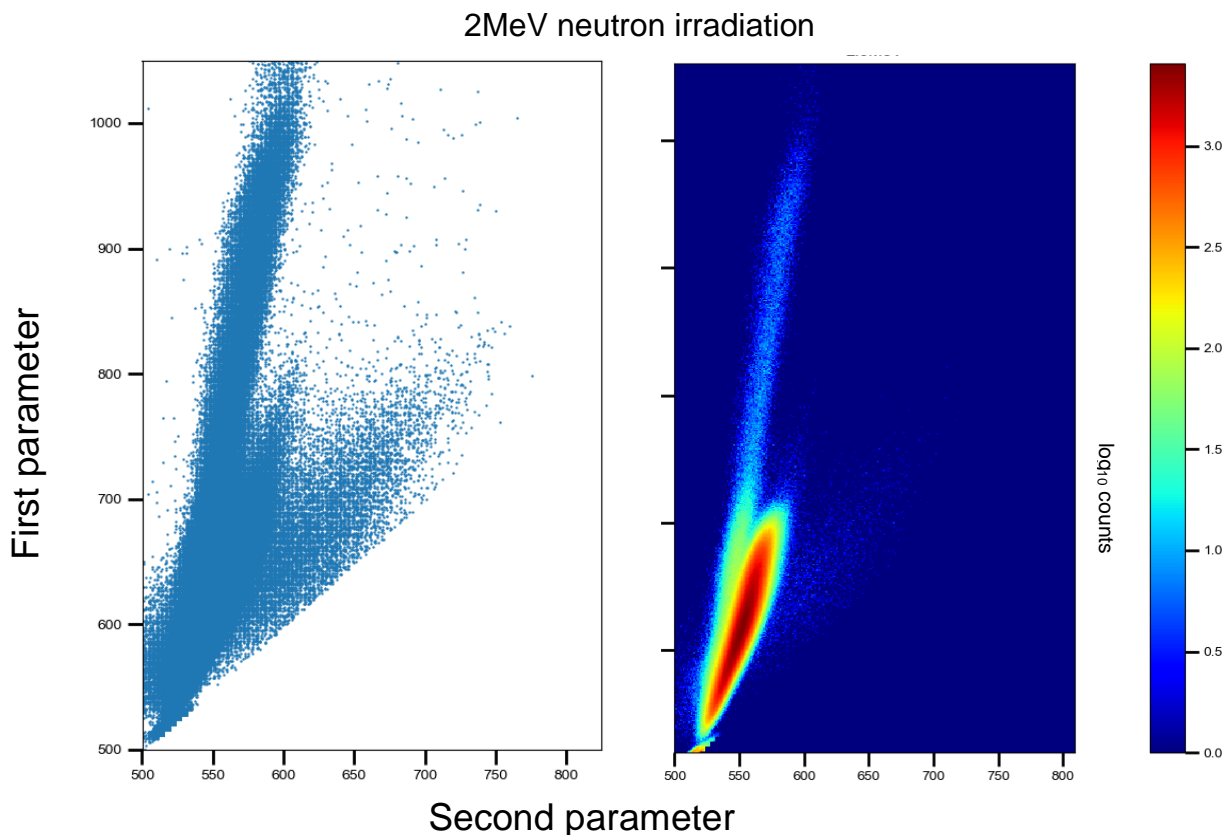


Figure 54: Scatter plots showing the same data from a 2.5MeV neutron irradiation. In the right hand plot, a logarithmic heat map reveals the neutron counts present in the data

scheme has been plotted logarithmically to show the presence of the linear artefact and the extended gamma-ray plume.

As can be seen in Figure 54, the neutron component contains numbers of counts that are orders of magnitude higher than gamma rays, and bins associated with the linear artefact contain tens of counts. Figure 55 shows measurements of four more descending energies (2, 1.8, 1.6 and 1.5 MeV) where the neutron plume can be seen retreating into the area of the graph previously swamped out between the gamma-ray counts and the linear artefact. This finding suggested that the response at lower neutron energies could be distinguished amongst the other scatter plot contributions, and that the lower threshold values were acceptable for use.

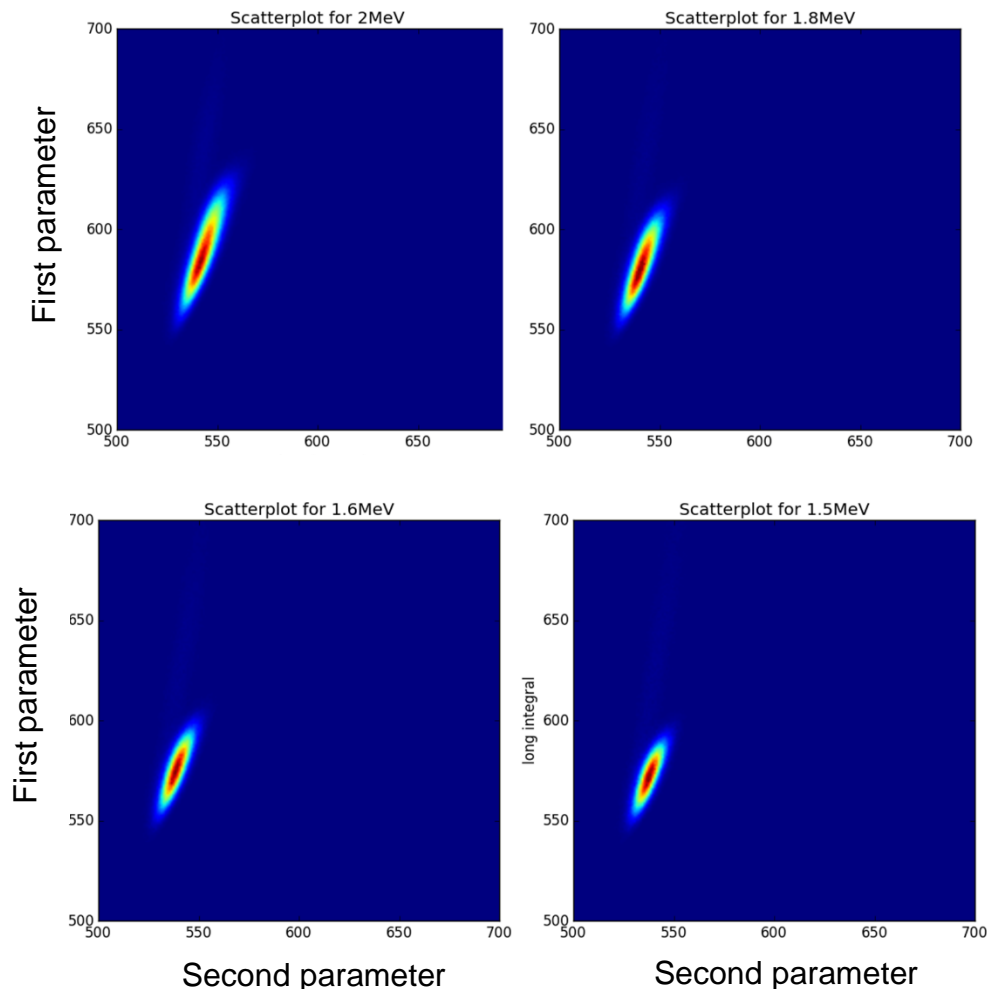


Figure 55: Neutron plumes produced by 2 MeV, 1.8 MeV, 1.6 MeV and 1.5 MeV monoenergetic neutrons from the NPL Van der Graaf accelerator. Heatmap colours are assigned linearly.

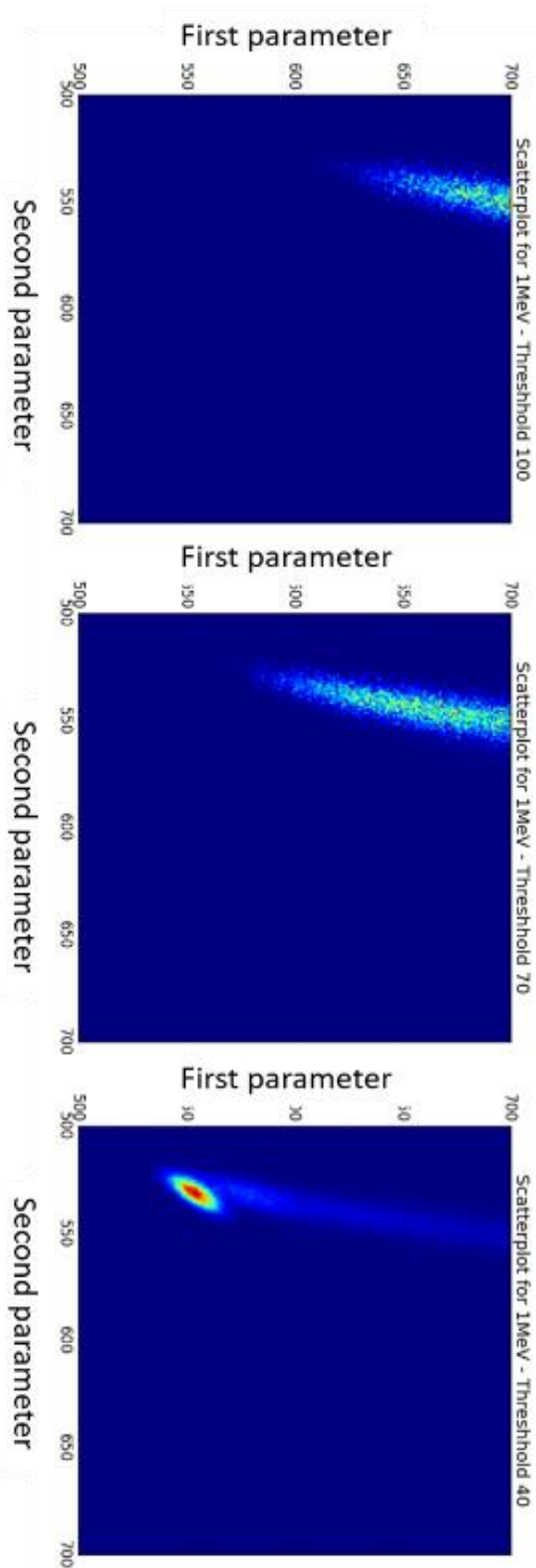


Figure 56: Plots showing the effect of threshold on the low energy cut-off. Each subplot shows a measurement of the same monoenergetic neutron energy of 1 MeV but with different thresholds.

Figure 56 shows the effect of the threshold on the measurements. The three subplots presented are three separate measurements of 1 MeV mono-energetics. The first subplot shows the data collected whilst the MFA is set with a threshold value of 100, this is the default value of the MFA. In subplots two and three the threshold is lowered to 70 and 40 respectively. At a lower threshold than 40 the spurious counts became non-negligible and began to dominate the neutron signal. As can be seen, the thresholds of 70 and 100 cut off the detector response at well above the level where 1 MeV neutrons produce a signal.

As there was now confidence that the low-energy cut-off would fall between 1 MeV and 500 keV, the Van de Graaf generator was set to produce 1 MeV neutrons, with the intention of moving incrementally down in energy, performing fully calibrated irradiations.

Three irradiations were performed: 1 MeV, 850 keV and 700 keV. Each irradiation was performed at three different threshold settings (100, 70 and 40) and identical runs were performed with the scatter cone in place to allow a scatter/ background correction. Each irradiation was run For as long as possible, but time was ultimately constrained by facility availability.

Two measurements were made per energy with the long counter: firstly a measurement of the total neutron field hitting the detector both directly from the source and from scatter off the equipment and the room, and secondly a shadow cone measurement was performed to determine the scatter component of the first measurement. Both of these measurements were made with the long counter in the 0° position with respect to the proton beam. Following the long counter calibration measurements, the long counter was replaced with the scintillator.

Analysis swiftly showed that the threshold settings above 40 yielded a low-energy cut-off above 1 MeV (see Figure 56) and data presented henceforth were measured with the threshold settings at 40.

The source parameters for the three calibrated irradiations are shown in Table 3. The uncertainties applicable to the calibrated neutron fluence provided are shown in Table 4; these values have been provided by NPL staff

and are standard counting uncertainties. The final table entry shows the total uncertainty multiplied by a reflective of a two standard deviation confidence interval (i.e. 95%).

Table 3: Parameters for the mono-energetic neutron runs using the Van de Graaf accelerator.

Reaction	T(p,n)	T(p,n)	T(p,n)
Incident particle energy E_p / keV	1573.5±3.0	1712.8±3.0	1854.4±3.0
Target thickness / keV	115±17	109±16	103±15
Mean neutron energy $E_n(\theta)$ / keV	700.1±3.4	850.1±3.2	999.9±3.2
Full width of Neutron energy distribution	122±18	113±17	106±17
$E_n(\theta+5^\circ)$ / keV	697.0±3.4	846±3.2	996.1±3.2
$E_n(\theta+10^\circ)$ / keV	687.8±3.4	836.2±3.2	984.6±3.2

Table 4: Uncertainties associated with the calibrated fluence irradiations. Calculations performed by NPL staff and provided in Instrument certificate of calibration.

Uncertainty component	Neutron Energy		
	0.7MeV	0.85MeV	1MeV
Statistical uncertainty associated with the neutron fluence rate determination	±0.6%	±0.4%	±0.6%
Long counter dead-time correction	±0.1%	±0.1%	±0.1%
In-scatter correction factor when measuring fluence rate	±0.3%	±0.3%	±0.3%
Positioning of long counter	±0.2%	±0.2%	±0.2%
Air out-scatter when measuring fluence rate	±0.1%	±0.1%	±0.1%
Efficiency and effective centre of long counter	±2.0%	±2.0%	±2.0%
Long counter long term stability	±0.8%	±0.8%	±0.8%
Variation of neutron fluence rate with incident beam current during irradiations	±3.7%	±0.9%	±1.0%
Instrument to target distance	±0.3%	±0.3%	±0.3%
Standard uncertainty in the fluence rate at the instrument reference position	±4.3%	±2.4%	±2.5%
Expanded uncertainty in fluence rate	±8.7%	±4.8%	±5.0%

3.3.4 Bare fission source measurements

3.3.4.1 NPL bare ^{252}Cf source

The first opportunity to test the system on a bare fission source was upon a source located at NPL. Accordingly, measurement using the source was made in the low scatter facility adjacent to the accelerator.

The detectors were set up on clamp stands in a similar arrangement to that behind the Lancaster source. The same distance between the neutron detector and the source was used of 97 cm, with the gamma trigger detector placed close by but not obscuring the neutron detector at a distance limited by the stand arrangement available in the low scatter facility. The detector arrangement NPL ^{252}Cf in Figure 57.

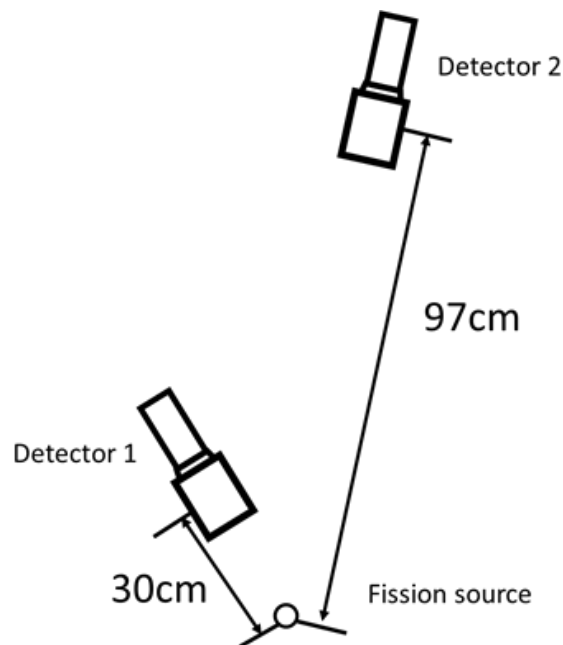


Figure 57: Plan view of the detector- source arrangement for the NPL ^{252}Cf measurement (not to scale).

As with previous measurements, the negative high voltage and PSD parameters were set up prior to the measurement being taken. The threshold settings for this measurement were set at 100 au (arbitrary units). An overnight exposure to the ^{252}Cf source was taken collecting a total of 14.5 hrs worth of data.

3.3.4.2 ^{244}Cm bare source

Following the measurements at NPL, the TOF system was used to measure the spectrum of a bare ^{244}Cm fission source. The aim of this measurement was to have to use the system to measure the under-reported ^{244}Cm spectrum and also to investigate the potential for the TOF setup to differentiate between the neutron spectra of fission nuclides. These measurements were done at Pajarito Scientific Corporation (PSC), in Santa Fe, New Mexico.

As for the previous TOF measurements, two EJ-309 detectors were used, coupled to the Hybrid Instruments MFA running in coincidence mode. The detectors were arranged as in Figure 58, optimised for γ -n coincidences with the second detector in a position so that it was not in any part eclipsed by the first detector. The first detector was placed in close proximity to the source in order to maximise the number of gamma-ray detections. The second detector was placed approximately 1 m away to avoid sacrificing energy resolution and to mirror previous geometry arrangements.

The ^{244}Cm source was set up alongside the detectors on a table-top in a large workshop area. The MFA and power supply were situated

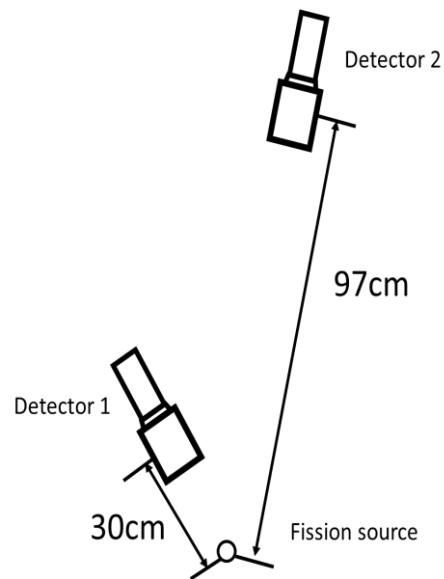


Figure 58: Plan view of the detector setup for ^{244}Cm measurement in PSC, Santa Fe, NM arranged to be the same as previous NPL measurements. (not to scale)



Figure 59: Photograph of the detector setup at PSC. The encapsulated ^{244}Cm source can be seen in the bottom centre of the photograph.

on a shelf, approximately 2 m away. Figure 59 shows the test area set up for the ^{244}Cm measurements.

The detectors were operated for some time to stabilise before the measurements started. The negative high voltage and PSD parameters were set up before each set of measurements were taken to match those used in the previous measurements at NPL. As the efficiency measurements at NPL had found that the previous threshold settings of 100 au did not utilise the full intrinsic efficiency of the EJ-309 scintillant, the threshold was set to 40 au to enable the full sensitivity of the system and reflect the lessons learned during detector characterisation.

The relatively low activity of the ^{244}Cm source necessitated a long irradiation time relative to earlier measurements. To gain the best possible statistics in the time available, the irradiation was left for 83 hrs which was limited by source facility availability.

3.3.4.3 ^{244}Cm and ^{252}Cf small scale TOF comparison

Also available for use at PSC was a small ^{252}Cf source. It was originally envisioned that this would provide the means to test the set-up at PSC with both nuclides. The source was fairly old however and the short half-life of ^{252}Cf

meant that it had decayed down to a fairly weak output. Whilst still usable as a measurable source of fission neutrons, the low geometric efficiency of the full 1 m detector setup rendered the measurement impractical in the time available. Instead, a smaller-scale TOF arrangement was set up, with the detectors considerably closer. Both ^{252}Cf and ^{244}Cm were measured in this way. As the detectors were now considerably closer there was concern that detector scatter would produce an appreciable component of the measurement. To evaluate this scatter contribution a second set of measurements with a slab of polythene between the detectors was made. This was an attempt to cut down detector cross scatter and isolate γ -n events. Figure 60 shows the arrangement of the detectors, source and polythene slab.

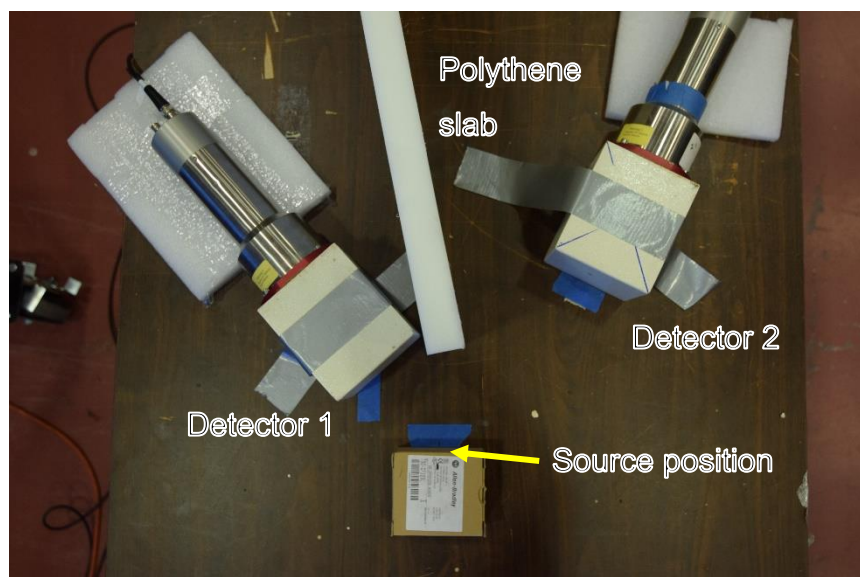


Figure 60: Photograph of detectors arranged in close in TOF configuration. The polythene slab is visible between the detectors. Identical measurements were taken with each source and both with and without the slab. Photograph taken without source in place

3.3.5 Study of sensitivity of TOF set-up to variables

A series of measurements were made to investigate the dependence of the system on various parameters using the Lancaster ^{252}Cf source. The effects of three variables were to be investigated:

- The PSD settings applied to the detectors
- Voltage applied to the detectors
- Shielding on the detectors.

Motivation for this set of measurements was two-fold: Firstly, the effect of detector voltage on the TOF spectrum had not been investigated. Secondly, an ongoing concern when interpreting the results has been the operation of the PSD algorithm. As there is considerable overlap between neutrons and gamma rays at low energy, the PSD settings had been set up to provide maximum efficiency, at the expense of accuracy. The rationale behind this has been that the incorrectly classified events would be removed by nature of their TOF signature.

Whilst misidentified gamma rays in detector 2 are easily filtered by their arrival time, misidentified neutrons in the first detector would have a more subtle effect. It was thought that if a neutron was identified in detector 1 as a gamma ray, the time it had taken to arrive would be non-negligible, resulting in an apparently faster flight time for the second neutron detected in detector 2. In order to investigate this, polyethylene shielding was used in front of the gamma detector to decrease the number of neutron triggers, and lead was also placed in front of detector 2.

The ^{252}Cf source to be used was the same water-stored source used earlier in this research based at Lancaster. The detector arrangement was near identical to that of previous measurements, although this time space was left for the inclusion of PE shielding in front of detector 1. As detector 2 remained in the same place, the movement of detector 1 by 5 cm should have no effect on the spectral shape but would however reduce the efficiency by a marginal amount. This is due to the reduction of gamma trigger detections as a result of the reduced geometric efficiency.

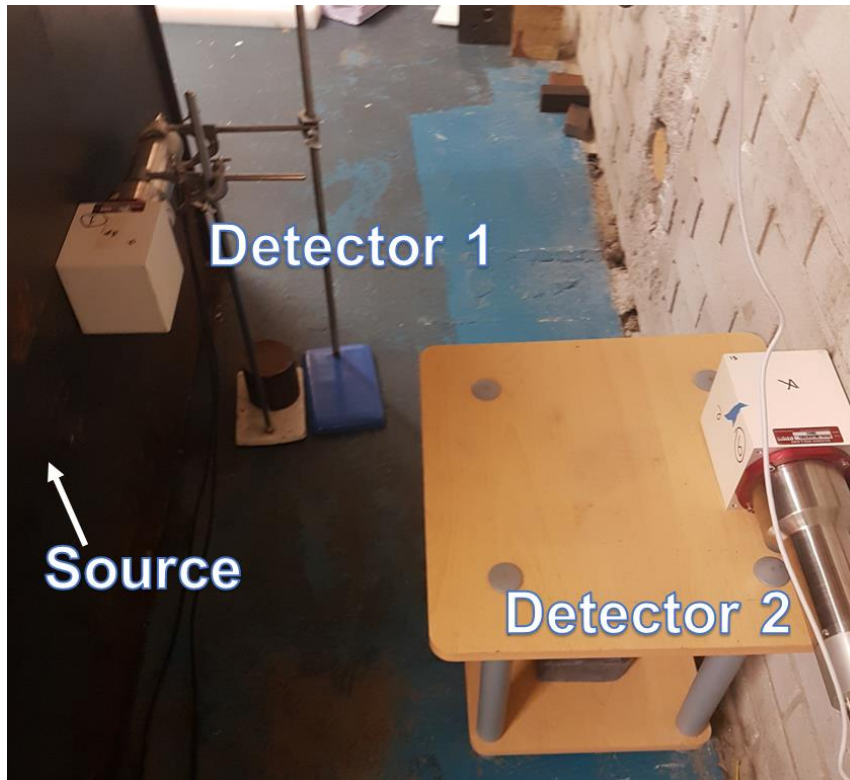


Figure 61: Detectors sited in the irradiation area to the rear of the ^{252}Cf tank in preparation for parameter study measurements.

Irradiations were carried out with a range of voltage, PSD and shielding combinations. The voltage of both detectors was varied together by the same amount and measurements were made at a high-, mid- and low-voltage combinations. In previous measurements, the PSD thresholds had been set to exclude as few of the desired particles from each detector, i.e., gamma rays in detector 1 and neutrons in detector 2 and relying on the arrival time of miss-identified particles to exclude themselves. This approach had appeared to work well for miss-identified gamma rays in detector 2, as they would arrive in the first two bins and be excluded. Neutrons being mistaken for gamma rays in detector 1, however, have a more subtle effect, and to gain insight into their effect a shielded measurement was made, using 5 cm of PE to reduce the number of neutrons arriving at the trigger detector. A lead shield was also placed in front of detector 2 to reduce gamma counts, but as described above, this was not expected to have much effect on the TOF distribution as gamma rays can be excluded by nature of their arrival time. Figure 62 shows the

detectors in a shielded configuration in the irradiation zone of the Lancaster ^{252}Cf neutron source.

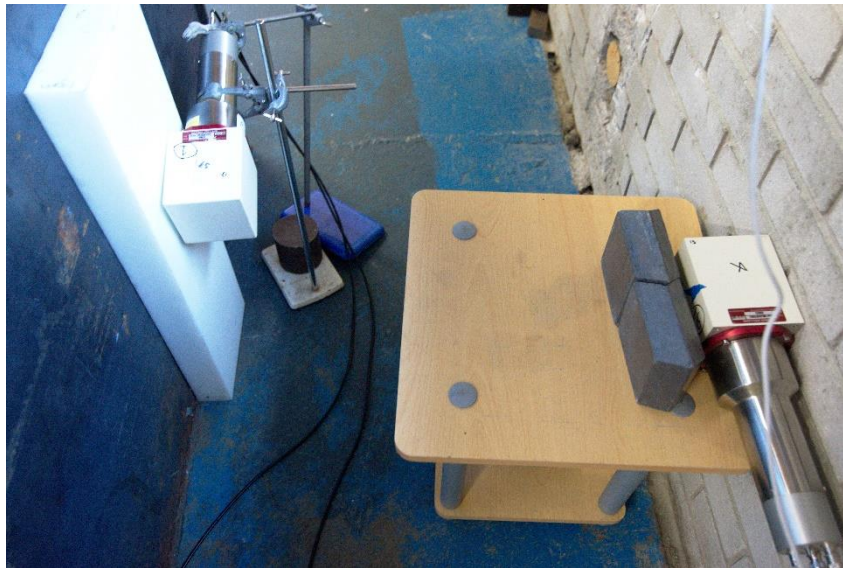


Figure 62: Detectors arranged for measurement of Lancaster source with PE and lead shielding

4 RESULTS

Chapter 3 described the equipment and experimental research carried out in the course of this research. The chapter following presents the results of these experiments, starting with early preliminary measurements exploring the operation of the spectroscopy system, and moving on through the various measurements made to characterise and apply the system.

4.1 LANCASTER UNIVERSITY ^{252}Cf TIME-OF-FLIGHT MEASUREMENTS

The first set of measurements were carried out with the Lancaster ^{252}Cf source, as described in 3.3.1. Counts were recorded in list mode on the data logging PC networked via Ethernet to the MFA. Analysis of the data shows the following numbers of the various combinations of coincident events that happened within the 240 ns coincidence window.

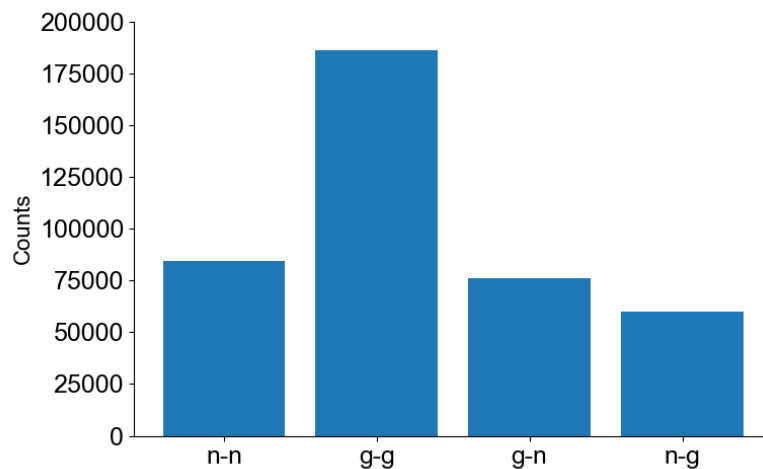


Figure 63: Bar chart showing numbers of counts of each coincidence pair.

As can be seen, the predominant registered event type are gamma-gamma coincidences. Neutron-neutron, gamma-neutron and neutron-gamma events are all also registered.

Figure 64 shows the results of applying particle discrimination logic to the individual events of the time separation distribution. Top left in the figure

shows the total events irrespective of particle classification as shown above. Top right is filtered to only contain n-n events. The bottom left and right plots show γ -n and γ - γ , respectively.

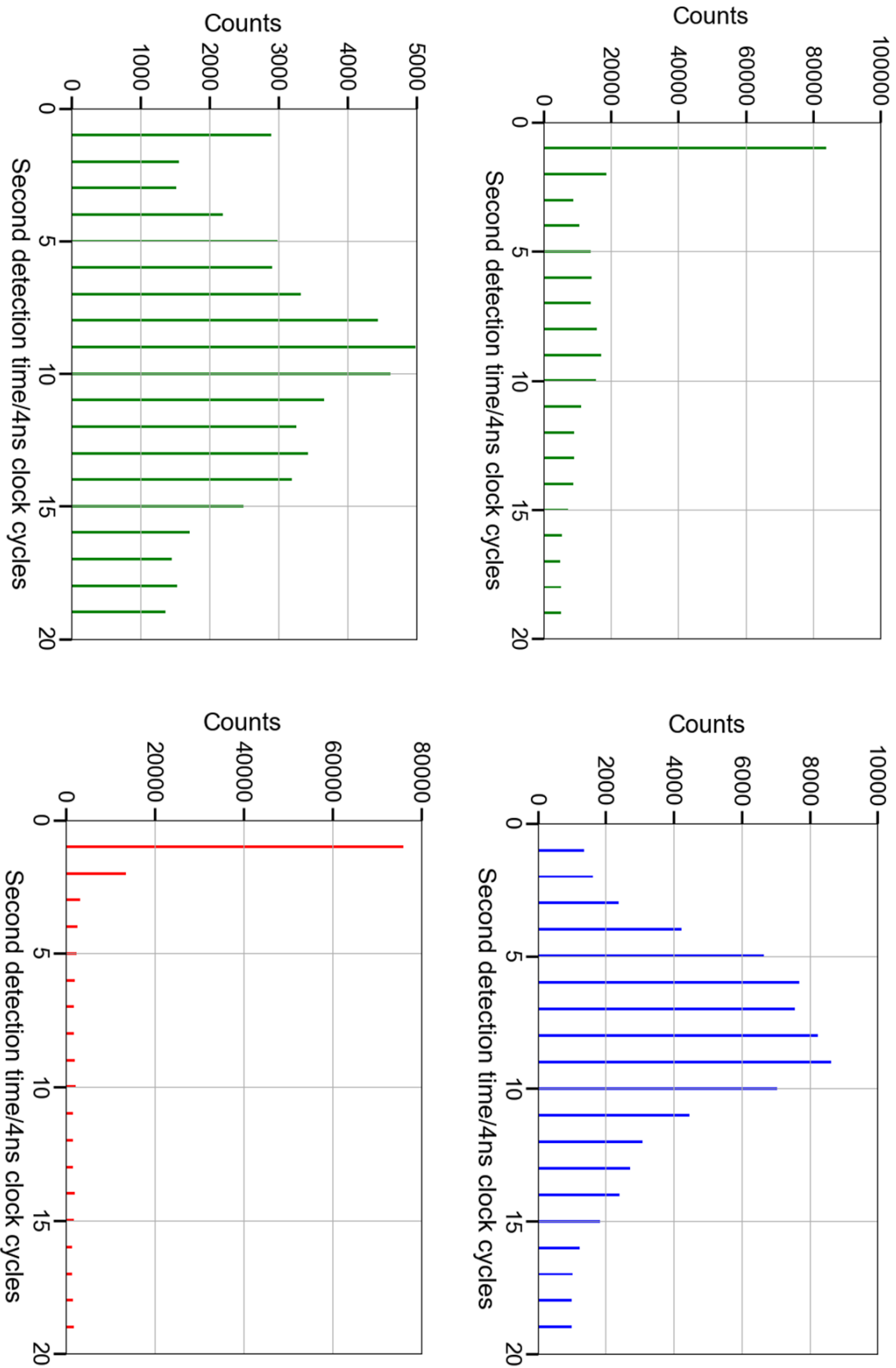


Figure 64: Time of flight spectra for the different particle criteria in the first set of Lancaster measurements. Top left shows all detected events, top right shows neutron-neutron events, bottom left shows gamma-neutron and bottom right shows gamma-gamma events.

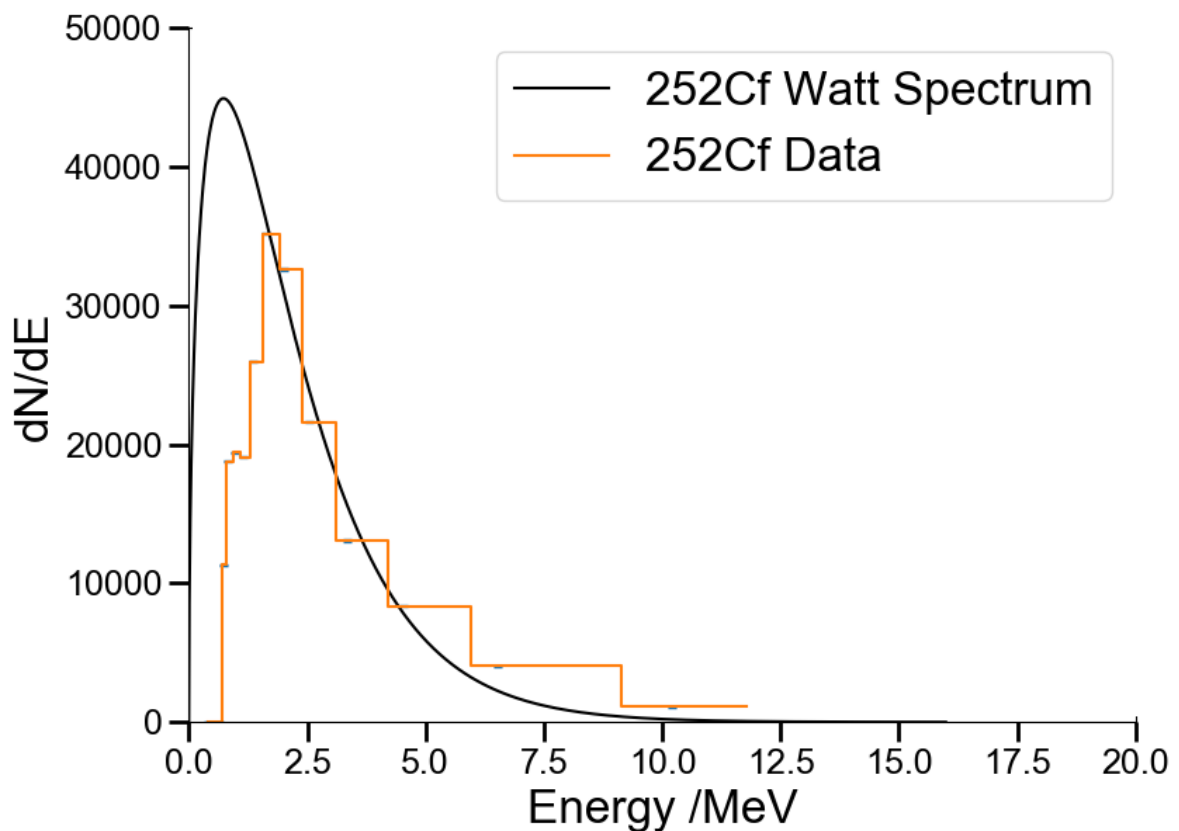
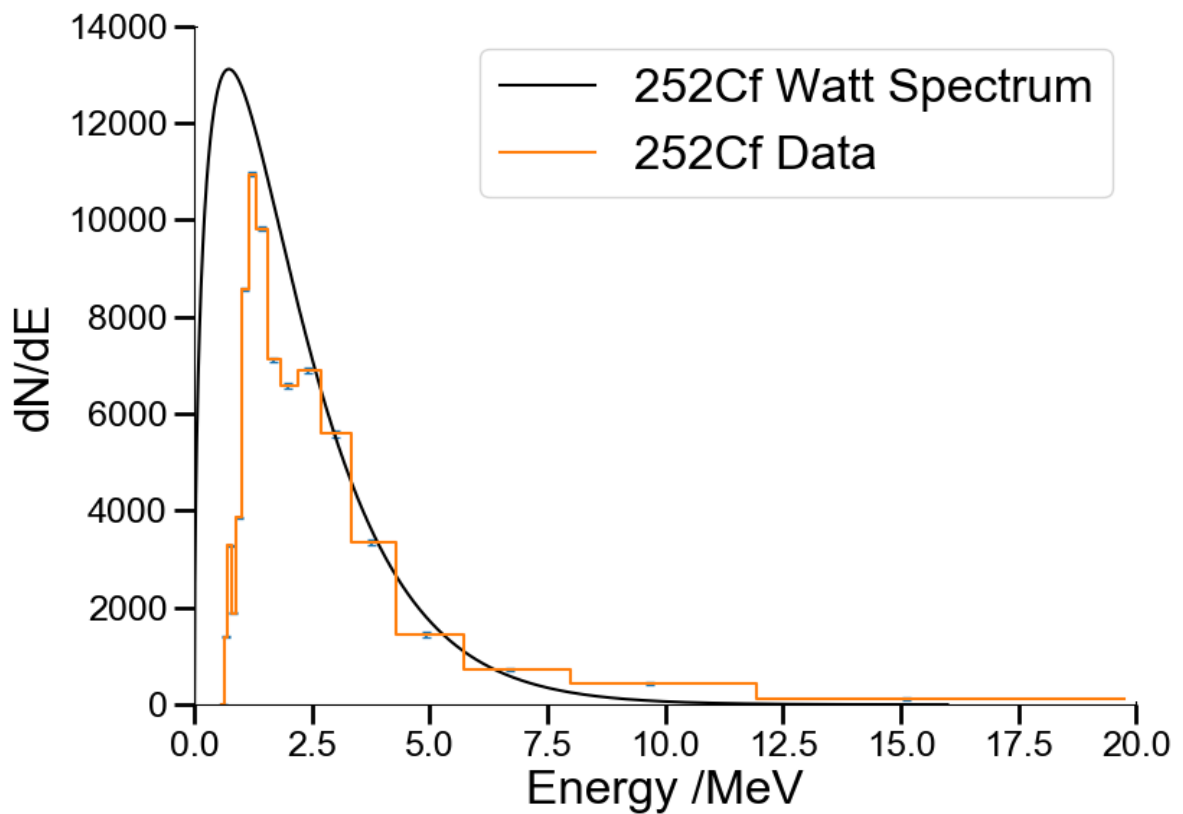


Figure 65: The TOF data converted to neutron energy spectra. The top plot shows the spectrum plotted from just γ -n events; bottom plot consists of n-n events. The black smooth curve in both plots depicts the ^{252}Cf Watt spectrum from [24].

4.2 NPL LOW-ENERGY RESPONSE MEASUREMENT

The following section presents the results of the low-energy detector efficiency measurements performed at NPL. The experimental procedure used to produce the data is described in section 3.3.3.

As explained previously, calibrated fluence runs were performed at three neutron energies at the presumed lower end of the sensitive region of the detector: 700, 850 and 1000 keV. Counts were recorded at three different threshold settings (100, 75, 40 arbitrary units) but examination of the data indicated that the two higher settings (100 and 75Au) resulted in a low-energy cut-off higher than 1 MeV. The following results therefore all represent the lower threshold of 40.

The counts collected during the irradiations are shown in Table 5. Uncertainties on the count data represent standard 1σ uncertainties. The percentage uncertainty of the integrated fluence values is the sum of various uncertainties in the calibration process and is expanded on in Table 4 (page 93). The uncertainties in the fluence data are multiplied by a coverage factor of $k=2$ to represent two standard deviations, or a confidence interval of 95%. Figure 67 shows heat-plots of the mixed γ/n field produced in the irradiations. The neutron counts were extracted from these scatter data.

Table 5: Count data collected during the calibrated fluence runs alongside the integrated fluence provided to the detector. Uncertainties on count data are standard one standard deviation uncertainties.

Incident neutron energy MeV ⁻¹	Counts	Integrated Fluence cm ⁻¹	Counts with shadow cone	Integrated fluence with cone cm ⁻¹	Percentage uncertainty on integrated fluences
0.7	3826±62	5.0x10 ⁵	167±13	1.09x10 ⁵	8.7
0.85	7945±89	1.8x10 ⁵	535±23	1.68x10 ⁵	4.8
1	28224±168	1.16x10 ⁵	792±28	7.94x10 ⁴	5

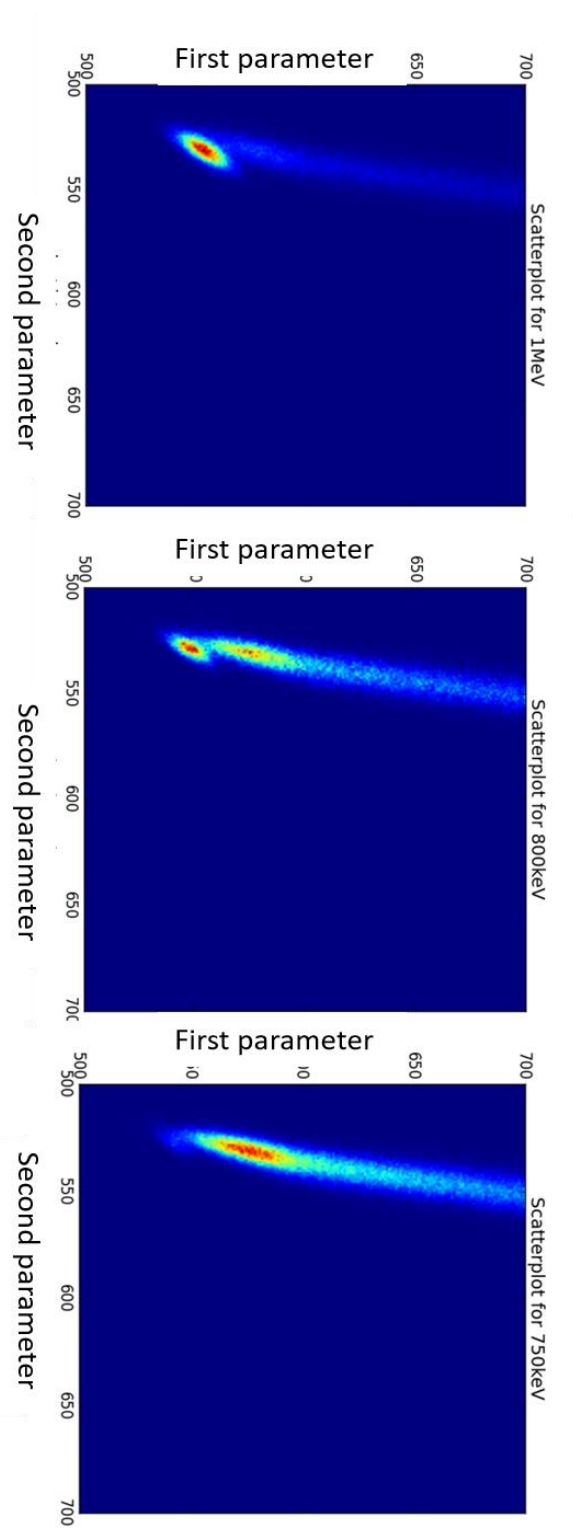


Figure 67: Heatplots of the mono-energetic irradiations showing the diminishing neutron signal.

Figure 68 shows a comparison of the counts with and without the shadow cone. The data in this case are in units of counts per incident neutron (on the detector volume) allowing the two values to be compared directly. The scatter contribution was found to be relatively small. This is consistent with the low energy of the accelerator-produced neutrons: after losing a proportion of their energy via a scattering interaction, it is likely that the leftover energy of the neutron is insufficient to be detected. The error bars in the plot show expanded uncertainties representing an enhanced confidence interval of 95%.

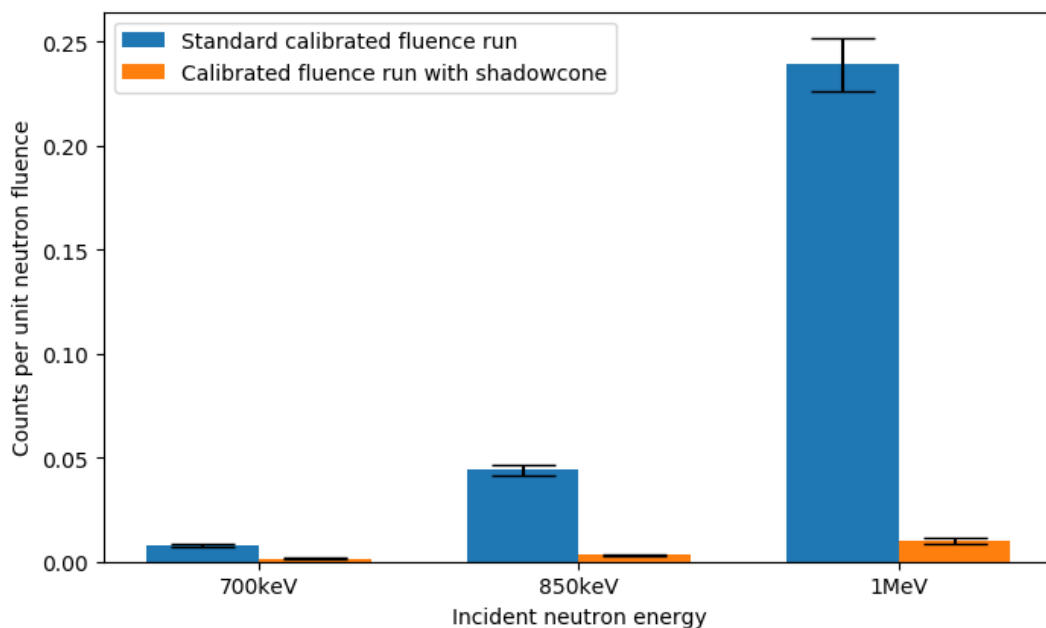


Figure 68: Plot showing the counts per unit neutron fluence both with and without the shadow cone. Error bars show expanded uncertainties representing a confidence interval of 95%.

The scatter fraction can be removed from the standard run to give a scatter-corrected value for the number of counts per unit neutron fluence, or the efficiency of the detector. Figure 69 shows the scatter corrected efficiency values. As in the previously presented data, the uncertainties are expanded to cover a 95% confidence interval.

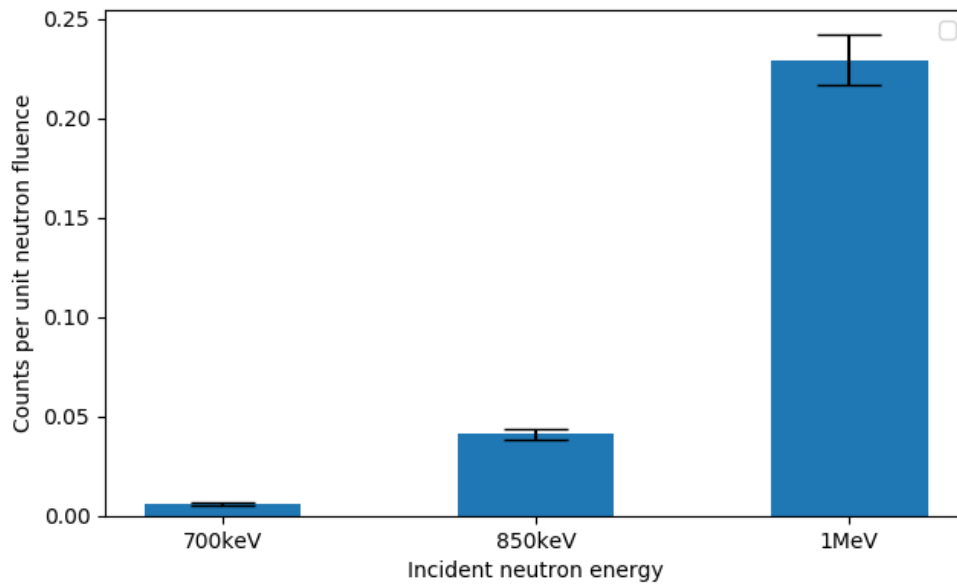


Figure 69: Plot showing the scatter- corrected efficiency values for the EJ309 detector irradiated at NPL.

Figure 70 shows the efficiency measurements alongside data reported by Pino et al. [13] for low-energy threshold values of 0.1 and 0.2 MeVee. The Pino data give measured EJ-309 efficiency values at energy values between 0 and 8.5 MeV, verified by Monte Carlo calculations. The NPL measurements suggest that the MFA threshold value of 40 is equivalent to a point between 0.1 and 0.2 MeVee. To relate the NPL efficiency measurements to the full range of energies encountered from a fission source, a fitting and interpolation process has been used.

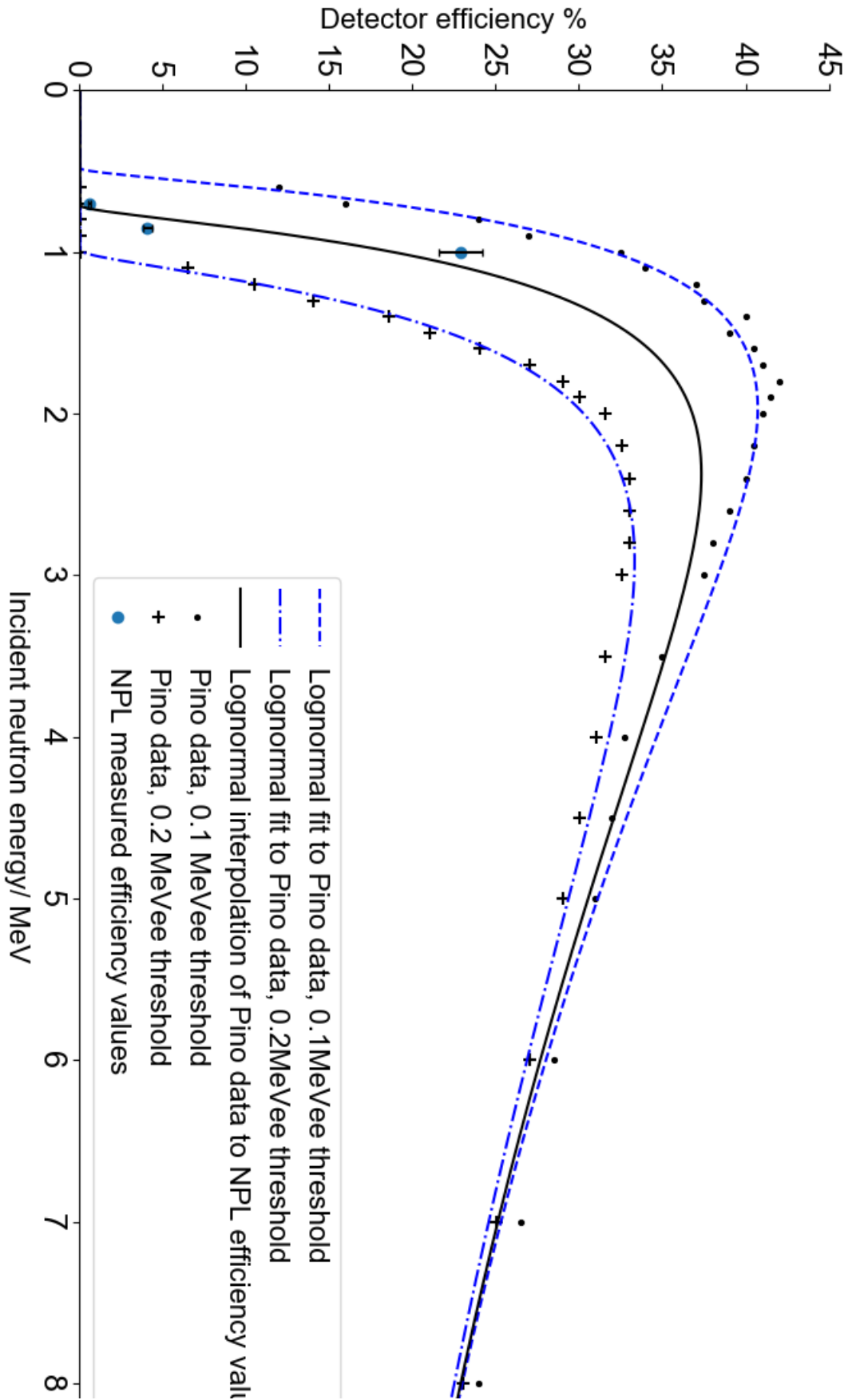


Figure 70: Plot of the lognormal curve fitted to NPL efficiency measurements alongside similar lognormal curves fitted to the Pino measurements [54]

The curves shown in Figure 70 are generated using a lognormal function, as per Equation 13.

Equation 13

$$Efficiency = \frac{1}{E\sigma} \exp - \left(\frac{\ln E - \mu}{2\sigma^2} \right)$$

Wherein E is the energy of the incident neutron fluence, and both σ and μ are fitting constants. This distribution is modified with an x offset to account for the null response at energies below 500 keV and a scaling factor. The curves are fitted to the Pino data using a least square fitting algorithm to find the four coefficients to best describe the data. A linear interpolation calculation is then used to find the fitting coefficients that best fit the NPL gathered data. This provides an efficiency function to use across the full energy range of the scintillator. Figure 71 shows the effect of the detector efficiency on the Watt fission spectrum. In this figure, the Watt spectrum has been folded with the efficiency curve to show the spectrum that the scintillator should recreate, should neutron detection efficiency be the only factor shaping the response of the system.

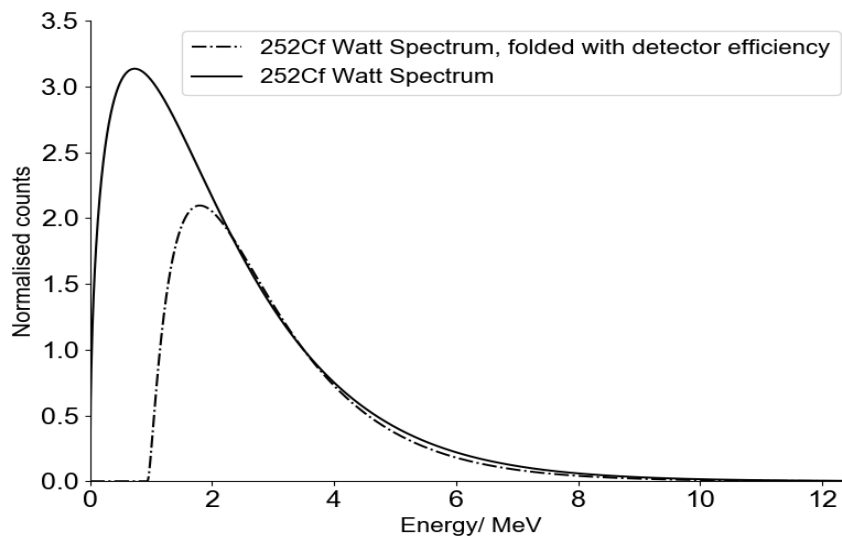


Figure 71: Effect of the detector response on the Watt spectrum. The solid curve shows the Watt distribution of neutron energies from a ^{252}Cf fission source. The dashed line shows the same spectrum folded with the efficiency of the detector as derived in this work. Both curves have been normalised to a value of 1 at 3.5MeV. Watt parameters from [24]

4.3 LANCASTER MEASUREMENTS: ROUND TWO

Figure 72 shows the time distribution of coincident γ -n events during the second spectrum measurement. The neutron energy spectrum measured in this arrangement, was calculated from the detection time interval distribution as in the previous measurements and is shown in Figure 73.

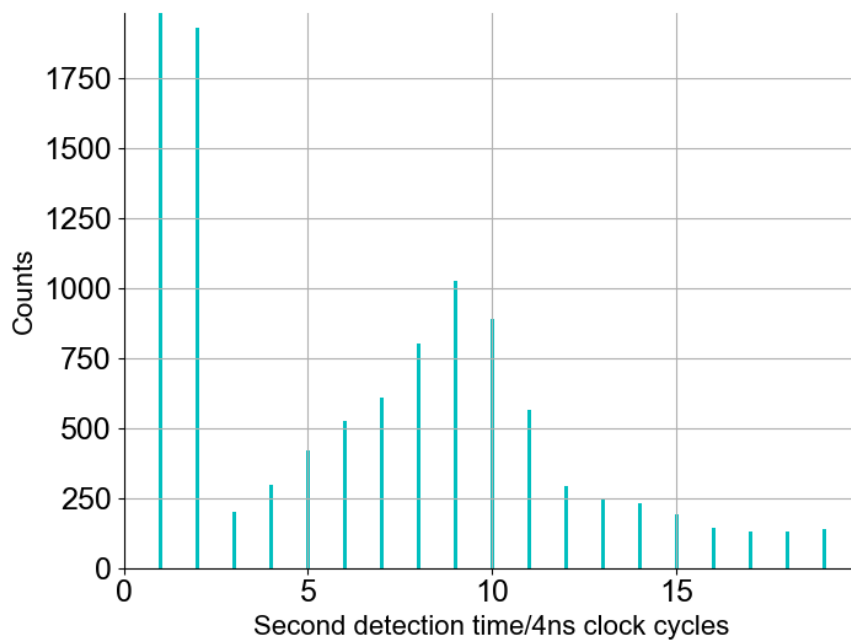


Figure 72: Time distribution of coincident γ -n events from the Lancaster ^{252}Cf fission source measured in the second detector arrangement.

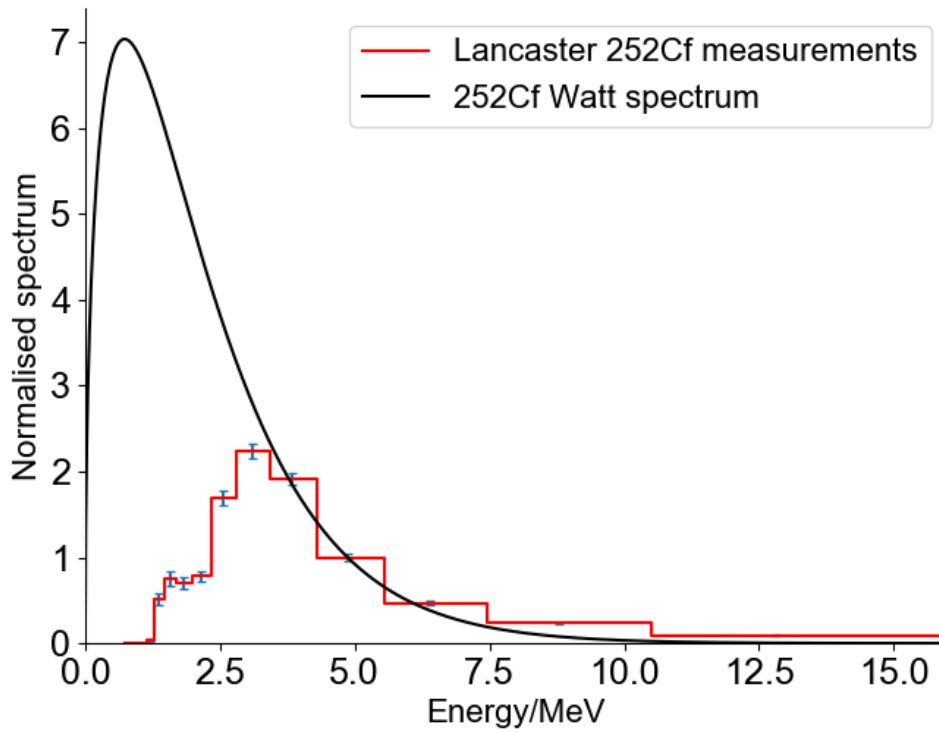


Figure 73: Energy spectrum calculated from the γ -n coincidence time distribution shown in Figure 72.

4.4 MEASUREMENT OF ^{252}Cf AND ^{244}Cm BARE FISSION SOURCES

The TOF detector system was used to measure the neutron spectra of several bare sources. The following section shows the results of the comparison of the PFNS of two different nuclides measured with the TOF system. The experimental setup of these experiments is described in section 3.3.4,

4.4.1 NPL ^{252}Cf measurement

The first opportunity to test the system on a bare fission source was upon a source located at NPL. Accordingly, measurement using the source was made in the low-scatter facility adjacent to the accelerator.

The detectors were set up on clamp stands in a similar arrangement to that behind the Lancaster ^{252}Cf source. The same distance between the neutron detector and the source was used of 97 cm, with the gamma trigger detector placed close by but without covering up the neutron detector. The detector arrangement can be seen in Figure 55.

As with previous measurements the negative high voltage and PSD parameters were set up prior to the measurement being taken. An overnight exposure to the ^{252}Cf source was taken collecting a total of 14.5 hrs worth of data. For the initial run, the system was set up with the high threshold of 100 (arbitrary units). Figure 75 shows the TOF-derived PFNS at the high threshold setting.

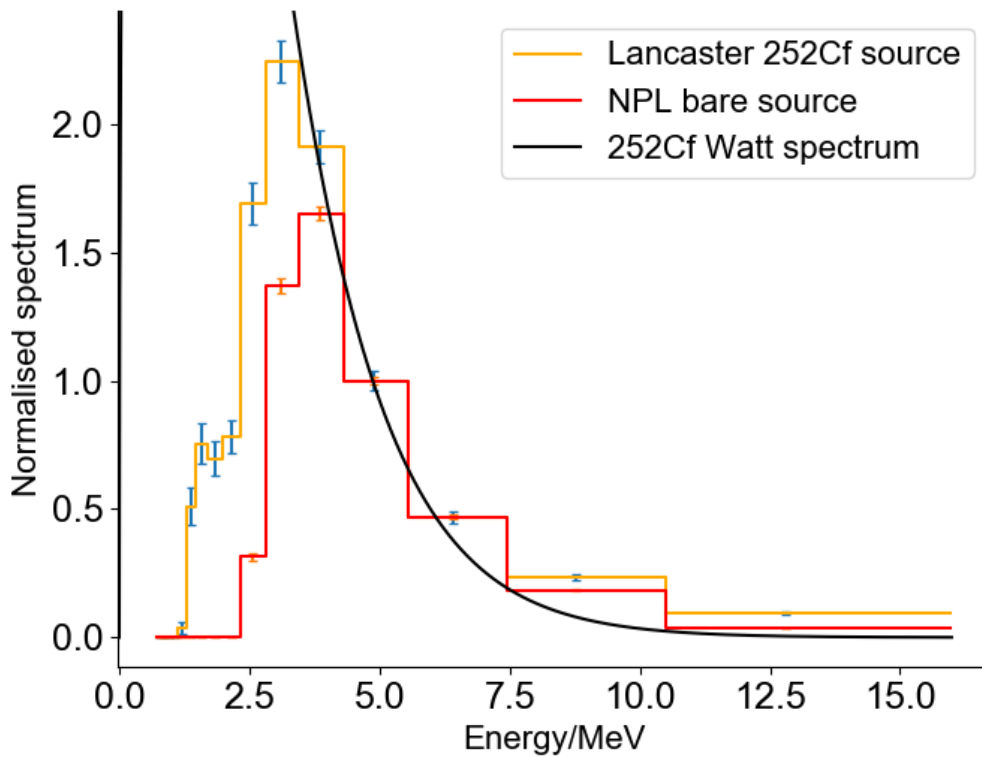


Figure 74: Comparison of energy spectrum measurements from NPL and Lancaster 252Cf sources. The reference Watt spectrum is shown for comparison. All are normalised to 1 at the same energy bin of 4.89MeV

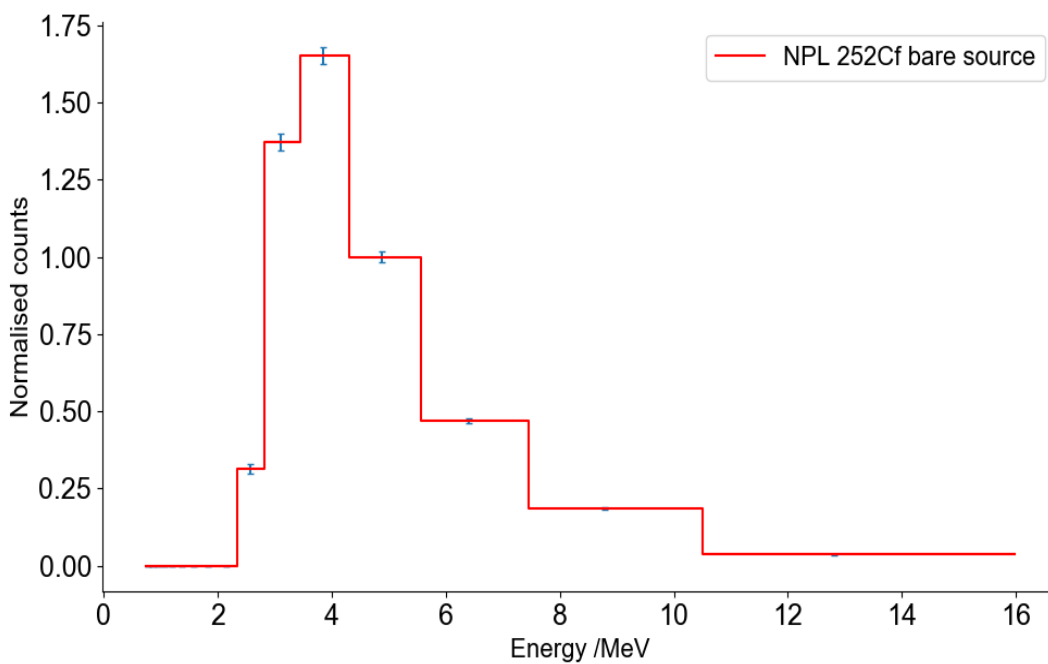


Figure 75: PFNS measured with the high trigger threshold on the NPL bare ^{252}Cf source.

The effect of the threshold is apparent in the spectrum as the response at energies below 2 MeV is very low. The high threshold was also used on the Lancaster measurements. Comparing the two spectra in Figure 74 shows a similar effect. The Lancaster data however exhibit significantly higher numbers of the low-energy neutrons.

As the source neutron spectrum should be identical for both measurements and the settings on the data acquisition system were the same, it stands to reason that the different spectrum shape must be due to the environment in which the measurements were taken. The softening of the measured neutron system can be explained by the scatter of neutrons in the environment around the source, particularly due to the water tank in which the source is stored.

As described in section 3.2.1, the Lancaster ^{252}Cf neutron source is moved to one side of a water tank in order to expose the instrument to the neutron flux. Despite being at one side, there is still 20 mm of water between it and the instrument, providing a source of hydrogen nuclei to scatter neutrons, both reducing the neutron energy and providing a longer flight path. In addition, oxygen nuclei can scatter neutrons back from the main bulk of the tank producing the same effect.

Figure 76 shows the NPL ^{252}Cf measurements alongside a modified efficiency curve. In this plot the reference spectrum has been folded with modified efficiency data, which has been fitted to the low energy cut off of the measurements with this threshold setting. As can be seen, there is little alteration to the fit at high energies, but the overall shape of the curve is much better predicted.

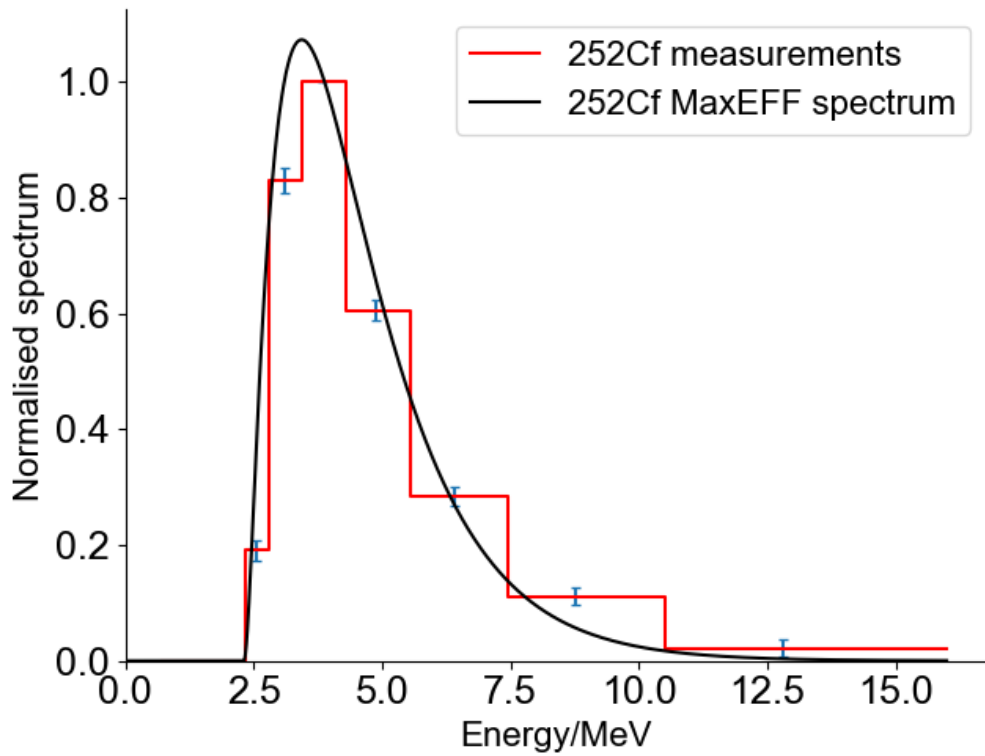


Figure 76: NPL ^{252}Cf data plotted alongside the reference ^{252}Cf Maxwellian spectrum, folded with detector efficiency curve fitted to low energy threshold of these measurements.

4.4.2 ^{244}Cm source measurements

The first true application of the system was the measurement of the ^{244}Cm bare fission source. Figure 77 shows the results of the measurements taken, with the same detector layout as at NPL. Also plotted are reference Watt and Maxwellian spectra for ^{244}Cm , folded with the detector efficiency curve as measured in the previous calibration measurements. This curve shall be referred to as the WattEFF spectrum. The measured data are in good agreement with the reported reference curves above 2 MeV.

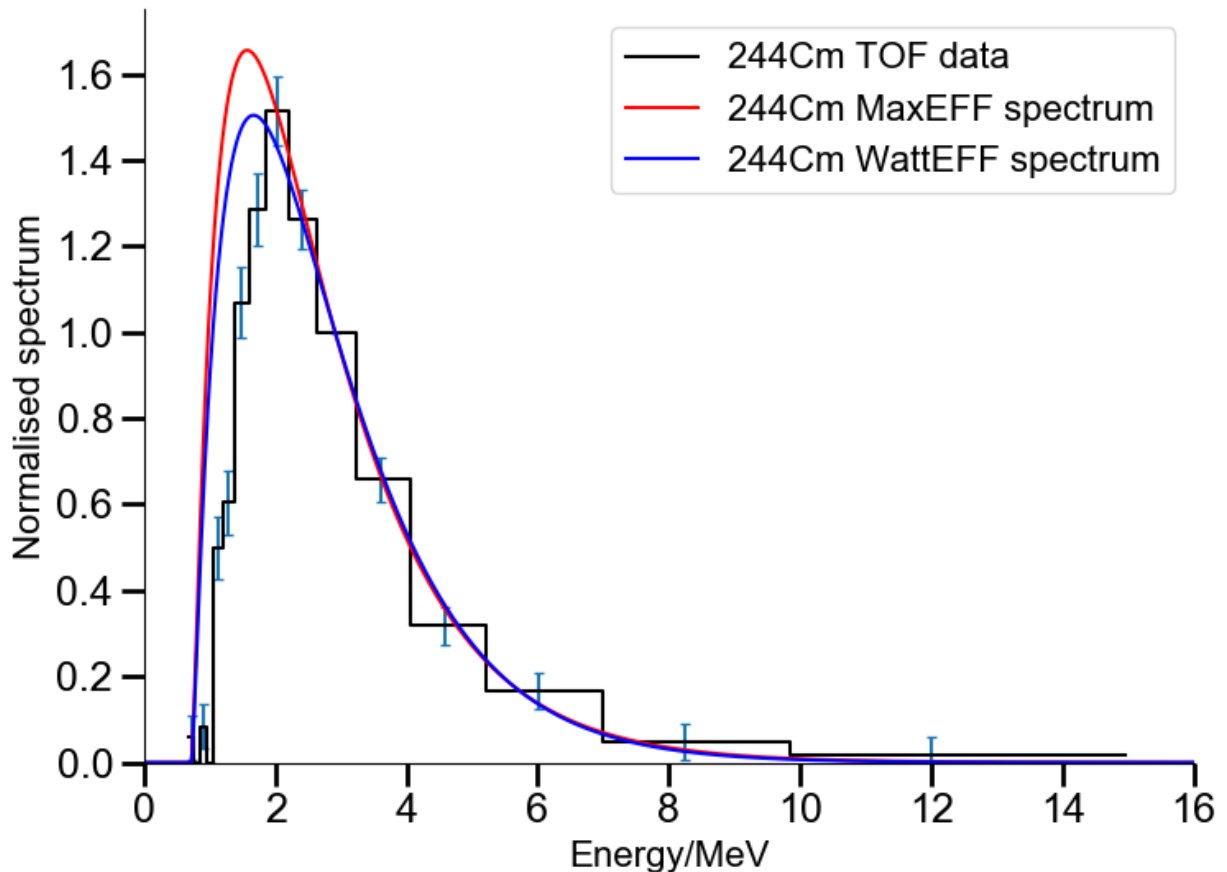


Figure 77: PFNS of the PSC bare ^{244}Cm source as measured with the TOF system. All plots normalised to 1 at 2.9MeV. Reference spectra in black plotted from parameters obtained from [24]

In addition to plotting the data alongside reference curves, a least square fitting algorithm was used to fit the Watt and Maxwellian spectrum to the measured data. For the Maxwellian spectrum, the single parameter “T” is adjusted to fit the curve, in the Watt spectrum, two parameters, a and b are adjusted. In both processes, the curves and data were normalised to 2.9 MeV

as in the previous figure. Figure 78 shows the curves fitted to the measured data.

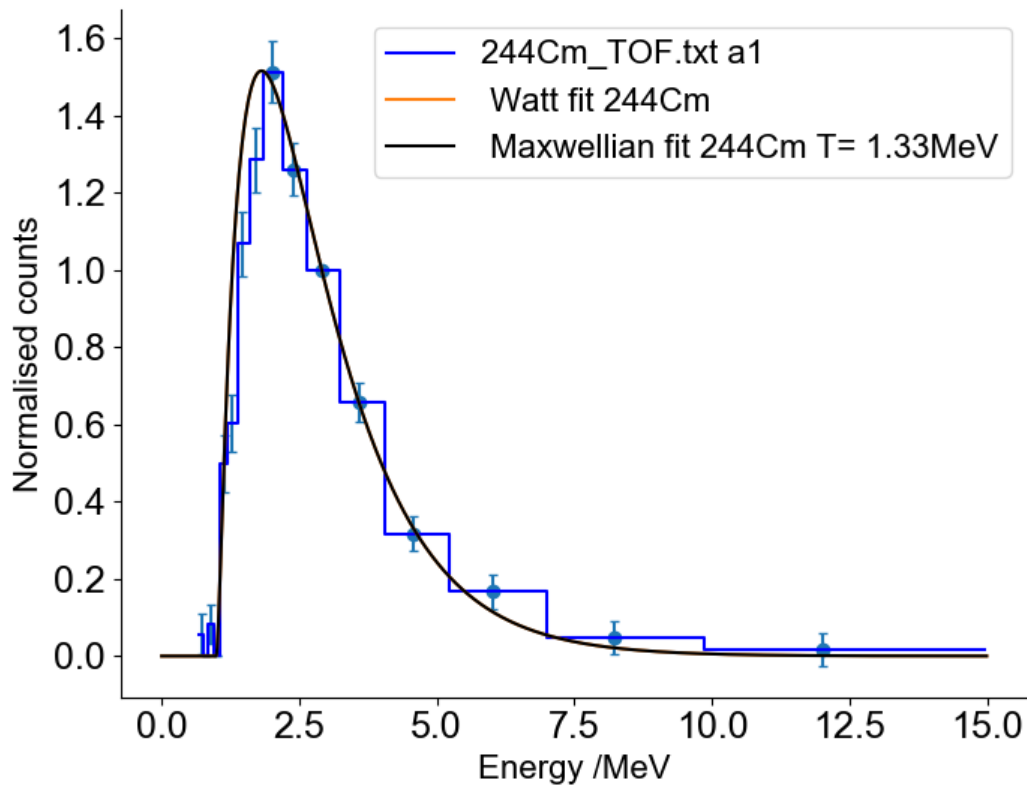


Figure 78: Watt and Maxwellian spectra fitted to the measured data. Watt fit obscured by that of the Maxwellian. Points used in the fit marked with circles.

The fitting process gave results of $T=1.336 (\pm 0.07)$ MeV, for the Maxwellian spectrum, and $a=0.918$ and $b=1.151$ for the Watt parameters. The fit was made using the high energy edge of the distribution, as this approach gave the best fit. As the detector threshold is higher than the energy of the neutrons being measured, the low energy edge of the spectrum is dictated by the threshold rather than the source spectrum.

The uncertainties on the fit were determined via a Monte Carlo procedure. Pseudo datasets sampled normally around the measured data were used to determine a large number of fits. The results of these fits were binned allowing the distribution of possible fits given the uncertainties to be

determined. A gaussian distribution fitted to this data gave the standard deviation of the Maxwellian fits, which is quoted here as the uncertainty.

4.4.3 Comparison of ^{252}Cf and ^{244}Cm in a small-scale TOF setup

In addition to the recreation of the NPL setup, a small-scale TOF measurement layout was constructed at PSC. The improved geometric efficiency of the smaller setup allowed a small ^{252}Cf source to be measured as well as the curium source. The TOF distributions measured for the two sources are shown in Figure 79.

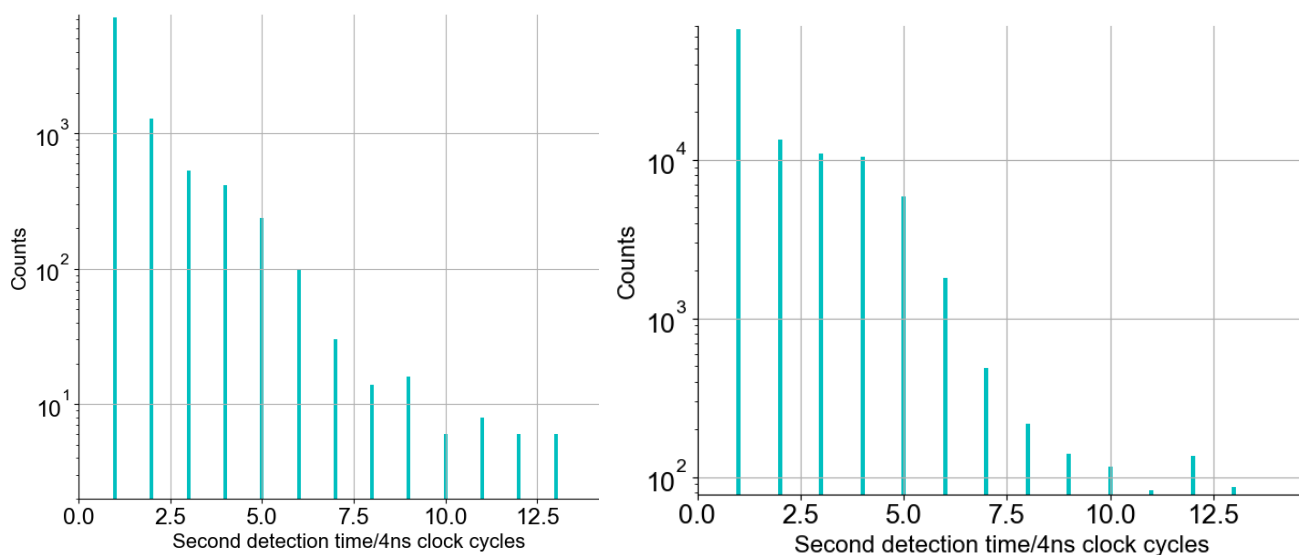


Figure 79: TOF distributions for the small separation TOF measurements. The left-hand plot shows the data collected from the ^{252}Cf source; the right-hand plot shows ^{244}Cm data. Note the logarithmic count axis.

In both TOF distributions the gamma peak in the first bin can be observed. This feature is present despite the fact that PSD is used to filter events and reflects the fact that the PSD process is imperfect, particularly at low energies. As the PSD parameters were set to over-classify neutrons in the second detector in order to maximise counts, this peak is particularly prominent.

Figure 80 shows the energy spectra derived from the TOF data. The plot shows both nuclides measured, both with and without a PE scatter-guard between the detectors. The energy conversion calculations were conducted using the separation between the source and the centre of the second

detector. As in previous treatments of the data, the first two bins of the TOF spectrum were discarded to remove the gamma spike.

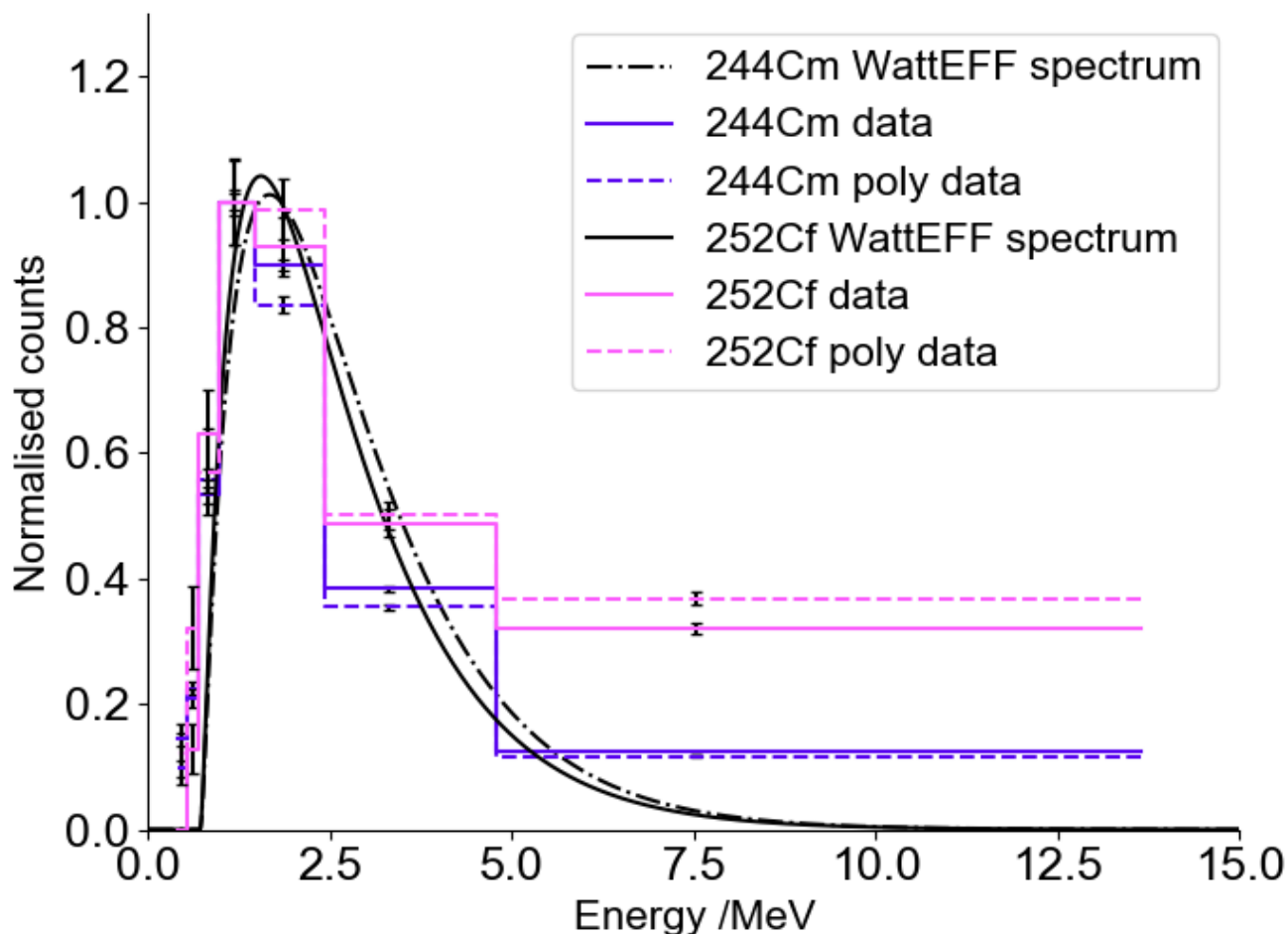


Figure 80: Energy spectrum for ^{252}Cf and ^{244}Cm derived from TOF data All datasets normalised to 1 at the peak.

Uncertainties on the counts around the peak preclude a confident assessment of the relative differences between the spectra, particularly in terms of discriminating between sources on the basis of locating the peak. Differences in the efficiency-corrected Watt spectra in that area do suggest however that, with better counting statistics, the two sources may be discerned from one another on the basis of peak position.

The presence of the PE-scatter guard appears to have a small influence on the observed spectrum, suggesting that misidentified neutrons

from detector 1 scattering into detector 2 have little effect on the measurements. However, poorer statistics in the californium measurements around the peak make identifying a trend difficult. At higher neutron energies, the distribution of events with the PE scatter-guard does show separation from the measurement taken without PE.

The largest deviation from the standard ^{252}Cf watt spectrum is in the final two bins, with considerable overestimation of the high-energy end of the spectrum. Most notable, however, is the separation between the two nuclides, with the ^{252}Cf generating a considerably greater discrepancy. One potential explanation for this effect is the greater multiplicity of ^{252}Cf relative to ^{244}Cm [24]. Greater numbers of higher-order groups of neutrons would increase the probability of double-neutron detections being misidentified as single, higher-energy neutrons.

To investigate this effect further, the same setup was recreated in Lancaster using the ^{252}Cf . This arrangement was measured with PE and lead shielding in front of detector 1 and detector 2, respectively. The effect of the PE was first investigated via the scatter-data gathered by the PSD algorithm on the MFA shown in Figure 82 and Figure 81. The pulse height data for these plots were collected over two 10-minute runs.

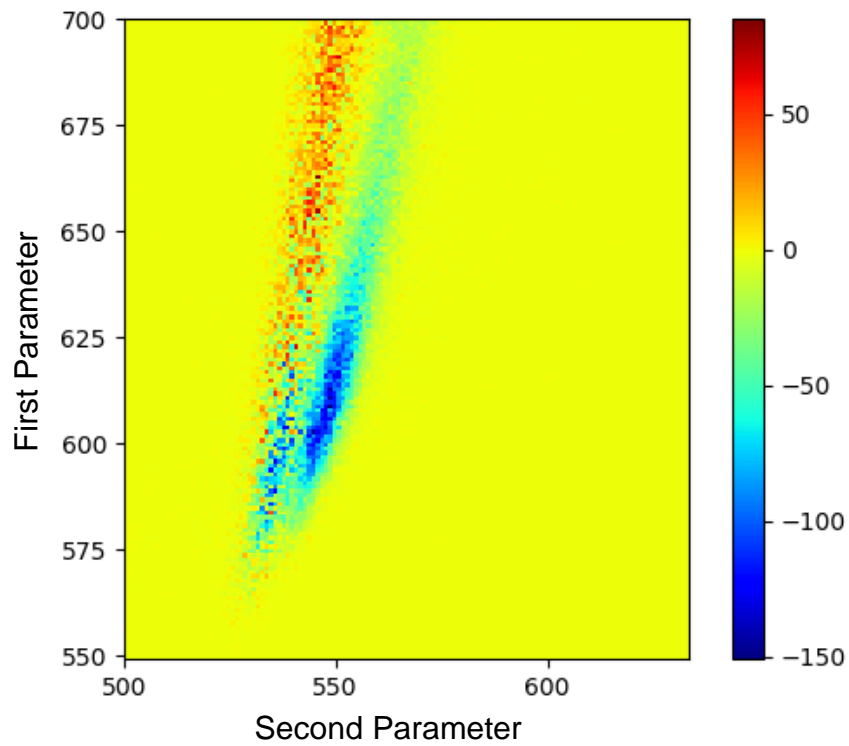


Figure 82: Heat map showing areas of difference between measurements with and without PE shielding. Areas in blue show where counts have been subtra

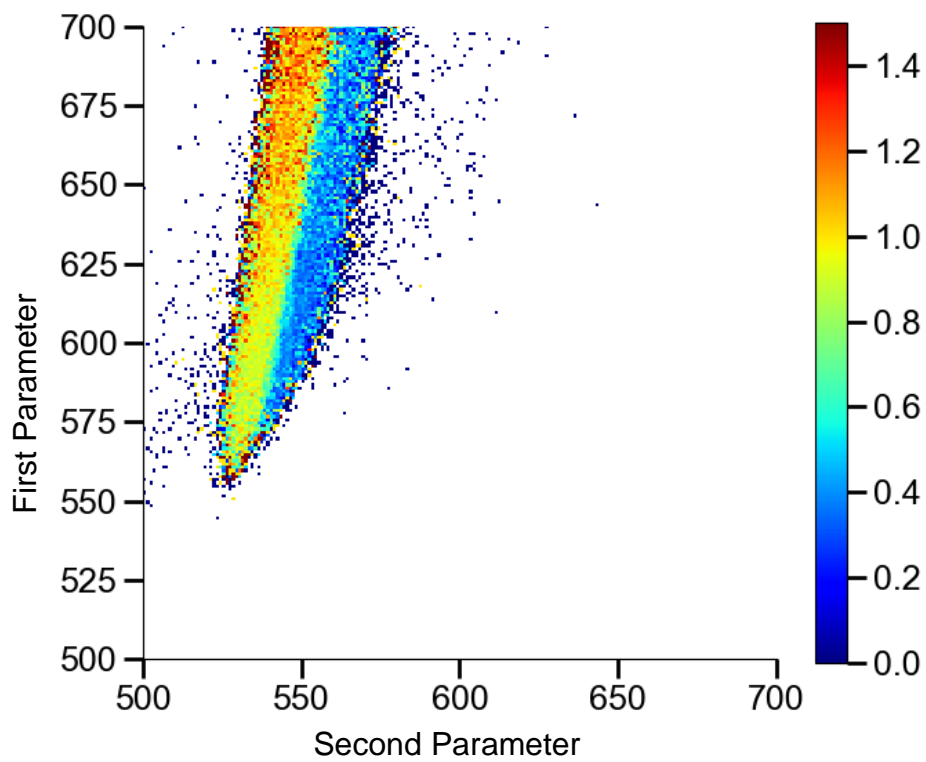


Figure 81: Heatmap showing the ratio of counts made with and without PE shielding in front of the detector.

As can be seen in Figure 82, the area on which the PE shielding has the greatest absolute effect is with the low-energy neutrons. Computing the ratio of counts with shielding to those made without, however, shows the change is approximately even across the neutron area of the scatterplot. Some gamma rays are also removed at low energy. The average ratio of shielded to non-shielded measurements is 0.35, suggesting the neutron fluence on the detector is reduced by two thirds. Figure 83 shows the TOF data gathered with and without the shielding. As can be seen, the high-energy bins are reduced by a marginal amount, potentially reflecting the reduction in multiplet neutron detections as described previously. The effect is not however strong enough to completely explain the overcounting in higher bins.

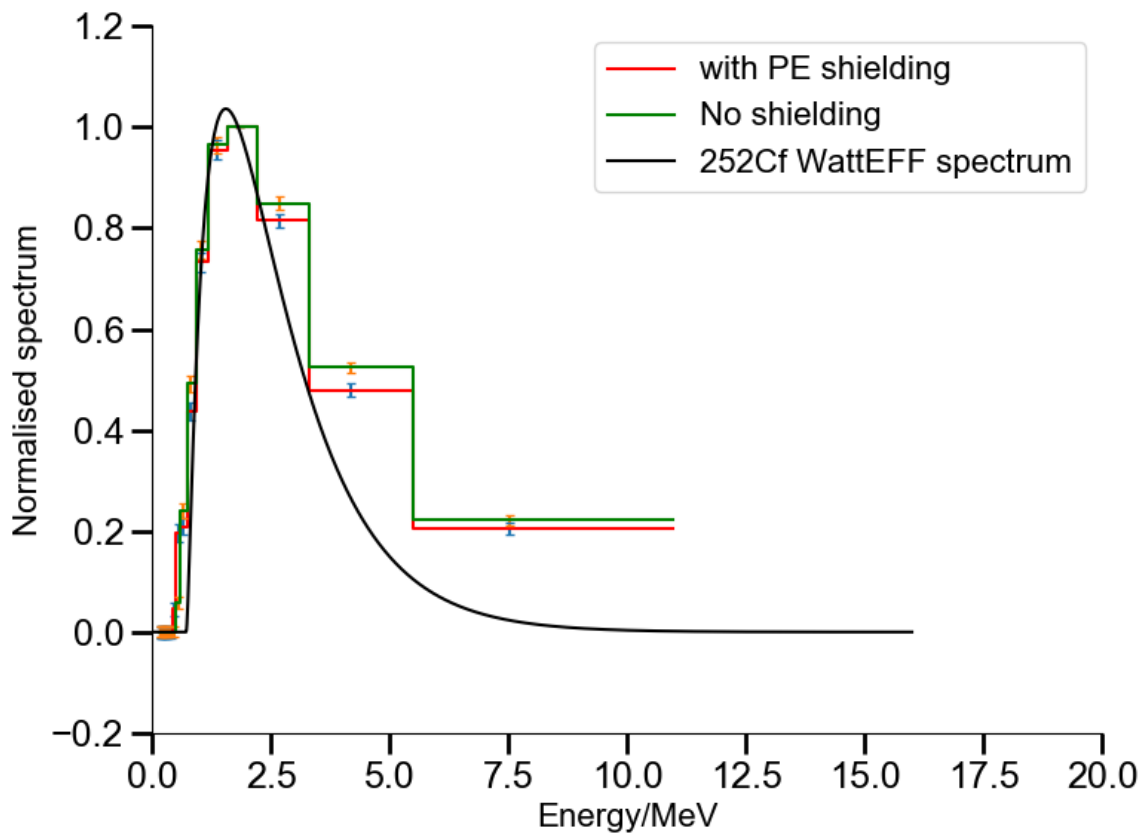


Figure 83: Small separation TOF measurements made at the Lancaster source with various shielding materials on the detectors.

4.5 PARAMETER STUDY ON TOF SYSTEM

Several experiments were performed in order to investigate the response of the TOF system to the Lancaster water-stored ^{252}Cf source. The experimental setup is described in section 3.3.5.

The first set of measurements were taken with varying detector negative high voltage. The effect on the spectrum is shown in Figure 84.

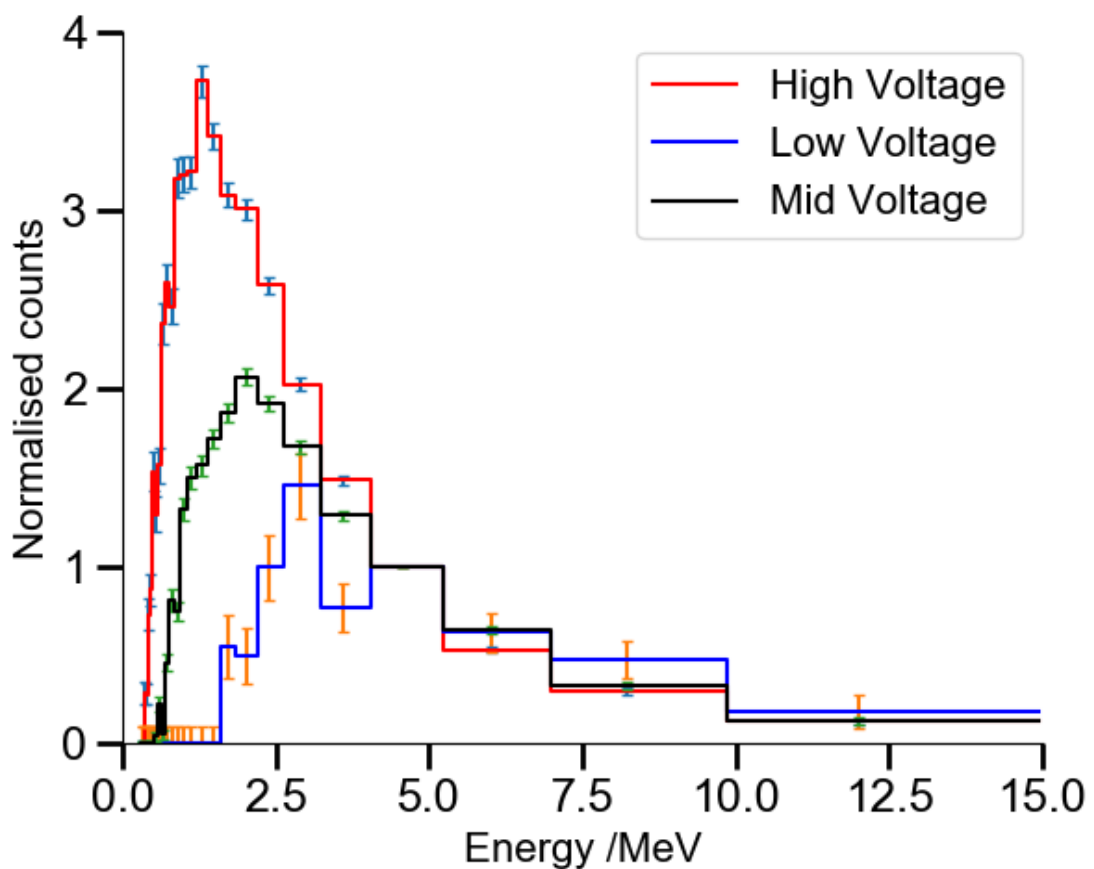


Figure 84: The effect of varying detector negative high voltage on the measured TOF spectrum.

As can be seen, varying the voltage applied to the photomultiplier elicits a similar response to changing the threshold values, moving the low-energy cut-off lower as voltage increases. The high-energy response appears to be consistent between voltages within statistical variance.

The results for the measurements made with shielding and PSD alterations are shown in Figure 85 and Figure 86. As can be seen in the first figure, the primary effect is a lowering of the high-energy response.

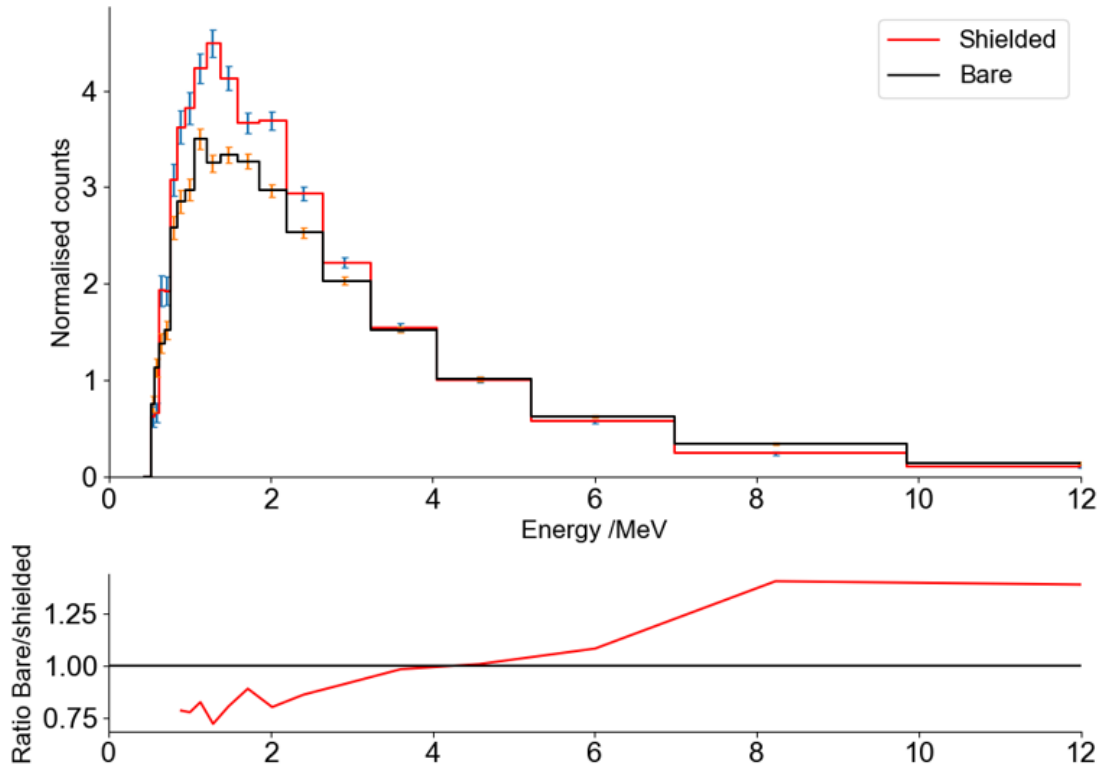


Figure 85: Comparison of results of measurements with shielding over the detectors and without. Plot of the ratio of the two measurements are shown in the smaller plot below. Both plots normalised to unity at 3.84.

The results of measurements with different PSD settings are shown in Figure 86. In this dataset, the high-energy responses are consistent within statistical variation. There is a noticeably lower response at the low-energy edge of the spectrum.

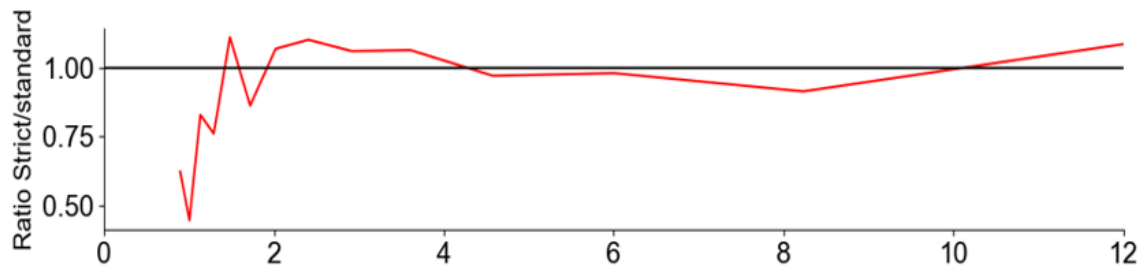
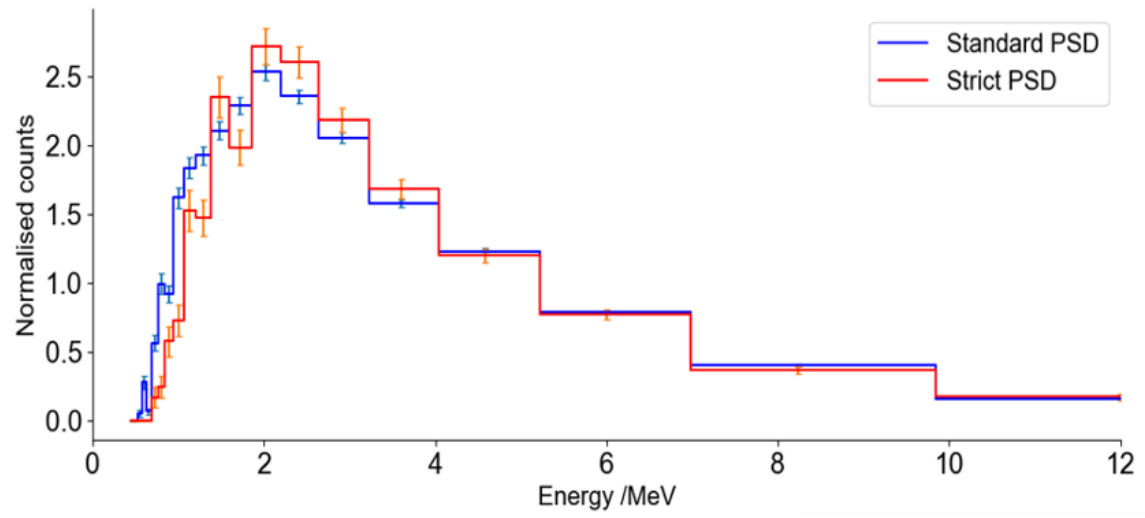


Figure 86: Comparison of results of measurement with varying PSD settings, ratio of the two plotted on subplot underneath.

5 DISCUSSION

As explained in the introduction to this thesis, this research was instigated with the goal of investigating the use of neutron time of flight measurement in a security context. Specifically, the aims of the research were to:

- Miniaturise the hardware associated with performing associated particle TOF spectroscopy.
- Perform TOF spectroscopy in real time.
- Measure the prompt fission neutron energy spectrum of ^{244}Cm and ^{252}Cf .
- Evaluate the ability of the system to discriminate or identify the nuclide under observation.

In the following section the findings of this research and the extent to which these aims have been accomplished will be discussed.

5.1 INITIAL FINDINGS AND VERIFICATION OF THE TOF SPECTROMETER

In section 4.1 (page 101) the first measurements of the Lancaster source using the modified Hybrid systems MFA were presented. These initial measurements verify the operation of the system and the functioning of the coincidence pairing.

The system functions as expected, with a flat rate of background count, a sharp gamma peak, and a distribution of correlated neutron events. As can be seen in these first measurements, the shape of the measured spectrum agrees with the shape of the known Watt spectrum for ^{252}Cf at high energies, once the adjustments for energy bin width and background counts have been made. The discrepancies between the measured results and the watt spectrum at this stage are generally attributed to the effect of detector efficiency on the operation of the system.

Of particular interest with these measurements is the ability to record coincident events of multiple particle scenarios. As was observed by summing the different event combinations, the predominant event type was γ - γ

coincidences reflecting the higher gamma multiplicity value in fission, relative to the neutron multiplicity. The counts of n-n, γ -n and n- γ coincidences are similar, but with a slight preference for n-n events. It is not known definitively why there is an equal or greater number of n-n events to either n- γ or γ -n, since γ multiplicities should increase the probability of the latter two scenarios, but it is possibly because the n-n category primarily contains neutron scatter events rather than multiplets of coincident particles.

When comparing the energy spectra computed from the TOF distributions of n-n and γ -n coincidences, shown in Figure 65 (page 104), it can be seen that the shape of each spectrum is in agreement with the Watt spectrum above 2.5 MeV. The data collected from n-n coincidences show a noticeably higher number of counts in the upper bins, representing neutrons above 5 MeV, than would be expected from the Watt distribution when it is normalised across the spectrum. Again, it is not known definitively why this is, but it is speculated that the mechanism of detection (neutron scatter between the detectors) favours high energy neutrons. This can be explained via the kinematics of the scatter reaction; the detectors are placed with an associated scatter angle of 45° , which equates to an energy loss of half the neutron's initial energy within a scatter event (assuming scatter off a proton in the scintillant.) The requirement for a scatter before the final detection lowers the neutron's energy, making it more likely that it will not reach the low energy cut off in the second detector, giving a lower detection efficiency for low energy neutrons.

The primary reason for focusing on γ -n coincidences in subsequent measurements is the reduced uncertainty associated with the coincidence mechanism. As shown in Figure 40, (page 67) the uncertainty in the energy domain regarding where the neutron is detected within the scintillator volume must be accounted for twice in a neutron scatter event, along with the uncertainty on the angle that the neutron will have scattered through. Furthermore, fission-correlated neutrons detected in coincidence cannot be removed from those consisting of neutron scatter using the PSD function of the MFA which will further complicate the spectrum. These geometric uncertainties are reduced when using γ -n events, as there is only one neutron

detection, and the use of PSD filtering of particles greatly reduces the number of fission-correlated neutrons included in the spectrum. Reduced uncertainty is an advantage when attempting to compare very similar spectra, such as those produced by fissioning nuclides.

The ability to measure n-n events is not however completely redundant. The use of associated particle TOF methods have been reported using start signalling based on gamma rays produced at the moment of (α ,n) reactions in AmBe sources. [116] [126] The energetics of the ${}^9\text{Be}(\alpha,n)$ reaction mean that 40% of the neutrons produced are not produced with a correlated gamma ray. This leads to an incomplete fast neutron spectrum, with neutrons above approximately 7 MeV missing. Having the option to measure n-n scatter events and accounting for the energy lost in the scatter event would potentially allow the full spectrum to be measured, giving the technique utility in measuring (α ,n) spectra, or those without associated gamma rays. Indeed, examining the capabilities of n-n mode would make for valuable further work.

5.2 NPL BARE ${}^{252}\text{Cf}$ SOURCE MEASUREMENTS

Section 4.4.1 (page 113) presented the results of the measurement of a bare ${}^{252}\text{Cf}$ source, taken at NPL. The differences between the spectra taken from bare and water stored sources shall be discussed in the following section (5.6.1.1).

The bare ${}^{252}\text{Cf}$ source measurement was made with the threshold settings on the MFA still at 100, and so exhibits a much higher low energy cut off than that would be expected from the efficiency of the scintillator. As in the Lancaster measurements however, this appears to primarily affect the low energy end of the spectrum. As the efficiency curve of EJ-309 peaks close to the low energy cut off, and then drops very linearly and slowly, the shape above the low energy cut off is preserved relatively well, with little improvement to the agreement between the curve and the data.

Adjusting the fit of the interpolation of the efficiency curve to match the low energy threshold of the measured californium data however renders a good fit to the data across the full energy range of measurements, as shown

in Figure 76 (page 116). Whilst there is good agreement across most of the measured data, it appears that the high energy bins of the spectrum are somewhat higher than expected. This finding is similar to the findings of Becchetti [118] and Blain [119], who have also measured the ^{252}Cf spectrum via gamma tagged, and both exhibit counts greater than predicted in the energy bins above 5 MeV.

An attempt was made to fit Watt and Maxwellian spectra using a least squares fitting procedure, but as the primary shaping factor of these fits is the average neutron energy, and this part of the spectrum falls below the low energy cut off of the detector system, the fitting procedure would not fit to any parameters that were reasonable considering the a priori knowledge of the source. Additionally, the high energy bins, which are believed to be overestimated, form a large enough proportion of the data that they can affect the fit considerably. As stated above however, the measurements show good agreement with the reference spectrum for ^{252}Cf when plotted and normalised together.

5.3 CURIUM MEASUREMENTS

There are few examples of curium fission spectra in the literature. This stands in stark contrast with that of ^{252}Cf , which, as a commonly used neutron source, has been studied in depth, mainly due to its abundance as a neutron source and its use as a reference spectrum.

In this research the PFNS of ^{244}Cm was deterministically measured using a pair of EJ-309 liquid scintillators in a prompt gamma triggered TOF mode. A far greater proportion of the high energy edge of the spectrum, was measured for ^{244}Cm compared to ^{252}Cf , allowing a Maxwellian fit to be made. The measured data were fitted to a Maxwellian spectrum with a parameter T , of 1.33 (± 0.07) MeV and the Watt spectrum with parameters of $a=0.918$ and $b=1.151$. This is in agreement with previous measurements, taken using various experimental setups.

The ^{244}Cm spectra that can be found in the literature are fairly dated. Three references to curium measurements made in the late 60s-early 70s

were made in the work of Aleksandrova et al [127], and a review of nuclear data undertaken in 1996 again references these works and made the case for these values to be remeasured with modern techniques. Also decried in the 1996 review was the lack of detail in earlier work on the exact nature of the measurements, and how and to what extent uncertainties in the data were quantified. [128]

The most recent measurements of the ^{244}Cm spectrum appear to be those of Batenkov et al. [129] made in 1997. These measurements were made with a foil deposited source housed in an ionisation chamber fission detector. Several neutron detectors were used which allowed a greater energy range to be studied than in this research. Further to measured values, unreferenced and somewhat contradictory mentions of Maxwellian and Watt parameters have been found, primarily in manuals to modelling applications. It is believed that these values are obtained by modelling the spectrum as a function of fission fragment distributions, and the measured neutron multiplicity. [24] [130] [6]

An additional aspect of the older ^{244}Cm data is that it is generally expressed in terms of the single parameter of the Maxwellian distribution. Table 6 shows the results of various legacy measurements of the ^{244}Cm spectrum, along with that made in this research.

Table 6: Maxwellian and Watt distributions from various sources.

<u>Energy range</u> <u>MeV⁻¹</u>	<u>Maxwell parameter T</u> <u>MeV</u>			<u>Method of measurement</u>	<u>Reference</u>	<u>Date</u>
2-15MeV	1.33 ± 0.07			γ triggered TOF	This work	2019
0.3-7	1.37 ± 0.03			TOF	[127] (Belov)	1969
0.5-6	1.455 ± 0.062 (extrapolated from average energy)			³ He spectrometer	[127] Herold	1972
0.5-6	1.38 ± 0.03			TOF	[131] Zamyatnin	1969
2-14	1.33 ± 0.03			Stilbene scintillator	[127] Aleksandrov	1974
-	1.5			-	[6]	1981
0.1 -15	1.37 ± 0.02			Fission chamber TOF	[129]	1997
	Watt Parameters					
	Number in graph	a	b			
-	1	0.906	3.720	-	[24]	2007
-	2	1.108	3.848	-	[130]	2003
2-15MeV	1.33 ± 0.07	γ triggered TOF	This work	2019		

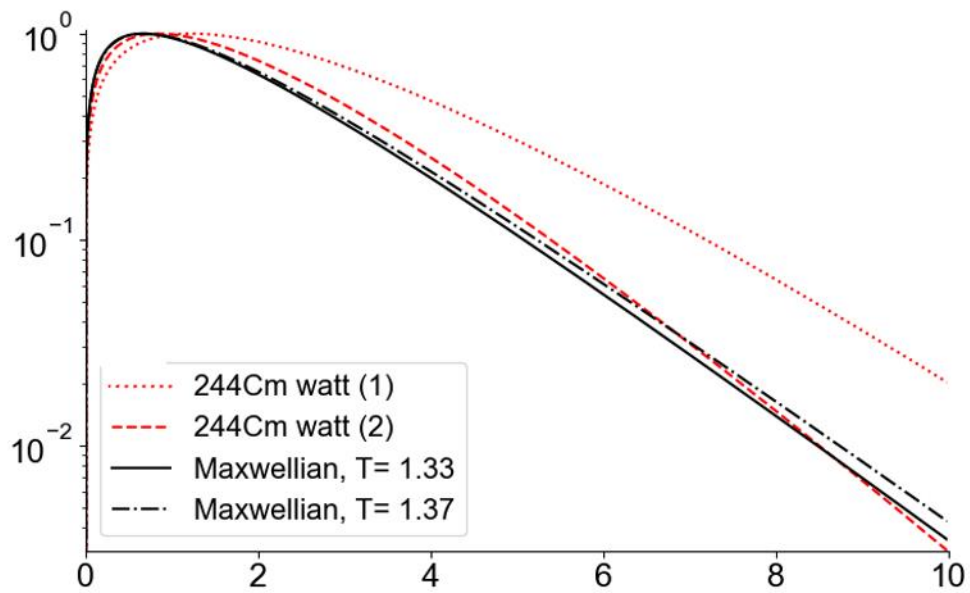


Figure 87: Watt and Maxwellian spectra for ^{244}Cm plotted using parameters listed in Table 6

Figure 87 shows Watt and Maxwellian spectra plotted using the parameters listed in Table 6. This research supports a Maxwellian parameter of 1.33, which corroborates that measured by Aleksandrov [127], but within uncertainties the result is consistent with the findings of Batenkov [129] in the most recent (1996) measurements.

A limitation of the measurements made in this research is the low counting statistics and subsequent uncertainty associated with the parameter found by the Maxwellian fit. A Monte-Carlo uncertainty analysis procedure suggests uncertainties of ± 0.07 , which are higher than those reported in the older measurements listed in Table 6, although it should be noted that the nature of the reported uncertainties and their reliability has been questioned in several review sources. The source of the increased uncertainties in these measurements is mainly due to counting statistics, as counting time was limited by source availability rather than data requirements. An additional factor is the resolution of the measurements, 4ns timing resolution in this research in comparison with around 1ns reported in the literature. The operation of the FPGA is the limiting factor on the timing resolution, governed by the clock cycle (4ns). This resolution limit reduces the number of data

available, particularly at the high energy end of the spectrum. Subsequent measurements with a stronger source or for longer period would reduce these uncertainties. Additionally, there is the geometric uncertainties associated with the detector size, the detectors used in this research had dimensions of 10cm, those used by Batenkov to obtain TOF measurements report a geometric uncertainty of 5mm.

Despite these limitations, the uncertainties are small enough that the Maxwellian parameter can be measured with a resolution comparable to the differences between nuclides. Most importantly in a source discrimination context, this result suggests that the fission spectrum can be measured to a precision that allows discrimination between ^{244}Cm and ^{252}Cf . The generally accepted Maxwellian parameter for ^{252}Cf , 1.42, renders a harder spectrum than that of ^{244}Cm . This is reflected in the measurements of ^{252}Cf sources made during this research; whilst the small range of energies that the spectra are measured over precludes the fitting of fission curves, the californium measurements in all cases suggest a measurably harder spectrum than that of curium. Figure 88 shows the measurements of ^{252}Cf and ^{244}Cm taken at NPL (section 4.4.1, page 113) and PSC (section 4.4.2, page 117) on the same axis, alongside Maxwellian spectra plotted using the parameters reported by Aleksandrov, folded with the detector efficiency for the measurements made in this work. All data is normalised to 1 in the first bin.

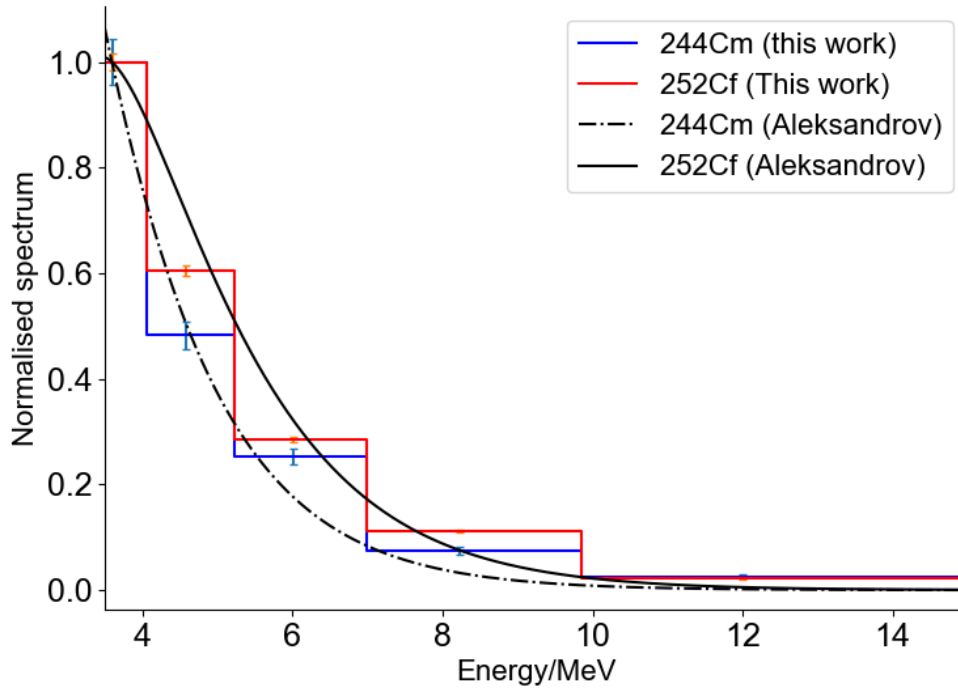


Figure 88: Comparison of ^{252}Cf and ^{244}Cm data. Normalised to area under the curve.

This compares well with the measurements made by Aleksandrov, who made measurements of ^{252}Cf , ^{244}Cm , and ^{240}Pu under identical conditions, using pulse height data from a variety of detectors. This is a particularly encouraging result, as being able to discriminate ^{240}Pu from ^{244}Cm or ^{252}Cf is a useful asset from a security context. The Maxwellian spectra determined by the measurements of Aleksandrova are plotted on Figure 89.

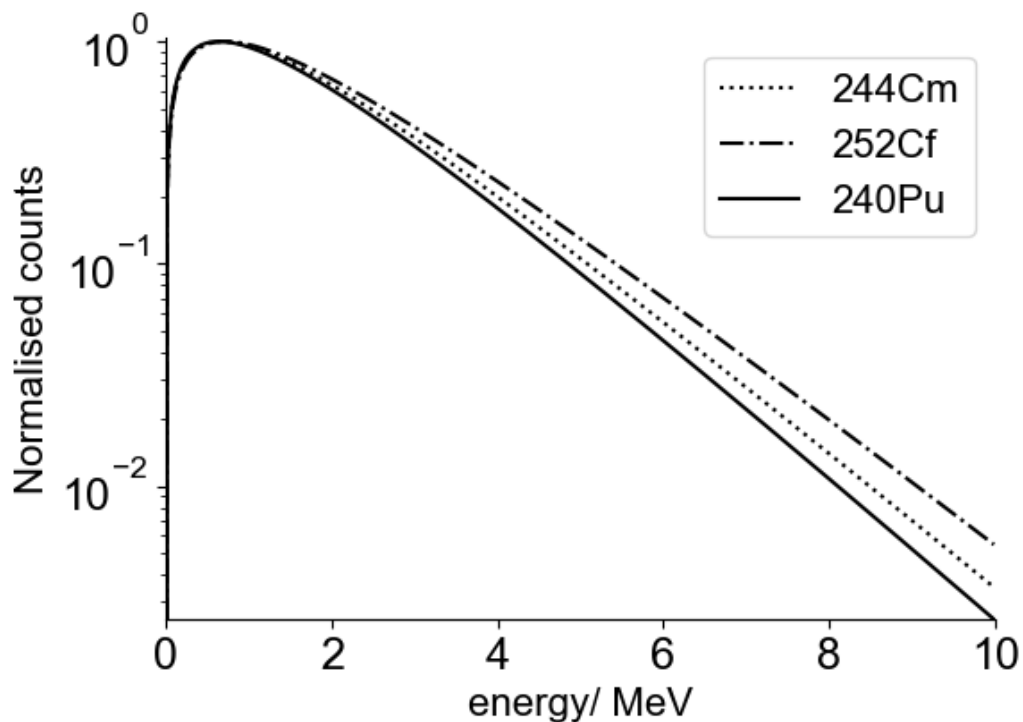


Figure 89: Maxwellian spectra using parameters measured by Aleksandrova et al [127]. Plotted are spectra for ^{252}Cf (1.42), ^{244}Cm (1.33), ^{240}Pu (1.26).

5.4 SIMULTANEOUS ^{244}Cm AND ^{252}Cf MEASUREMENTS

Section 4.4.3 (page 119) shows the results of the small separation TOF measurements of ^{252}Cf and ^{244}Cm taken under identical conditions. As can be seen in the measurements there is significant separation between the two nuclides in the high energy region of the spectrum. At the peak of the spectra the two datasets are indistinguishable within uncertainties, unfortunately the low activity of the two sources prevented the collection of enough counts to adequately show any separation around the peak.

The counts at the high energy end of the spectrum were higher than expected. As explained in the results section, it was thought that this could have been a manifestation of the multiplicity of the two nuclides. Subsequent measurements with polyethylene however have suggested that this is not the sole reason for this result.

It is not entirely clear why there is such a strong signal from the high energy end of the spectrum. It does however appear to affect both of the nuclides under investigation. It is possible there is an unforeseen component of the efficiency of the overall system which favours the detection of high energy neutrons, such as a correlation between the gamma energy and that of high energy prompt neutrons. Alternatively, this could be a systematic error born of the assumption that prompt neutrons and prompt gamma rays are produced at exactly the same moment. The majority of investigations into prompt gamma rays have focused on those emitted within 10ns of fission, although there is evidence that some take longer to materialise. [132] At short flight times, even small delays in the gamma emission times would lead to an overestimation of the neutron energy, resulting in overpopulation of the high energy bins. This speculation however cannot be confirmed by the measurements made here and would need to be developed via further research.

There remains however a separation in the spectra measured from the two nuclides, supporting the hypothesis that the ^{252}Cf spectrum is measurably harder than that of ^{244}Cm , when measured via a TOF approach [127].

5.5 NPL EFFICIENCY MEASUREMENTS

Section 4.2 (page 105) shows the results of the efficiency measurements on the detector system. The primary motivation for this work was the need to understand the system response to low energy neutrons.

Few detector characterisations reported in the literature are accompanied by efficiency data. Response measurements are typically used to determine the light output curve and detector resolution functions of a detector, with the efficiency of the detector accounted for during subsequent modelling. This focus on the light output is driven by the requirement of pulse height spectrum unfolding applications, as described in the background section on page 29. Standalone efficiency data are seldom reported, this is partially due to the fact that both the low energy cut off and absolute efficiency

of a detector have a strong dependence on the threshold settings of the data acquisition hardware, and partially because the effect of efficiency is accounted for during detector modelling, without specific input from the user. Where efficiency values are reported, it is usually as part of a detector characterisation utilising TOF methods, most recently reflected in the work of Pino [13] and Kornilov [52].

Knowledge of the detector efficiency and the low energy cut off is vital when interpreting the data provided by TOF systems, as can be seen in the early results presented in this thesis, where the efficiency curves must be accounted for before the measurements will fit the reference spectra, particularly at the lower energy regions. The Pino data mentioned above incorporates measured data, measured using a TOF setup similar to that used in this research, compared with modelled results produced by MCNPX and GEANT4 and was found to be adequate for use in this work. Fitting the Pino efficiency curves to the low energy threshold measurements gives an efficiency curve which can be used with this TOF setup. Performing the low energy measurements was also valuable in verifying the low energy cut off associated with the EJ-309 scintillant, as the Pino data reports uncertainties of around 5%, and at low threshold settings measurements do not cover the whole energy range over which the scintillator is sensitive, with the point of the response cut off interpolated via modelling.

The results of the low energy cut off measurements were somewhat surprising, as it was expected that the efficiency response would drop linearly with decreasing energy. If this were the case, then based on the measurements at 1 and 0.85 MeV, the final 0.7 MeV measurement should have been below the cut off. The presence of neutrons in this measurement was somewhat unexpected. Examination of the modelled efficiency curves at higher thresholds however indicated the presence of this effect. Furthermore, comparing with other modelled data (from the TOF experiments described by Becchetti [118], albeit EJ-200, a plastic scintillator, but still based on proton recoil) exhibits the same feature, suggesting that it is physical component of the efficiency spectrum.

The fitting of the efficiency data to the lognormal curve as shown in Figure 70, provided a convenient method of using the Pino data in this research. The use of a curve as shown here was also an effective way of applying the data to a continuous curve such as the Watt spectrum, allowing it to maintain its shape without distortion produced by interpolation of modelled or measured point data.

Folding the efficiency into the reference data for comparison with the measured data has proved a good way of comparing the measurements with the expected Watt spectrum. The technique is inspired by the work of Becchetti et al [118]. It is preferable to directly correcting the measurements for efficiency as it avoids producing unphysically high counts where the efficiency gets close to zero and simplifies the error propagation process.

5.5.1 Absolute system efficiency

Until now, only the detection efficiency of a single detector has been considered. By the nature of the detection mechanism, i.e. a gamma ray must be detected in coincidence with a neutron, the absolute detection efficiency of the system will be a convolution of the detector efficiencies with respect to energy for both gamma rays and neutrons. Pino has also reported values for the gamma efficiency alongside the measurements for neutron detection efficiency. Compared to the response for neutrons, the gamma efficiency is relatively flat at the energies encountered from fission [54].

This research has not attempted to establish the overall efficiency of the system, rather it has relied on the fact that as the energy spectrum of prompt fission gamma rays is stochastic with respect to neutron energy [133], The shape of the measured spectrum remains dependent only on the neutron efficiency curves, and is not dependent on the gamma ray efficiency. As future work however, establishing the gamma ray efficiency and the geometric efficiency of the system could prove a means of measuring the rate of fission, independently of the overall radioactivity of the source.

5.6 PARAMETER STUDY

Both the effect of the surroundings of the source and the parameters used to setup the equipment has a direct bearing on the measurements obtained. This aspect of performing TOF measurements has not been reported in the literature but has been briefly investigated during this research using the Lancaster californium source.

5.6.1.1 Effect of the water tank and scatter

The experiments performed using the Lancaster source suggest that surroundings of the source and the water-tank has a strong influence on the measured spectrum. As can be seen in direct comparison with the NPL bare californium, source shown in Figure 74 (page 114), the low energy end of the spectrum is extended to below the threshold of the detector, and the high energy bins of the spectrum also increase in size relative to the normalisation point.

This effect can be explained in terms of the scatter around the source; neutrons scattered off the surroundings will have a longer flight path and therefore a longer time of flight, as shown in Figure 90 hence they will be mistaken for lower energy neutrons. This also explains the apparent lowering of the low energy threshold of the detector; whilst the TOF may suggest that a neutron has low energy, in reality it will merely have had a longer flight path,

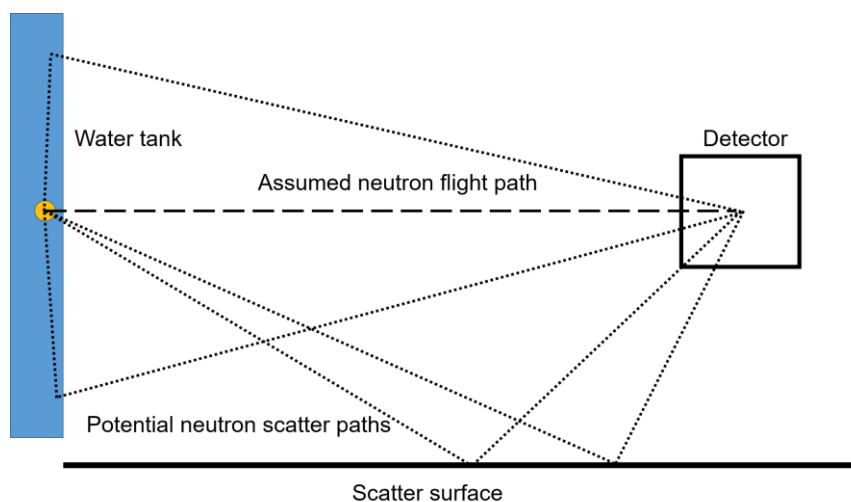


Figure 90: Illustration of scatter off the water tank and source surroundings. The longer path of neutrons scattered into the detector are illustrated.

but still be energetic enough to produce a scintillation pulse greater than the threshold of the detector.

5.6.2 The effect of photomultiplier voltage on efficiency

Figure 84 (page 124), shows energy spectra produced using a ^{252}Cf source, and the TOF system with three different negative high voltage levels supplying the detectors. The effect of varying the high voltage can be seen clearly, the energy threshold lowering as voltage is increased. This can be understood as a manifestation of the increasing photomultiplier tube gain with the supply voltage. As the gain is made larger, decreasingly small scintillation pulses are able to trigger the pulse acquisition process, and therefore the overall detection efficiency is increased. The effect is largely the same as that of changing the threshold on the MFA.

Whilst this is a fairly intuitive finding, it highlights the need to keep equipment consistent between measurements, as the effect of the changing efficiency can easily match or exceed that of the small differences in different fission neutron spectra.

5.6.3 The effect of PSD settings on the measurement

Altering the PSD settings of the system seems to have a small effect on the measured data, mostly altering the low energy end of the spectrum. As can be seen, the application of a stricter PSD setting raises the low energy threshold and heightens the peak at the most probable energy. The high energy response is largely unchanged. These effects can be understood in terms of the system artificially removing true events; strict PSD not only removes a number of false counts but will also increase the number of true counts rejected. As the area of greatest ambiguity in particle identification is around low amplitude pulses, the application of strict PSD disproportionately effects low energy events.

From this finding it can be seen that, in the neutron detector at least, it is better to leave the PSD at a less strict setting, relying on the timing information to remove erroneous gamma coincidences. A reasonable amount of particle discrimination fidelity must be maintained in the gamma trigger

however, as falsely classified neutrons cannot be sifted out of the measurements in such a simple manner.

5.7 IMPLICATIONS FOR ISOTOPIC DISCRIMINATION IN A SECURITY

CONTEXT

The results of this research demonstrate the ability to measure the fission spectrum and fit it to a Maxwellian distribution, using just a pair of organic scintillators, without an external trigger. Whilst evidence for the discrimination of ^{252}Cf and ^{244}Cm has been examined, there are many other nuclides that are of interest from a security standpoint.

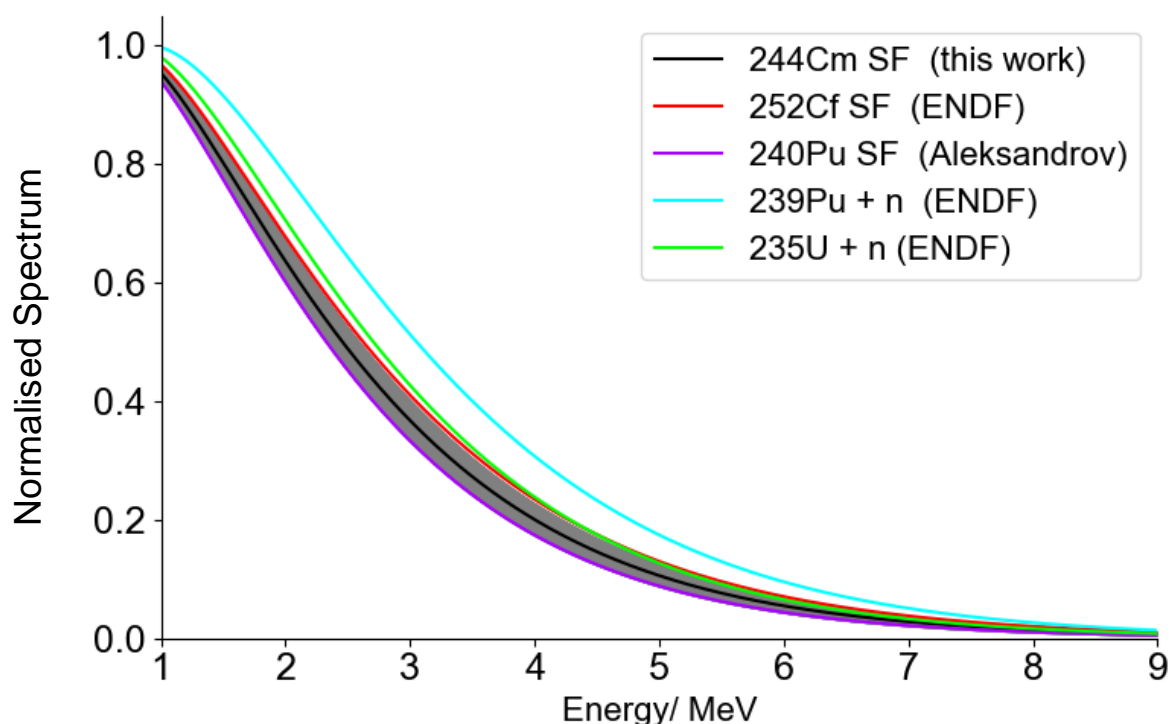


Figure 91: Induced and spontaneous fission spectra for $^{235}\text{U}(n_{\text{thermal}}, \text{fission})$, $^{239}\text{Pu}(n_{\text{thermal}}, \text{fission})$ and ^{240}Pu , ^{244}Cm and ^{252}Cf spontaneous fission. Spectra for ^{235}U and ^{239}P are taken from ENDF/B V library. ^{252}Cf and ^{240}Pu are Maxwellian distributions from [127], and ^{244}Cm is from this research. The grey area shows the one sigma uncertainty on the ^{244}Cm measurements.

As explained earlier in this thesis, there is great value in the ability to discriminate the neutron spectra of fissile materials such as ^{235}U and ^{239}Pu from those indicating spent nuclear fuel such as ^{244}Cm , or ^{240}Pu , and from

those that may have come from a university or industrial source such as AmBe or ^{252}Cf .

On the most basic level this research has demonstrated the ability to measure the fission spectrum simply and easily, suggesting that TOF measurements would be able to discriminate between fission sources and (α,n) sources. As mentioned earlier, some interesting further work would be to take measurements of an AmBe source, as the literature suggests that the spectrum measured would be significantly different in shape to that of a fission source [12].

The discrimination of neutron spectra of fission sources is difficult due to the similarity of their distributions. Figure 91 shows reference spectra for the thermally induced fission of ^{235}U and ^{239}Pu , such as may be produced by SNM under interrogation by the neutron spectrum of a thermalised AmLi source. Alongside those spectra are those of the spontaneous fission of ^{240}Pu , ^{244}Cm and ^{252}Cf . Also shown on the plot is the uncertainty associated with the Maxwellian fit to the data taken in this work (dotted lines).

As can be seen from the plot, due to the closeness of the curves, combined with the uncertainty associated with the measurements, it would be difficult to confidently discriminate between the different spectra on the basis of the measurements presented in this thesis. As previously discussed, as the uncertainties are mainly due to lower counting statistics, it is reasonable to expect that they could be reduced with further counts. Similar TOF setups [127] in the literature have reported data fitted with Maxwellian spectra with uncertainties on the T value as low as ± 0.03 , at which point discrimination is more feasible. Performing the uncertainty analysis on the basis of an identical dataset, but with more counts, running the measurements for 4 times the amount of time would reduce the uncertainties to ± 0.03 . The same end can be also be achieved via a source 4 times as active, or by moving the detectors closer to improve geometric efficiency.

A final matter, complicating efforts to identify nuclides based on their prompt neutron energy spectrum, is the uncertainty surrounding reference spectra available in the literature. [134] There is a constant effort to update

nuclear data, and whilst some spectra, such as that of ^{252}Cf , are well characterised, for many nuclides measurements of the fission spectrum are still subject to inconsistency.

6 CONCLUSIONS OF THIS RESEARCH

Time of flight spectroscopy has long been used to measure the neutron energy spectrum as it is the only way of obtaining a deterministic measurement of neutron energy. There have been several ways this has been achieved in the past, often requiring specialised instrumentation, source preparation and equipment and only recently has it been a technique that can be used in a more general sense.

This research has outlined the development of TOF neutron spectroscopy system, allowing this technique to be performed in a real time, and using small scale, portable hardware, using two EJ-309 scintillators, without any external trigger. Furthermore, it has investigated the ability of the TOF system to discriminate between nuclides. This ability to identify and characterise neutron spectra is desirable in a range of security and safeguards contexts and is particularly difficult given the similarity of the neutron spectra produced by different sources, and the challenge typically associated with measuring them. On the basis of the data collected, it can be established that there is scope to discriminate between ^{244}Cm and ^{252}Cf , and the spectra can be fitted Maxwellian spectrum, giving insight to its identity when compared with known fission spectra. Extrapolating out, this finding suggests that the discrimination of other fission sources, particularly those of ^{235}U and ^{239}Pu , is feasible.

The ^{244}Cm spectrum itself is of interest in a number of applications, particularly in the characterisation of spent nuclear fuel but has been subject to uncertainty. It has been some time since it has been measured and this work adds to and advances knowledge of this spectrum. The lack of information characterising fission spectra has not only affected ^{244}Cm , and this simple method for deterministically measuring fission spectra is a demonstration of a potential method of increasing the body of knowledge on fission spectra in general.

This technique is not completely immune to some of the subtleties associated with all methods of measuring the neutron energy spectrum;

understanding the detector efficiency is an important aspect of making any measurements and is particularly relevant here. It was found that efficiency data in the literature can be used in this case as long as it is adjusted to represent the detector and settings in use, and for this purpose efficiency measurements have been made to establish the low energy cut off of the detector.

An investigation into the effect of the source environment and the set-up of the system has found that the measured spectrum is sensitive to small changes in the surroundings and measurement parameters. Those measuring spectra with a TOF system based on liquid scintillators must take great care that the system efficiency is not affected by small changes in the detector thresholds, the detector voltages, and the geometry of the time of flight arrangement. The shape of the measured spectrum is highly dependent on these factors and small changes can easily overshadow the subtle differences in spectrum that are under investigation.

6.1 FUTURE WORK

There are several areas of interesting further work that could follow on from this research, particularly now that the operation and response of the system is better understood given the findings of this work.

An obvious next step is to use the system to measure more examples of fission spectra. As stated above, ^{244}Cm and ^{252}Cf can be discriminated on the basis of their spectra, and there are other fission sources with similar or greater separation in their fission sources. It would be valuable work to measure more fission nuclides, to further demonstrate the discriminative ability of the system. In addition to demonstrating the power to discriminate nuclides, this would add to the body of knowledge of fission sources in general.

As part of this effort to characterise fission spectra, a logical development from measuring spontaneous fission sources would be to extend the application of the system to stimulated fission spectra. Whilst nuclides which can be induced to fission, such as ^{235}U and ^{239}Pu are harder to access,

evaluating the response of the TOF system to their spectra would enhance its utility in a security context. Whilst the known spectra taken from the ENDF library (Figure 91, page 142) suggested that the spectra have a greater separation from the nuclides measured in this work, and may be more easily identified, there would be the additional challenge of the obscuration factor of the stimulation spectrum. Additional research could examine strategies for minimising this signature, whilst obtaining the maximum amount of information about the source under interrogation.

This research has focused on γ -n events. It would extend the utility of the system to further examine n-n scatter events, as this would open up opportunities to measure the spectrum of neutron sources without associated particles, the full energy range of the commonly used AmBe source for example cannot be measure using only γ -n coincidences. Accounting for scatter and the effect of the efficiency of two detectors on the system response would allow these spectra to be measured.

Finally, there is a large amount of work that could be done to further develop the hardware of the system. Finer timing resolution, the inclusion of more detectors and the accounting for pulse height as well as pulse timing would either improve the measurements which can already be made with this setup or open up more capabilities of the system.

6.2 FINAL WORDS

In conclusion, there are several achievements and findings that this research has accomplished:

- It has been demonstrated that the fast neutron energy spectrum of a fission source can be measured in real time using two EJ-309 scintillator detectors and a single, FPGA-based data acquisition system. A choice of n-n or γ -n events can be used.
- The time interval distribution is distinct between different fission radionuclides when measured under identical conditions. Fitting to the known spectrum parameters is possible with enough precision to suggest differentiation between fission sources is feasible.

- The response of the system is highly dependent on the settings of the data acquisition process, and the voltage applied to the photomultiplier tubes of the detector. This is a reflection of the probability behind event detection and the effect the aforementioned parameters have on the efficiency of the detectors across the energy range.
- Measurements of the ^{244}Cm spectrum are in broad agreement with the relatively sparse amount of prior data and add to the body of knowledge of this spectrum.

The novelty of this system lies in the simple, portable and real time nature of the TOF system and its ability to measure fission spectra to a degree where discrimination is possible. In addition, the measurements made with the new system advance the knowledge available on the long unexplored ^{244}Cm prompt fission spectrum.

7 REFERENCES

- [1] J. Chadwick, "The Existence of a Neutron," *Proc. R. Soc. London. Ser. A*, vol. 136, no. 830, pp. 692-708, 1932.
- [2] W. Bowen, M. Cottee, C. Hobbs, L. Lentini, M. Moran and S. Tzinieris, "9/11 and Beyond," in *Nuclear Security Briefing Book*, London, Kings college London, 2019, p. 35.
- [3] H. R. Vega-Carrillo and S. A. Martinez-Ovalle, "Neutron spectra and dosimetric features of Isotopic neutron sources: A review," in *Int. Symp. Solid State Dosimetry*, Leon, Mexico, 2015.
- [4] R. T. Kouzes, J. H. Ely, L. E. Erikson, W. J. Kernan, A. T. Lintereur, E. R. Siciliano, D. L. Stephens, D. C. Stromswold, R. M. V. Ginhoven and M. L. Woodring, "Neutron detection alternatives to ^3He for national security applications,," *Nucl. Instrum. Methods Phys. Res. A*, vol. 623, no. 3, pp. 1035-1045, 2010.
- [5] R. T. Kouzes, E. R. Siciliano, J. H. Ely, P. E. Keller and R. J. McConn, "Passive neutron detection for interdiction of nuclear material at borders," *Nucl. Instrum. Methods Phys. Res. A*, vol. 584, no. 2-3, pp. 383-400, 2008.
- [6] P. M. Rinard, G. E. Bosler and J. R. Phillips, "Calculated neutron source spectra from selected irradiated PWR fuel assemblies," Los Alamos National Laboratory, Los Alamos, NM Tech. Rep. LA-9125-LS, 1981.
- [7] J. L. Szabo and L. J. Boutaine, "Some Examples of Industrial Uses of Neutron Sources," *Radiat. Prot. Dosim.*, vol. 70, no. 1-4, pp. 193-196, 1997.
- [8] M. J. Joyce, M. Aspinall, B. D'Mellow and R. O. Mackin, "Digital discrimination of neutrons and γ -rays in liquid scintillators using pulse

- gradient analysis.," *Nucl. Instrum. Methods Phys. Res. A*, vol. 578, no. 1, pp. 191-197, 2007.
- [9] J. S. Beaumont, B. A. Shippen, M. P. Mellor and M. J. Joyce, "Imaging of fast neutrons and gamma rays from ^{252}Cf in a heavily shielded environment," *Nucl. Instrum. Methods Phys. Res. A*, vol. 847, pp. 77-85, 2017.
- [10] M. J. Joyce, S. Agar, M. D. Aspinall, J. S. Beaumont, E. Colley, M. Colling, J. Dykes, P. Kardasopoulos and K. Mitton, "Fast neutron tomography with real-time pulse-shape discrimination in organic scintillation detectors," *Nucl. Instrum. Methods Phys. Res. A*, vol. 834, pp. 36-45, 2016.
- [11] J. Iwanowska, L. Swiderski, T. Krakowski, M. Moszynski, T. Szczesniak and G. Pausch, "The time-of-flight method for characterizing the neutron response of liquid organic scintillators," *Nucl. Instrum. Methods Phys. Res. A*, vol. 781, pp. 44-49, 2015.
- [12] J. Scherzinger, R. A. Jebali, J. Annand, A. Bala, K. Fissum, R. Hall-Wilton, D. Hamilton, N. Mauritzson, F. Messi, H. Perrey and E. Rofors, "Tagging fast neutrons from a ^{252}Cf fission-fragment source," *Appl. Radiat. Isot.*, vol. 128, pp. 270-274, 2017.
- [13] F. Pino, L. Stevanto, D. Cester, G. Nebbia, L. Sajo-Bohus and G. Viesti, "The Light output and the detection efficiency of the liquid scintillator EJ-309," *Applied Radiation and Isotopes*, vol. 89, pp. 79-94, 2014.
- [14] L. Berge, O. Litaize, O. Serot, C. D. S. Jean, P. Archier and Y. Penelieu, "Study on Prompt Fission Neutron Spectra and Associated Covariances for $^{235}\text{U}(\text{nth},\text{f})$ and $^{239}\text{Pu}(\text{nth},\text{f})$," in *Physics Procedia*, 2015.
- [15] W. Mannhart, "Evaluation of the ^{252}Cf Fission Neutron Spectrum between 0MeV and 20MeV," IAEA, Braunschweig (Germany, F.R.) Tech. Rep. IAEA-TECDOC--410, 1986.

- [16] M. Schulc, M. Košťál, E. Novák, R. Kubín and J. Šimon, "Application of ^{252}Cf neutron source for precise nuclear data experiments," *Appl. Radiat. Isot.*, vol. 151, pp. 187-195, 2019.
- [17] A. T. Yue, M. S. Dewey, D. M. Gilliam, G. L. Greene, A. B. Laptev, J. S. Nico, W. M. Snow and F. E. Wietfeldt, "Improved Determination of the Neutron Lifetime," *Phys. Rev. Lett.*, vol. 111, no. 22, 2013.
- [18] A. P. Serebrov, V. E. Varlamov, A. G. Kharitonov, A. K. Fomin, Y. N. Pokotilovski, P. Geltenbort, I. A. Krasnoschekova, M. S. Lasakov, R. R. Taldaev and A. V. Vassiljev, "Neutron lifetime measurements using gravitationally trapped ultracold neutrons," *Phys. Lett. B*, vol. 78, no. 1-2, pp. 72-78, 2005.
- [19] G. F. Knoll, "Sources of Background Radiation," in *Radiation detection and measurement*, Hoboken, NJ, USA, Wiley, 2000, p. 757.
- [20] Z. Hu, L. Ge, J. Sun, Y. Zhang, Z. Cui, G. Gorini, H. Zhang, J. Chen, J. Chen, X. Li and T. Fan, "Measurements of cosmic ray induced background neutrons near the ground using a Bonner sphere spectrometer," *Nucl. Instrum. Methods Phys. Res. A*, vol. 940, pp. 78-82, 2019.
- [21] T. Vasilopoulou, I. Stamatelatos, P. Batistoni, A. Colangeli, D. Flammini, N. Fonnesu, S. Loreti, B. Obryk, M. Pillon and R. Villari, "Improved neutron activation dosimetry for fusion," *Fusion Engineering and Design*, vol. 139, pp. 109-114, 2019.
- [22] L. Meitner and O. R. Frisch, "Disintegration of Uranium by Neutrons: A New Type of Nuclear Reaction," *Nature*, vol. 143, no. 3615, pp. 239 - 240, 1939.
- [23] E. N., "The Origin of Neutron Radiation," Los Alamos National Laboratory, Los Alamos, NM Tech. Rep. LA-UR-90-732, 1991.

- [24] J. Verbeke, C. Hagmann and D. M. Wright, "Simulation of Neutron and Gamma Ray emission from fission," Lawrence Livermore National Laboratory, Livermore CA Tech. Rep. UCRL-AR-228518, 2007.
- [25] V. Weisskopf, "Statistics and Nuclear Reactions," *Phys. Rev.*, vol. 52, no. 4, pp. 295-303, 1937.
- [26] E. B. Watt, "Energy Spectrum of Neutrons from Thermal Fission of ^{235}U ," *Phys. Rev.*, vol. 87, no. 6, pp. 1037-1041, 1952.
- [27] O. Litaize and O. Serot, "Investigation of phenomenological models for the Monte Carlo simulation of the prompt fission neutron and γ emission," *Phys. Rev. C*, vol. 82, no. 5, 2011.
- [28] N. Kornilov, F.-J. Hamsch and V. A. S., "Neutron emission in fission," *Nucl. Phys. A*, vol. 789, no. 1-4, pp. 55-72, 2007.
- [29] T. Ethvignot, M. Devlin, R. Drosch, T. Granier, R. C. Haight, B. Morillon, R. O. Nelson, J. M. O'Donnell and D. Rochman, "Prompt-fission-neutron average energy for $^{238}\text{U}(n,f)$ from threshold to 200 MeV," *Phys. Lett. B*, vol. 575, no. 3-4, pp. 221-228, 2003.
- [30] D. Madland and A.C. Kahler, "Refinements in the Los Alamos model of the prompt fission neutron spectrum," *Nucl. Phys. A*, vol. 957, pp. 289-311, 2017.
- [31] G. Choppin, O. L. J and J. Rydberg, "Radiochemistry and Nuclear Chemistry: 4th Edition," in *Radiation Effects on Matter*, Amsterdam, Elsevier Inc., 2002, p. 166.
- [32] G. F. Knoll, "Interaction of Neutrons," in *Radiation Detection and Measurement, 3rd Edition*, Wiley, 2000, pp. 55-57.
- [33] D. Hei, H. Zhuang, W. Jia, C. Cheng, Z. Jiang, H. Wang and D. Chen, "Design of a setup for ^{252}Cf neutron source for storage and analysis purpose," *Nucl. Instrum. Methods Phys. Res. B*, vol. 386, pp. 1-3, 2016.

- [34] B. J. Marion and C. F. Young, *Nuclear Reaction Analysis: Graphs and Tables*, Amsterdam, 1968.
- [35] A. Enqvist and I. Pazsit, "Calculation of the light pulse distributions induced by fast neutrons in organic scintillation detectors," *Nucl. Instrum. Methods Phys. Res. A*, vol. 618, no. 1-3, pp. 266-274, 2010.
- [36] G. F. Knoll, "Fast Neutron Detectors," in *Radiation Detection and Measurement, 3rd Edition*, Hoboken, NJ, USA, Wiley, 2000, pp. 553-558.
- [37] E. Rutherford, "The scattering of alpha and beta particles by matter and the structure of the atom," *Philos. Mag*, vol. 21, no. 6, 1911.
- [38] B. J. Birks, *The Theory and Practice of Scintillation Counting*, New York, NY, USA: Pergamon, 1964.
- [39] R.-Y. Zhu, "Radiation Damage Effects," in *Handbook of Particle Detection and Imaging*, Heidelberg, Springer-Verlag, 2012, pp. 537-559.
- [40] S. Golovkin, A. Konstantinchenko, V. Kozlov, A. Kushnirenko, A. Pyshechev, V. Shershukov, V. Vasil'chenko and K. Zimyn, "Radiation damage studies on new liquid scintillators and liquid-core scintillating fibers,," *Nucl. Instrum. Methods Phys. Res. A*, vol. 362, no. 2-3, pp. 283-291, 1995.
- [41] M. Ceconello, "Liquid Scintillators Neutron Response Function: A Tutorial," *J Fusion Energy*, vol. 38, no. 3-4, pp. 356-375, 2019.
- [42] N. Kornilov, I. Fabry, S. Oberstedt and F. Hamsch, "Total characterization of neutron detectors with a ^{252}Cf source and a new light output determination," *Nucl. Instrum. Methods Phys. Res. A*, vol. 599, no. 2-3, pp. 226-233, 2009.
- [43] A. Enqvist, C. C. Lawrence, B. M. Wieger, S. A. Pozzi and T. N. Massey, "Neutron light output response and resolution functions in EJ-

- 309 liquid scintillation detectors,” *Nucl. Instrum. Methods Phys. Res. A*, vol. 715, pp. 79-86, 2013.
- [44] N. Zaitseva, A. Glenn, L. Carman, R. Hatarik, S. Hamel, M. Faust, B. Schabes, N. Cherepy and S. Payne, “Pulse Shape Discrimination in Impure and Mixed Single-Crystal Organic Scintillators,” *IEEE Trans. Nucl. Sci.*, vol. 58, no. 6, pp. 3411 - 3420, 2011.
- [45] I. Pawełczak, S. Ouedraogo, A. Glenn, R. Wurtz and L. Nakae, “Studies of neutron- γ pulse shape discrimination in EJ-309 liquid scintillator using charge integration method,” *Nucl. Instrum. Methods Phys. Res. A*, vol. 711, pp. 21-26, 2013.
- [46] M. Matzke, “Unfolding Procedures,” *Rad. Proct. Dosim.*, vol. 107, no. 1-3, pp. 155-174, 2003.
- [47] A. Tomanin, J. Paepen, P. Schillebeeckx, R. Wynants, R. Nolte and A. Lavietes, “Characterization of a cubic EJ-309 liquid scintillator detector,” *Nucl. Instrum. Methods Phys. Res. A*, vol. 756, pp. 45-54, 2014.
- [48] M. Gohil, K. Banerjee, S. Bhattacharya, K. K. T, G. Rana, K. M. J, R. Meena, H. Pandey, K. P. T, A. Ghosh, S. Dey, D. Mukhopadhyay, S. Pandit, R. P. S, T. Banerjee and Bandhopadhyay, “Measurement and simulation of neutron response function of organic liquid scintillator detector,” *Nucl. Instrum. Meth. Phys. Res. A*, vol. 664, no. 1, pp. 304-309, 2012.
- [49] A. Enqvist, C. C. Lawrence, B. M. Wieger, S. A. Pozzi and T. N. Massey, “Neutron light output response and resolution functions in EJ309 liquid scintillation detectors,” *Nucl. Instrum. Methods Phys. Res. A*, vol. 715, pp. 79 - 86, 2013.
- [50] G. Dietze and H. Klein, “NRESP4 and NEFF4 - Monte Carlo codes for the calculation of neutron response functions and detection efficiencies for NE 213 scintillation detectors,” *Physikalisch-Technische*

Bundesanstalt, Braunschweig (Germany, F.R.) Tech. Rep.
RN:14769159, 1982.

- [51] M. Frégeau, M. Delarue, A.-M. Frelin-Labalme, B. Laurent, X. Ledoux and C. Varignon, "Light response and efficiency calibration of EJ309 liquid scintillator between 3 and 45 MeV," *Nucl. Instrum. Methods Phys. Res. A*, vol. 941, 2019.
- [52] N. Kornilov, I. Fabry, S. Oberstedt and F.-J. Hamsch, "Total characterization of neutron detectors with a ^{252}Cf source and a new light output determination," *Nucl. Instrum. Methods Phys. Res. A*, vol. 599, no. 2-3, pp. 226-233, 2009.
- [53] H. Bai, Z. Wang, L. Zhang, Y. Lu, H. Jiang, J. Chen and G. Zhang, "Calibration of an EJ309 liquid scintillator using an AmBe neutron source," *Nucl. Instrum. Methods Phys. Res. A*, vol. 863, pp. 47-54, 2017.
- [54] F. Pino, L. Stevanato, D. Cester, G. Nebbia, L. Sajo-Bohus and G. Viesti, "The light output and the detection efficiency of the liquid scintillator EJ-309," *Appl. Radiat. Isot.*, vol. 89, pp. 79 - 84, 2014.
- [55] S. Meada, H. Tomita, J. Kawarabayashi and T. Iguchi, "Fundamental Study on Neutron Spectrum Unfolding using Maximum Entropy and Maximum Likelihood Method," *Prog. Nucl. Sci. Tech*, vol. 1, pp. 233-236, 2011.
- [56] L. Lebreton, A. Zimbal and D. Thomas, "Experimental Comparison of ^{241}Am -Be Neutron Fluence Energy Distributions," *Radiat. Prot. Dosimetry*, vol. 126, no. 1-4, pp. 3-7, 2007.
- [57] G. M. Ishak-Boushaki and M. Allab, "Comparison between standard unfolding and Bayesian methods in Bonner spheres neutron spectrometry," *Nucl. Instrum. Methods Phys. Res. A*, vol. 689, pp. 35-39, 2012.

- [58] M. Regginato and A. Zimbal, "Bayesian and maximum entropy methods for fusion diagnostic measurements with compact neutron spectrometers," *Rev. Sci. Instrum.*, vol. 79, no. 2, p. 023505, 2008.
- [59] M. Reginatto, P. Goldhagen and S. Neumann, "Spectrum unfolding, sensitivity analysis and propagation of uncertainties with the maximum entropy deconvolution code MAXED," *Nucl. Instrum. Methods Phys. Res. A*, vol. 476, no. 1-2, pp. 242-246, 2002.
- [60] G. F. Perey, "Spectrum Unfolding by the least squares method," Oak Ridge National Laboratory, Oak Ridge, Tennessee, 1977.
- [61] M. Reginatto, "Overview of spectral unfolding techniques and uncertainty estimation," *Radiat. Meas.*, vol. 45, no. 10, pp. 1323-1329, 2010.
- [62] N. J. Roberts, "Investigation of combined unfolding of neutron spectra using the UMG unfolding codes," *Radiat. Proct. Dosim.*, vol. 126, no. 1-4, pp. 398-403, 2007.
- [63] C. C. Lawrence, A. Enqvist, M. Flaska, S. A. Pozzi and F. Becchetti, "Comparison of spectrum-unfolding performance of (EJ315) and (EJ309) liquid scintillators on measured ^{252}Cf pulse-height spectra," *Nucl. Instrum. Methods Phys. Res. A*, vol. 729, pp. 924-929, 2013.
- [64] S. Avdic, S. A. Pozzi and V. Protopopescu, "Detector response unfolding using artificial neural networks," *Nucl. Instrum. Methods Phys. Res. A*, vol. 565, pp. 924-929, 2006.
- [65] S. A. Hossein, "Neutron spectrum unfolding using artificial neural network and modified least square method," *Radiat. Phys. Chem.*, vol. 126, pp. 75-84, 2016.
- [66] S. Vitisha and K. P. Sarkar, "Neutron spectrum unfolding using genetic algorithm in a Monte Carlo simulation," *Nucl. Instrum. Methods Phys. Res. A*, vol. 737, pp. 76-86, 2014.

- [67] M. Matzke, "Propagation of uncertainties in unfolding procedures," *Nucl. Instrum. Methods Phys. Res. A*, vol. 476, no. 1-2, pp. 230-241, 2002.
- [68] G. F. Knoll, "Chapter 14, Slow Neutron Detection Methods," in *Radiation Detection and Measurement, 3rd Edition*, Hoboken, NJ, USA, Wiley, 2000, pp. 505-513.
- [69] D. J. Thomas, "Neutron Spectrometry for radiation protection," *Radiat. Prot. Dosimetry*, vol. 110, no. 1-4, pp. 141-149, 2004.
- [70] H. Tatsuta, K. Katoh and Y. Yoshida, "Energy Response of BF₃ Counter Using Paraffin Moderators," *Jap. J. Appl. Phys.*, vol. 4, no. 5, pp. 321-325, 1965.
- [71] T. Nishitani and J. D. Strachan, "Neutron Spectroscopy with a ³He Ionization Chamber on TFTR," *Jpn. J Appl. Phys.*, vol. 29, no. 3, pp. 591-596, 1990.
- [72] D. Chichester, J. Johnson and E.H. Seabury, "Fast-neutron spectrometry using a ³He ionization chamber and digital pulse shape analysis,," *Appl. Radiat. Isot.*, vol. 70, no. 8, pp. 1457-1463, 2012.
- [73] A. Gook, F. J. Hambsch and M. Vidali, "Prompt neutron multiplicity in correlation with fragments from spontaneous fission of ²⁵²Cf," *Phys. Rev. C*, vol. 90, no. 6, p. 064611, 2014.
- [74] S. Zeynalov, O. Zeynalova, F.-J. Hambsch, P. Sedyshev and V. Shvetsov, "Ionization chamber for prompt fission neutron investigation," *Phys. Proc.*, vol. 59, pp. 160-166, 2014.
- [75] D. Mazed, S. Mameri and R. Ciolini, "Design parameters and technology optimization of ³He-filled proportionalcounters for thermal neutron detection and spectrometry applications," *Rad. Meas.*, vol. 47, no. 8, pp. 577-587, 2012.
- [76] M. Manolopoulou, M. Fragopoulou, S. Stoulos, C. Koukorava, A. Spyrou, G. Perdikakis, S. Hashemi-Nezhad and M. Zamani, "Studies on

the response of ^3He and ^4He proportional counters to monoenergetic fast neutrons,," *Nucl. Instrum. Methods Phys. Res. A*, vol. 562, no. 1, pp. 371-379, 2006.

- [77] M. Weyrauch, A. Casnati, P. Schillebeeckx and M. Clapham, "Use of ^4He -filled proportional counters as neutron spectrometers," *Nucl. Instrum. Methods Phys. Res. A*, vol. 403, no. 2-3, pp. 442-454, 1998.
- [78] T. R. Kouzes, H. J. Ely, T. A. Lintereur, R. E. Siciliano and L. M. Woodring, "BF₃ Neutron Detector tests," Pacific Northwest National Laboratory, Washington Tech. Rep. PNNL-19050, 2009.
- [79] T. Langford, C. Bass, E. Beise, H. Breuer, D. Erwin, C. Heimbach and J. Nico, "Event identification in ^3He proportional counters using risetime discrimination," *Nucl. Instrum. Methods Phys. Res. A*, vol. 717, pp. 51-57, 2013.
- [80] G. W. R. Endres, J. M. Aldrich, L. W. Brackenbush, L. G. Faust, R. V. Griffith and D. E. Hankins, "Neutron Dosimetry at Commercial Nuclear plants," Pacific Northwest National Laboratory, WA Tech. Rep. PNL-3585, 1981.
- [81] E. Bougamont, A. Dastgheibi, J. Derre, J. Galan, G. Gerbier, I. Giomataris, M. Gros, I. Katsioulas, D. Jourde, P. Magnier, X. Navick, T. Papaevangelou, I. Savvidis and G. Tsiledakis, "Neutron spectroscopy with the Spherical Proportional Counter based on nitrogen gas," *Nucl. Instrum. Methods Phys. Res. A*, vol. 847, pp. 10-14, 2017.
- [82] F. D. Brooks and H. Klein, "Neutron Spectroscopy- historical review and present status," *Nucl. Instrum. Methods Phys. Res. A*, vol. 476, no. 1-2, pp. 1-11, 2002.
- [83] D. J. Thomas and A. V. Alevra, "Bonner sphere spectrometers—a critical review," *Nucl. Instrum. Methods Phys. Res. A*, vol. 476, no. 1-2, pp. 12-20, 2002.

- [84] R. Bedogni, A. Esposito and M. Chiti, "Determination of workplace neutron spectra at a high energy hadron accelerator using active and passive Bonner sphere spectrometers," *Radiat. Meas.*, vol. 43, no. 2-6, pp. 1113-1117, 2008.
- [85] G. M. Ishak-Boushaki and M. Allab, "Comparison between standard unfolding and Bayesian methods in Bonner spheres neutron spectrometry," *Nucl. Instrum. Methods Phys. Res. A*, vol. 689, pp. 35-39, 2012.
- [86] R. L. Bramblett, R. I. Ewing and T. W. Bonner, "A new type of neutron spectrometer," *Nucl. Inst. Meth.*, vol. 9, no. 1, pp. 1-12, 1960.
- [87] R. Bedogni, J. M. Gomez-Ros, M. Costa, V. Monti, E. Durisi, O. S. Planell, L. Menzio, D. Flammini, F. Moro, M. Pillon and A. Pietropaolo, "An active Bonner sphere spectrometer for intense neutron fields," *Nucl. Instrum. Methods Phys. Res. A*, vol. 940, pp. 302-306, 2019.
- [88] D. J. Thomas, A. G. Bardell and E. M. Macaulay, "Characterisation of a gold foil-based Bonner sphere set and measurements of neutron spectra at a medical accelerator," *Nucl. Instrum. Methods Phys. Res. A*, vol. 476, no. 1-2, pp. 31-35, 2002.
- [89] R. Bedogni, P. Ferrari, G. Gualdrini and A. Esposito, "Design and experimental validation of a Bonner Sphere Spectrometer based on Dysprosium activation foils," *Radiat. Meas.*, vol. 45, no. 10, pp. 1201-1204, 2010.
- [90] R. Bedogni, R. Bedogni, J. M. Gómez-Ros, D. Bortot, A. Pola, M. V. Introini, A. Esposito, A. Gentile, G. Mazzitelli and B. Buonomo, "Development of single-exposure, multidetector neutron spectrometers: The NESCOFI@BTF project," *Radiat. Prot Dosimetry*, vol. 161, no. 1-4, pp. 37-40, 2014.
- [91] R. Bedogni, J. M. Gómez-Ros, A. Pola, M. V. Introini, D. Bortot, A. Gentile, A. Esposito, G. Mazzitelli, B. Buonomo, L. Quintieri and L.

- Foggetta, "Testing a newly developed single-sphere neutron spectrometer in reference monochromatic fields from 147keV to 14.8MeV,," *Nucl. Instrum. Methods Phys. Res. A*, vol. 714, pp. 110-114, 2013.
- [92] M. A. Wonders, D. L. Chichester and M. Flaska, "Characterization of New-Generation Silicon Photomultipliers for Nuclear Security Applications," *EPJ Web of Conferences*, vol. 170, p. 07015, 2018.
- [93] R. A. Akbarov, G. S. Ahmadov, F. I. Ahmadov, D. Berikov, M. Holik, R. Mammadov, S. M. Nuruyev, A. Z. Sadigov, Z. Y. Sadygov and S. I. Tyutyunnikov, "Fast neutron detectors with silicon photomultiplier readouts," *Nucl. Instrum. Methods Phys. Res. A*, vol. 936, pp. 549-551, 2019.
- [94] Y. Liang, T. Zhu, C. E. Parker, A. L. Richard, T. N. Massey, R. Chandra, H. Ray, K. A. Jordan, J. Baciak and A. Enqvist, "Neutron spectroscopy and spectral unfolding with ^4He fast neutron scintillators,," *Nucl. Instrum. Methods Phys. Res. A*, vol. 922, pp. 1-7, 2019.
- [95] R. P. Kelley, L. M. Rolison, J. M. Lewis, D. Murer, T. N. Massey, A. Enqvist and K. A. Jordan, "Neutron response function characterization of ^4He scintillation detectors," *Nucl. Instrum. Methods Phys. Res. A*, vol. 793, pp. 101-107, 2015.
- [96] G. F. Knoll, T. M. Henderson and W. J. Felmler, "A Novel ^3He Scintillation Detector," *IEEE Trans. Nucl. Sci.*, vol. 34, no. 1, pp. 470-474, 1987.
- [97] L. A. Boatner, E. P. Comer, G. W. Wright, J. O. Ramey, R. A. Riedel, G. E. Jellison and J. A. Kolopus, "Improved lithium iodide neutron scintillator with Eu^{2+} activation: The elimination of Suzuki-Phase precipitates," *Nucl. Instrum. Methods Phys. Res. A*, vol. 854, pp. 82-88, 2017.

- [98] X. Wen, T. Harvey, R. Weinmann-Smith, J. Walker, Y. Noh, R. Farley and A. Enqvist, "Characterization of a tin-loaded liquid scintillator for gamma spectroscopy and neutron detection," *Nucl. Instrum. Methods Phys. Res. A*, vol. 897, pp. 47-53, 2018.
- [99] C. Frangville, A. Grabowski, J. Dumazert, E. Montbarbon, C. Lynde, R. Coulon, A. Venerosy, G. H. V. Bertrand and M. Hamel, "⁶Li₂10B₄O₇ NPs-loaded plastic scintillators for fast/thermal neutron and gamma ray detection," *Mat. Chem. Frontiers*, vol. 3, no. 8, pp. 1574-1579, 2019.
- [100] T. Brown, P. Chowdhury, E. Doucet, E. Jackson, C. Lister, A. Mitchell, C. Morse, A. Rogers, G. Wilson, N. D'Olympia, M. Devlin, N. Fotiades, J. Gomez, S. Mosby and R. Nelson, "Applications of C7LYC scintillators in fast neutron spectroscopy," *Nucl. Instrum. Methods Phys. Res. A*, vol. 954, p. 161123, 2020.
- [101] C. Cowles, S. Behling, P. Baldez, M. Folsom, R. Kouzes, V. Kukharev, A. Lintereur, S. Robinson, E. Siciliano, S. Stave and P. Valdez, "Development of a lithium fluoride zinc sulfide based neutron multiplicity counter," *Nucl. Instrum. Methods Phys. Res. A*, vol. 887, pp. 59-63, 2018.
- [102] M. Osipenko, V. Ceriale, G. Gariano, M. Girolami, S. Cerchi, R. Nolte, E. Pirovano, M. Ripani and D. Trucchi, "Calibration of a ⁶Li diamond-sandwich spectrometer with quasi-monoenergetic neutrons," *Nucl. Instrum. Methods Phys. Res. A*, vol. 931, pp. 135-141, 2019.
- [103] M. Osipenko, M. Ripani, G. Ricco, B. Caiffi, F. Pompili, M. Pillon, M. Angelone, G. Verona-Rinati, R. Cardarelli, G. Mila and S. Argiro, "Neutron spectrometer for fast nuclear reactors," *Nucl. Instrum. Methods Phys. Res. A*, vol. 799, pp. 207-213, 2015.
- [104] H. Kluge and K. Weise, "The Neutron Energy Spectrum of a ²⁴¹Am-Be(Alpha,n) Source and Resulting Mean Fluence to Dose Equivalent Conversion Factors," *Radiat. Prot. Dosim.*, vol. 2, pp. 85-93, 1982.

- [105] J. W. Marsh, D. J. Thomas and M. Burke, "High resolution measurements of neutron energy spectra from Am-Be and Am-B neutron sources," *Nucl. Instrum. Methods Phys. Res. A*, vol. 366, no. 2-3, pp. 340-348, 1995.
- [106] A. Seghour and F. Seghour, "Unfolding neutron energy spectra from foil activation detector measurements with the Gold algorithm," *Nucl. Instrum. Methods Phys. Res. A*, vol. 457, no. 3, pp. 617-626, 2001.
- [107] E. Vagena, K. Theodorou and S. Stoulos, "Thick-foils activation technique for neutron spectrum unfolding with the MINUIT routine— Comparison with GEANT4 simulations,," *Nucl. Instrum. Methods Phys. Res. A*, vol. 887, pp. 64-69, 2018.
- [108] F. Molina, P. Aguilera, J. Romero-Barrientos, H. Arellano, J. Agramunt, J. Mede, J. M. and M. Zambra, "Energy distribution of the neutron flux measurements at the Chilean Reactor RECH-1 using multi-foil neutron activation and the Expectation Maximization unfolding algorithm,," *Appl. Radiat. Isot.*, vol. 129, pp. 28-34, 2017.
- [109] U. d. Bitelli, F. P. G. Martins and R. Jerez, "Measurements of the neutron spectrum energy in the IPEN/MB-01 reactor core," *Braz. J Phys.*, vol. 39, no. 1, pp. 39-43, 2009.
- [110] D. Thomas, A. Bardell and E. Macaulay, "Characterisation of a gold foil-based Bonner sphere set and measurements of neutron spectra at a medical accelerator,," *Nucl. Instrum. Methods Phys. Res. A*, vol. 476, no. 1-2, pp. 31-35, 2002.
- [111] D. Bleuel, M. McMahan, L. Ahle, B. Barquest, J. Cerny, L. Heilbronn and C.C. Jewett, "Characterization of a tunable quasi-monoenergetic neutron beam from deuteron breakup," *Nucl. Instrum. Methods Phys. Res. B*, vol. 261, no. 1-2, pp. 974-979, 2007.

- [112] J. I. W. Watterson, "Review of Accelerator based neutron sources and their applications," Schonland research Centre, Wits, South Africa Tech. Rep. XA0054945, 2000.
- [113] M. Devlin, J. Gomez, K. Kelly, R. Haight, J. O'Donnell, T. Taddeucci, H. Lee, S. Mosby, B. Perdue, N. Fotiades, J. Ullmann, C. Wu, B. Bucher, M. Buckner, R. Henderson, D. Neudecker, M. White, P. Talou, M. Rising and C. Solomon, "The Prompt Fission Neutron Spectrum of $^{235}\text{U}(n,f)$ below 2.5 MeV for Incident Neutrons from 0.7 to 20 MeV,," *Nucl. Data Sheets*, vol. 148, pp. 322-337, 2018.
- [114] N. Kornilov, A. Kagalenko, V. Baryba, V. Demenkov, S. Pupko and P. Androsenko, "Inelastic neutron scattering and prompt fission neutron spectra for ^{237}Np ," *Anns Nucl. Energy*, vol. 27, pp. 1643-1667, 2000.
- [115] J. Pal, S. Saha, C. C. Dey, B. K. Sinha and M. B. Chatterjee, "Neutron energy spectrum of an Am-Be source by gamma gated NTOF technique," *Radiat. Phys. and Chem.*, vol. 51, no. 4-6, pp. 475-477, 1998.
- [116] J. Scherzinger, R. A. Jebali, J. Annand, K. Fissum, R. Hall-Wilton, S. Koufigar, N. Mauritzson, F. Messi, H. Perrey and E. Rofors, "A comparison of untagged gamma-ray and tagged-neutron yields from $^{241}\text{AmBe}$ and $^{238}\text{PuBe}$ sources,," *Appl. Radiat. Isot.*, vol. 127, pp. 98-102, 2017.
- [117] M. Skiba, G. Ericsson, A. Hjalmarsson, C. Hellesen, S. Conroy, E. Andersson-Sundén, J. Eriksson and J. Contributors, "Kinematic background discrimination methods using a fully digital data acquisition system for TOFOR," *Nucl. Instrum. Methods Phys. Res. A*, vol. 838, pp. 82-88, 2016.
- [118] F. D. Becchetti, M. Febbraro, R. Torres-Isea, M. Ojaruega and L. Baum, " ^{252}Cf fission-neutron spectrum using a simplified time-of-flight setup: An advanced teaching laboratory experiment," *Am. J. Phys.*, vol. 81, no. 2, pp. 112-119, 2013.

- [119] E. Blain, A. Daskalakis, R. C. Block and Y. Danon, "Measurement of prompt fission neutron spectrum for spontaneous fission of ^{252}Cf using γ multiplicity tagging," *Phys. Rev. C*, vol. 95, p. 064615, 2017.
- [120] Hamamatsu, "Basic Principles of Photomultiplier Tubes," in *Photomultiplier tubes, Third edition*, Hamamatsu Photonics K K, 2007, pp. 13-19.
- [121] Burle Industries Ltd, "Photomultiplier Applications," in *Photomultiplier Handbook*, Burle Industries Ltd, 1980, pp. 80-119.
- [122] M. Bruggeman, P. Baeten, W. De Boeck and R. Carchon, "Neutron Coincidence Counting based on Time Interval Analysis with Dead Time Corrected One and Two Dimensional Rossi-alpha Distributions. An application for Passive Neutron Waste Assay," *Nucl. Instrum. Methods Phys. Res. A*, vol. 382, pp. 511-518, 1996.
- [123] G. R. Chopin, J. Liljenzin and J. Rydberg, "Chapter 13, Particle Accelerators," in *Radio Chemistry and Nuclear Chemistry*, Elsevier, 2002, pp. 352-354.
- [124] N. J. Roberts, H. Tagziria and D. J. Thomas, "Determination of the effective centres of the NPL long counters," NPL, London Tech. Rep. NPL REPORT DQL RN004, 2004.
- [125] G. C. Taylor and D. J. Thomas, "Neutron scatter characteristics of the low scatter facility of the Chadwick building," National Physical Laboratory, London Tech. Rep. CIRM 17, 1998.
- [126] J. Scherzinger, J. R. M. Annand, G. Davatz, K. G. Fissum, U. Gendotti, R. R. Hall-Wilton, A. Rosborg, E. Hakansson, R. Jebali, K. Kanaki, M. Lundin, B. Nilsson and H. Svensson, "Tagging fast neutrons from an AmBe source," *Appl. Radiat. Isot.*, vol. 98, pp. 74-79, 2015.
- [127] Z. A. Aleksandrova, V. I. Bolshov, V. F. Kuznetsov, G. N. Smirenkin and M. N. Tarasko, "Spectra of the prompt neutrons arising from the

spontaneous fission of ^{252}Cf , ^{244}Cm and ^{240}Pu ,” *Sov. Atom. Ener.*, vol. 36, pp. 355-358, 1974.

- [128] D. L and S. B, “Status of measurements of fission neutron spectra of minor actinides,” in *Selected Papers of ISTC Workshop on Nuclear Data of Minor Actinides*, Tokai, 1997.
- [129] O. I. Batenkov, G. S. Boykov, L. V. Drapchinski, M. Marajov and V. A. Trenkin, “The measurement of prompt neutron spectrum in spontaneous fission of ^{244}Cm ,” in *Selected Papers of ISTC Workshop on Nuclear Data of Minor Actinides*, Tokai, Japan, 1997.
- [130] X-5 Monte Carlo Team, “MCNP - A general monte carlo N-Particle transport code, Version 5,” Los Alamos National Laboratory, Los Alamos, NM Tech. Rep. LA-13709-M, 2003.
- [131] Y. Zamyatiny, N. Kroshkin, A. Mel'nikov and V. Nefedov, “Measurement of the energy spectra and the average number of prompt neutrons produced in the fission of actinide elements,” in *Nuclear data for Reactors (Proc. of the 2nd Int. Conf. on Nucl. Data for Reactors)*, Helsinki, 1970.
- [132] H. Maier-Leibnitz, P. Armbruster and H. J. Specht, “Prompt and Delayed Gamma rays from fission,” IAEA, Vienna Tech. Rep. Jul-405-NP, 1965.
- [133] A. Chyzh, C. Y. Wu, E. Kwan, R. A. Henderson, J. M. Gostic, T. A. Bredeweg, R. C. Haight and A. C. Hayes-Sterbenz, “Evidence for the stochastic aspect of prompt γ emission in spontaneous fission,” *Phys. Rev. C*, vol. 85, no. 2, 2012.
- [134] D. Neudecker, T. Taddeucci, R. Haight, H. Lee, M. White and M. Rising, “The Need for Precise and Well-documented Experimental Data on Prompt Fission Neutron Spectra from Neutron-induced Fission of ^{239}Pu ,” *Nucl. Data Sheets*, vol. 131, pp. 289-318, 2016.

[135] Eljen Technology, "NEUTRON/GAMMA PSD LIQUID SCINTILLATOR EJ301, EJ309 DATASHEET," 2018. [Online]. Available: https://eljentechnology.com/images/products/data_sheets/EJ-301_EJ-309.pdf. [Accessed 15 01 2020].

APPENDIX A: GAMMA INTERACTIONS IN THE DETECTOR

A gamma photon incident with the detector volume also have the ability to interact with the scintillant and produce a signal. Upon interaction a pulse of optical photons is produced that is very similar to those produced by neutrons, but the mechanism whereby they are formed is different. Similarly, to neutrons, gamma rays are uncharged and therefore do not directly form ionisation tracks in the scintillant. However, gamma rays are an electromagnetic phenomenon, and therefore in contrast with neutrons, will interact with atomic electrons, allowing a number of different excitement mechanisms. The nature of the interaction between gamma photons and atomic electrons means that gamma interactions happen in discrete events, and therefore behave more like a neutron recoiling off nuclei than an alpha particle slowing as it travels through matter.

At the energy range studied in this work (0.5-20MeV) Compton scattering is the predominant mechanism by which gamma photons deposit their energy into the scintillant [19]. In this process an incident gamma photon interacts with an electron in the orbital shell of an atom in the scintillator, imparts some of its energy to the electron and is then scattered by an angle θ . The energy gained by the electron is enough to liberate it from the atom of origin producing a free electron. This free electron now travels through the scintillant as an energetic charged particle, exciting atomic electrons into higher atomic singlet and triplet quantum states, producing de-excitation photons in the same manner as neutrons. The proportion of the gamma ray's energy gained by the electron depends on the scatter angle of the initial gamma photon.

The electron recoil energy is given by:

$$E_e = E_\gamma - E_{\gamma 1}$$

Where E_γ is the gamma energy, and $E_{\gamma 1}$ is the gamma energy after the recoil, given by:

$$E_{\gamma 1} = \frac{E_\gamma}{1 + \frac{E_\gamma}{m_0 c^2} (1 - \cos\theta)}$$

This gives a theoretical maximum amount of energy that can be transferred to the electron, in the case where $\theta=180^\circ$.

As the electron can scatter at any angle between 0 and 180° a mono-energetic source of gamma photons will produce a continuum of electron energies, with a high energy cut-off at the theoretical maximum. As the photon will never transfer the entirety of its energy to the recoil photon, the Compton edge is lower in energy than the full energy of a monoenergetic gamma source.

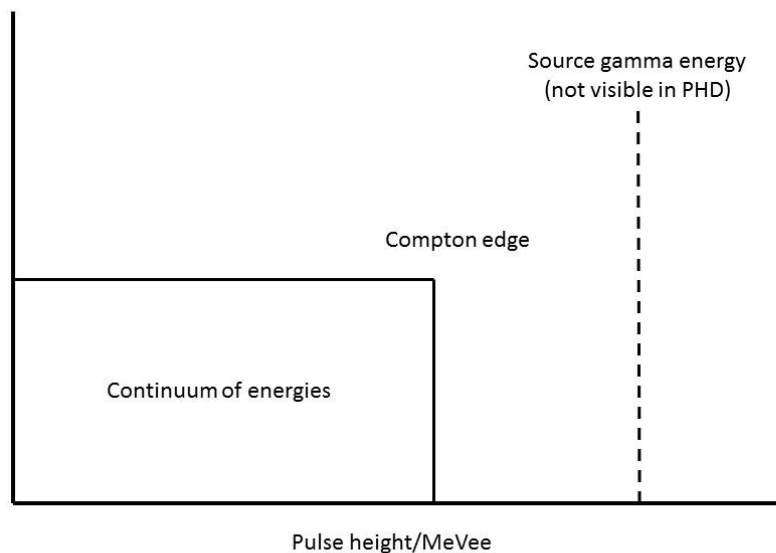


Figure 92: Compton edge and spectrum continuum produced by a mono-energetic gamma source. (Resolution effects not included)

Some commonly used gamma sensitive detectors, for example sodium iodide detectors, exhibit a full energy peak in their responses. This is produced by pair production effects and does not feature in the organic scintillator pulse height spectrum. Therefore, any energy scale axis calibrations using gamma sources rely on finding the Compton edge and correctly associating it with a known peak in the gamma spectrum.

APPENDIX B: PROPERTIES OF EJ301 AND EJ309

Data provided by the manufacturer Eljen [135].

Properties	EJ301	EJ309
Light output (% Anthracene)	78	80
Scintillation efficiency (photons/MeV e ⁻)	12000	12300
Wavelength of maximum emission	425	424
Decay time, short Component (ns)	3.2	3.5
Mean decay times of first 3 components (ns)	3.16 32.3 270	N/A
Bulk light Attenuation length (m)	2.5-3	>1
Specific Gravity	0.874	0.959
Refractive index	1.505	1.57
Flash point (°C)	26	144
Boiling point (°C at 1atm)	141	290-300
Vapour pressure (mm Hg at 20°C)	6	0.002
No of H Atoms per cm ³ (x10 ²²)	4.82	5.43
No of C Atoms per cm ³ (x10 ²²)	3.98	4.35
No of electrons per cm ³ (x10 ²²)	2.27	3.16
